

Electronic Thesis and Dissertation Repository

---

12-2-2014 12:00 AM

## Numerical Modeling of Deformation, Oscillation, Spreading and Collision Characteristics of Droplets in an Electric Field

Osameh Ghazian, *The University of Western Ontario*

Supervisor: Dr. Kazimierz Adamiak, *The University of Western Ontario*

A thesis submitted in partial fulfillment of the requirements for the Doctor of Philosophy degree in Electrical and Computer Engineering

© Osameh Ghazian 2014

Follow this and additional works at: <https://ir.lib.uwo.ca/etd>



Part of the [Biomedical Commons](#), [Mechanical Engineering Commons](#), and the [Other Electrical and Computer Engineering Commons](#)

---

### Recommended Citation

Ghazian, Osameh, "Numerical Modeling of Deformation, Oscillation, Spreading and Collision Characteristics of Droplets in an Electric Field" (2014). *Electronic Thesis and Dissertation Repository*. 2538.

<https://ir.lib.uwo.ca/etd/2538>

This Dissertation/Thesis is brought to you for free and open access by Scholarship@Western. It has been accepted for inclusion in Electronic Thesis and Dissertation Repository by an authorized administrator of Scholarship@Western. For more information, please contact [wlsadmin@uwo.ca](mailto:wlsadmin@uwo.ca).

«NUMERICAL MODELING OF DEFORMATION, OSCILLATION, SPREADING  
AND COLLISION CHARACTERISTICS OF DROPLETS IN AN ELECTRIC  
FIELD»

(Thesis format: Integrated-Article)

by

«Osameh Ghazian»

Graduate Program in «Electrical & Computer Engineering»

A thesis submitted in partial fulfillment  
of the requirements for the degree of  
« Doctor of Philosophy »

The School of Graduate and Postdoctoral Studies  
The University of Western Ontario  
London, Ontario, Canada

© « Osameh Ghazian » « 2014 »

## Abstract

Electric field induced flows, or electrohydrodynamics (EHD), have been promising in many fast-growing technologies, where droplet movement and deformation can be controlled to enhance heat transfer and mass transport. Several complex EHD problems existing in many applications were investigated in this thesis.

Firstly, this thesis presents the results of numerical simulations of the deformation, oscillation and breakup of a weakly conducting droplet suspended in an ambient medium with higher conductivity. It is the first time that the deformation of such a droplet was investigated numerically in a 3D configuration. We have determined three types of behavior for the droplets, which are less conducting than ambient fluid: 1) oblate deformation (which can be predicted from the small perturbation theory), 2) oscillatory oblate-prolate deformation and 3) breakup of the droplet.

Secondly, a numerical study of droplet oscillation placed on different hydrophobic surfaces under the effect of applied AC voltage including the effect of ambient gas was investigated. The presented algorithm could reproduce droplet oscillations on a surface considering different contact angles. It has been found that the resonance frequency of the water droplet depends on the surface property of the hydrophobic materials and the electrostatic force.

Thirdly, a new design of an electrowetting mixer using the rotating electric field was proposed which offers a new method to effectively mix two droplets over a different range of AC frequencies. Two regimes were observed for droplet coalescence: 1) coalescence due to the high droplet deformation, 2) coalescence due to the interaction of electrically induced dipoles.

Fourthly, the spreading and retraction control of millimetric water droplets impacting on dry surfaces have been investigated to examine the effect of the surface charge density and electric field intensity. The effect of the surface charge on the spreading of droplets placed gently on surfaces was investigated in the first part. It was found that the maximum spreading diameter increases with an increasing charge. In the second part, the

impact of a droplet on a ground electrode was considered. It was also found that in order to keep the maximum diameter after the impact, less charge is needed for surfaces with lower contact angle.

Finally, the interaction between two identical charged droplets was investigated numerically. The effects of the impact velocity, drop size ratio and electric charge on the behavior of the combined droplet were investigated. It was shown that two conducting droplets carrying charges of the same polarity under some conditions may be electrically attracted. The formation of charged daughter droplets has been investigated and it was found that the number of the satellite droplets after collision appears to increase with an increase in the droplet charge.

## Keywords

Electrohydrodynamics; Numerical Simulation; Electric Field; Droplet; Oscillation; Breakup; Leaky Dielectric Liquid; Contact Angle; Hydrophobic Surface; Rotating Electric Field; Resonance Frequency; Coalescence; Electrically Induced Dipoles; Droplet Impact; Spreading; Maximum Spreading ratio; Charge Density; Surface Wettability; Head-on Collision; Satellite Droplets

## Co-Authorship Statement

This thesis has been written by Osameh Ghazian under supervision of Dr. Kazimierz Adamiak and Dr. G.S. Peter Castle. Parts of the material presented in this thesis have been published in several peer-reviewed journals and refereed conference proceedings as listed below. The research in each publication has been conducted by the principal author and guided/supported by or in collaboration with the underlined authors, who are the research supervisors or members of the advisory committee.

Chapter 3 presented a numerical investigation of the 3-D deformation of an initially uncharged and spherical droplet suspended in another immiscible fluid under DC uniform electric field. Three regimes were observed for droplet deformation: 1) oblate deformation (which can be predicted from the small perturbation theory), 2) oscillatory oblate-prolate deformation and 3) breakup of the droplet. O. Ghazian was the principal author of this chapter. Some revisions and recommendations were made by the supervisors Dr. K. Adamiak and Dr. G. S. P. Castle. The material in Chapter 3 has been published in:

*O. Ghazian, K. Adamiak and G.S.P Castle, "Numerical simulation of electrically deformed droplets less conductive than ambient fluid", Colloids and Surfaces A: Physicochemical and Engineering Aspects, Volume 423, 20 April 2013, Pages 27–34.*

In Chapter 4 the 3-D oscillations of a water droplet under the effect of external fields, such as gravity and sinusoidal electric field, were investigated numerically. The time variation of the shape of a perfectly conducting droplet demonstrated that a water droplet vibrates strongly at certain frequencies. O. Ghazian was the principal author of this chapter. Some revisions and recommendations were made by the supervisors Dr. K. Adamiak and Dr. G. S. P. Castle. The material in Chapter 4 has been published in:

*O. Ghazian, K. Adamiak and G.S.P Castle, “Electric-field-induced oscillations of water droplets deposited on insulating surfaces”, Journal of Electrostatics, Volume 71, Issue 3, June 2013, Pages 489–495.*

In Chapter 5 the 3-D oscillations and coalescence of water droplets deposited on a dielectric substrate under the effect of a rotating electric field was investigated. This chapter also presented a new design of an electrowetting mixer using the rotating electric field and offered a new method to effectively mix two droplets over a different range of AC frequencies. O. Ghazian was the principal author of this chapter. Some revisions and recommendations were made by the supervisors Dr. K. Adamiak and Dr. G. S. P. Castle. The material in Chapter 5 has been published in:

*O. Ghazian, K. Adamiak and G.S.P Castle, “Oscillation, pseudo-rotation and coalescence of sessile droplets in a rotating electric field”, Colloids and Surfaces A: Physicochemical and Engineering Aspects, Volume 441, 20 January 2014, Pages 346–353.*

In Chapter 6 the dynamics of spreading and impact of a dielectric droplet onto a dry conductive substrate in the presence of an external vertical electric field was investigated numerically. In the first part, the spreading of a charged dielectric droplet placed on a ground electrode was simulated. In the second part, the suppression of the droplet receding phase, after it has been impacted onto a surface, was investigated using a vertical field parallel to the impact axis. O. Ghazian was the principal author of this chapter. Some revisions and recommendations were made by the supervisors Dr. K. Adamiak and Dr. G. S. P. Castle. The material in Chapter 6 has been published in:

*O. Ghazian, K. Adamiak and G.S.P Castle, “Spreading and retraction control of charged dielectric droplets”, Colloids and Surfaces A: Physicochemical and Engineering Aspects, Volume 448, 20 April 2014, Pages 23–33.*

In Chapter 7 interaction between two identical charged droplets is investigated numerically. In the first part, the mechanism of Coulomb attraction between two conducting droplets is investigated. The second part of the study concerns the collision dynamics of two identical charged droplets. O. Ghazian was the principal author of this chapter. Some revisions and recommendations were made by the supervisors Dr. K. Adamiak and Dr. G. S. P. Castle. The material in Chapter 7 has been published in:

*O. Ghazian, K. Adamiak and G.S.P Castle, Head-on collision of electrically charged droplets, Journal of Electrostatics, Volume 73, February 2015, Pages 89–96.*

## Acknowledgments

I am appreciably grateful to Prof. K. Adamiak and Prof. G. S. Peter Castle, my research advisor, for their endless support and academic guidance that helped me to achieve my research goals. I would also like to express my deepest appreciation to them for their instructive advices and also their support and encouragement during this research. I could not have made it through my studies without their encouragement and guidance and they will always be my advisors. Your advice on both research as well as on my career have been priceless.

A special thanks to my family. Words cannot express how grateful I am to my mother, father, my mother-in law, and father-in-law, for all of the sacrifices that you've made on my behalf. I am indebted to my parents who raised me with a love of science and supported me in all my pursuits.

I would like to gratefully and sincerely thank staff members at the electronic shop at Western University who supported me throughout the course of my research.

I would also like to thank my friends and colleagues in the Applied Electrostatics Research Centre (AERC) at UWO. The group has been a source of friendships as well as good advice and collaboration. Particularly, I would like to thank Mohammadreza Ghazanchaei, Peyman Dordizadeh, Husam Eldin Osman and Seyed-Reza Mahmoudi.

Finally, I would like to thank my loving, supportive, encouraging, and patient wife Hoda for bringing the meaning of happiness to my life and all the stolen moments from her during these years.



# Contents

Abstract.....	ii
Co-Authorship Statement.....	iv
Acknowledgments.....	vii
Chapter 1.....	1
1 « Introduction and objectives».....	1
1.1 Introduction.....	1
1.2 Thesis objectives.....	2
1.2.1 Droplet deformation under the effect of electric field.....	2
1.2.2 Electrowetting and oscillations of droplets on insulating surfaces.....	3
1.2.3 Droplets impacting on solid surfaces.....	4
1.2.4 Droplet collisions.....	5
1.3 Thesis outline.....	6
References.....	9
Chapter 2.....	15
2 «Numerical models in simulating electrohydrodynamics of droplets».....	15
2.1 Modeling methods for two-phase flow.....	16
2.1.1 Volume-of-Fluid (VOF) method.....	17
2.1.2 Level-Set method.....	18
2.1.3 Conservative Level-Set method.....	20
2.1.4 Modeling of the surface tension force.....	23
2.2 Electrostatic force calculation.....	24
2.2.1 Leaky dielectric model.....	26
2.2.2 Perfect dielectric model.....	27
2.3 Finite Element Method.....	28

References.....	33
Chapter 3.....	37
3 « Numerical simulation of electrically deformed droplets less conductive than the ambient fluid» .....	37
3.1 Introduction.....	37
3.2 Problem statement.....	40
3.3 Simulation validation .....	45
3.4 Results and discussion .....	47
3.4.1 Small deformation.....	48
3.4.2 Oscillatory oblate-prolate motion .....	49
3.4.3 Break up .....	51
3.4.4 Effect of viscosity and conductivity ratios on droplet breakup .....	53
3.5 Conclusions.....	56
References.....	57
Chapter 4.....	59
4 « Electric-field-induced oscillations of water droplets deposited on insulating surfaces».....	59
4.1 Introduction.....	59
4.2 Problem statement.....	61
4.3 Results and discussion .....	66
4.4 Conclusions.....	73
References.....	74
Chapter 5.....	78
5 « Oscillation, pseudo-rotation and coalescence of sessile droplets in a rotating electric field».....	78
5.1 Introduction.....	78

5.2	Problem statement.....	80
5.3	Numerical results and discussion.....	83
5.3.1	Droplet oscillation.....	84
5.3.2	Droplet pseudo-rotation .....	87
5.3.3	Coalescence of two droplets .....	88
5.4	Experimental confirmation .....	93
5.4.1	Mixing of two droplets.....	94
5.5	Conclusions.....	96
	References.....	97
	Chapter 6.....	101
6	« Spreading and retraction control of charged dielectric droplets » .....	101
6.1	Introduction.....	101
6.2	Problem statement.....	104
6.3	Results.....	107
6.3.1	Spreading of charged dielectric droplet using vertical electric field .....	107
6.3.2	Retraction control of the charged dielectric droplets using vertical electric field .....	111
6.4	Conclusions.....	126
	References.....	127
	Chapter 7.....	131
7	« Head-on collision of electrically charged droplets ».....	131
7.1	Introduction.....	131
7.2	The mathematical model.....	133
7.3	Verification of the numerical method.....	135
7.4	Results and discussion .....	136
7.4.1	Two stationary conducting droplets.....	137

7.4.2	Impacting dielectric droplets.....	140
7.4.3	Unequal-size droplets: .....	146
7.5	Conclusions.....	148
	References.....	150
	Chapter 8.....	153
8	« Summary and recommendations for future study » .....	153
8.1	Summary.....	153
8.2	Recommendations for future studies .....	154
8.2.1	Frost removal using electric field .....	154
8.2.2	Separation of bio-particles in microfluidic chips.....	155
8.2.3	Coating.....	155
8.2.4	Hot-spot cooling.....	155
	References.....	157
	Curriculum Vitae .....	158

## List of Tables

Table 2.1 Summary of the boundary conditions .....	31
Table 3.1 List of experimental parameters .....	45
Table 4.1 Contact angles of a water droplet on different materials .....	66

## List of Figures

Figure 2.1 The exact volume-of-fluid function over a square grid.....	17
Figure 2.2 Representation of the level set function .....	19
Figure 2.3 Different 3D element types .....	30
Figure 3.1 Model of a suspended droplet in an electric field.....	41
Figure 3.2 Droplet breakup in NN6 configuration [13]: experimental data (left) and numerical results (right). The applied electric field strength is 4.5 kV/cm .....	46
Figure 3.3 Droplet breakup in NN21 configuration [13]: experimental data (left) and numerical results (right). The applied electric field strength is 3.2 kV/cm .....	46
Figure 3.4 Droplet deformation versus electric capillary number for $R=0.15$ , $S=1.38$ and $\lambda=1.31$ .....	48
Figure 3.5 Sequence of images showing the oscillation of the 1.3 mm droplet for $E=4$ kV/cm. (a) Observation normal to the applied electric field. (b) Observation parallel to the applied electric field.....	50
Figure 3.6 Frequency of droplet oscillation versus electric capillary number ( $Ca_E$ ) for $R=0.15$ , $S=1.38$ and $\lambda=1.31$ .....	51
Figure 3.7 Sequence of images showing the breakup of the 1.3 mm droplet for $E=7$ kV/cm.....	52
Figure 3.8 Critical electric capillary number as a function of the viscosity ratio for $S=1.38$ .....	54
Figure 3.9 Droplet shape for different conductivity ratios ( $R$ ) at $t=0.05$ s.....	54
Figure 3.10 Flow patterns of the droplet for $E=7$ kV/cm (XY view) .....	55
Figure 4.1 Force balance at the contact line .....	60

Figure 4.2 Model of a droplet deposited on a dielectric substrate and exposed to an electric field .....	62
Figure 4.3 Definition of the aspect ratio .....	65
Figure 4.4 Spherical drop geometry defined by radius $R$ and contact angle $\theta$ .....	66
Figure 4.5 Snapshots of numerical result for $\theta=110^\circ$ , $f=34$ Hz and $V=5$ kV .....	68
Figure 4.6 Aspect ratio $A_e/A_s$ as a function of the frequency of the applied AC electric field for $\theta=110^\circ$ .....	69
Figure 4.7 Snapshots of numerical result for $\theta=90^\circ$ , $f=40$ Hz and $V=5$ kV .....	70
Figure 4.8 Aspect ratio $A_e/A_s$ as a function of the frequency of the applied AC electric field for $\theta=90^\circ$ .....	70
Figure 4.9 Snapshots of a 10 $\mu$ l water droplet located on a surface with $\theta=100^\circ$ in (a) resonant frequency of 35 Hz and (b) commercial frequency of 50 Hz.....	72
Figure 4.10 Resonant frequencies as a function of the volume of the water droplet.....	73
Figure 5.1 Model of a sessile droplet in a rotating field (a) Top view, (b) 3-D model.....	81
Figure 5.2 Definition of the droplet width ( $W$ ) .....	82
Figure 5.3 Top view snapshots of the numerical results for a rotating droplet for $\theta=100^\circ$ and $f=35$ Hz.....	84
Figure 5.4 Droplet aspect ratio ( $A$ ) as a function of the time for different frequencies of electric field and contact angle $\theta=100^\circ$ .....	85
Figure 5.5 Droplet aspect ratio ( $A$ ) as a function of the time for different frequencies of electric field and contact angle $\theta=130^\circ$ .....	85
Figure 5.6 Effect of surface tension on droplet resonant frequency for $\theta=100^\circ$ .....	86

Figure 5.7 Comparison between the droplet oscillation frequency obtained from numerical simulation and Noblin’s expression.....	87
Figure 5.8 Fluid velocity vectors inside the droplet for $\theta=100^\circ$ and $f=25$ Hz.....	88
Figure 5.9 Schematic of two liquid droplets placed on a solid substrate subjected to rotating electric field. (a) Droplets position, (b) 3-D model.....	89
Figure 5.10 Time evolution of the first coalescence regime for $\theta=100^\circ$ , $\bar{f} = 1$ and $Ca_E=0.016$ .....	90
Figure 5.11 Time evolution of droplet shapes in the second coalescence regime for $\theta=100^\circ$ , $\bar{f} = 1.66$ and $Ca_E=0.016$ .....	91
Figure 5.12 $(\bar{f}, Ca_E)$ diagram for $\theta=100^\circ$ . The dashed lines correspond to the boundaries between two coalescence regimes. ....	92
Figure 5.13 $(\bar{f}, Ca_E)$ diagram for two different contact angles ( $\theta=130^\circ$ and $\theta=100^\circ$ ). The lines correspond to the boundaries between two coalescence regimes.....	92
Figure 5.14 Experimental set up for producing the rotating electric field.....	93
Figure 5.15 Clockwise pseudo-rotational motion of a droplet for $f=26$ Hz.....	94
Figure 5.16 Mixing of two droplets with ion-exchanged water and indigo carmin dyed water.....	95
Figure 5.17 Mixing time of two water droplets containing starch syrup to vary the viscosity. ....	96
Figure 6.1 Initial configuration used in numerical computations.....	107
Figure 6.2 Electrostatic spreading of a charged droplet placed on a surface ( $\theta=60^\circ$ ). ...	109
Figure 6.3 Dynamic spreading ratio of droplets with different surface charges in the presence of electric field $E=25$ kV/cm for $\theta=60^\circ$ .....	110



Figure 6.4 Effect of viscosity for $q/q_{Ray}=0.55$ and $E=25$ kV/cm .....	111
Figure 6.5 Computational domain for simulating a droplet impinging on horizontal surface.....	112
Figure 6.6 Experimental [17] (left) and simulated (right) shape of a water droplet impinging a super-hydrophobic surface.....	113
Figure 6.7 Comparison between the experimental [17] and numerical maximum spreading diameter .....	114
Figure 6.8 Comparison between the calculated spread diameter [5] and numerical results for the droplets impacting solid surface at different Weber numbers and the constant contact angle $\theta =100^\circ$ .....	115
Figure 6.9 Effect of surface contact angle on the maximum droplet spreading .....	115
Figure 6.10 Electric potential contour lines for different instants of time after the droplet impact.....	116
Figure 6.11 Impact of the electrically charged droplet on a surface with the contact angle of $\theta=100^\circ$ and exposed to an external electric field $E=25$ kV/cm.....	118
Figure 6.12 Dynamic spreading diameter droplets charged to different values in the presence of electric field $E=25$ kV/cm for $\theta=100^\circ$ , $We=364$ and $Re=80$ .....	119
Figure 6.13 Effect of impact velocity on the droplet spreading for $\theta=100^\circ$ and $q/q_{Ray}=0.8$ .....	120
Figure 6.14 Impact of the charged droplet on a surface with the contact angle of $\theta=60^\circ$ and $E=25$ kV/cm .....	122
Figure 6.15 Dynamic spreading ratio of droplets with different surface charges in the presence of electric field $E=25$ kV/cm for $\theta=60^\circ$ and $We=364$ .....	122

Figure 6.16 Effect of contact angle on spreading diameter for $q/q_{Ray}=0.28$ , $We=364$ and $E=25$ kV/cm .....	123
Figure 6.17 Spreading of a droplet impacting on a surface $\theta=60^\circ$ and subjected to an electric field $E=8.3$ kV/cm and $We=364$ .....	125
Figure 6.18 Dynamic spreading ratio of droplets with different surface charges in the presence of electric field $E=8.3$ kV/cm for $\theta=60^\circ$ and $We=364$ .....	125
Figure 7.1 Initial configuration used in numerical simulation of droplet impact .....	134
Figure 7.2 Pan and Suga simulation [18] (left) and our simulated (right) snapshots of head-on collision of two uncharged water droplets in air. The initial droplet diameter is $300 \mu\text{m}$ and the relative velocity of collision is $0.28$ m/s .....	136
Figure 7.3 Interaction between two identical spherical droplets with the same (A) and different charges (B) at an initial distance of $2.5$ radii between centers.....	138
Figure 7.4 Two identical spherical droplets with different charges at a larger distance of $2.7$ radii between the two centers, $q_1/q_{Ray}=0.1$ (bottom), $q_2/q_{Ray}=0.25$ (top) .....	139
Figure 7.5 The limit between attraction and repulsion regimes for two identical droplets .....	140
Figure 7.6 Shape evolution of the head-on collision of two equal-size droplets for $We=6.7$ , $Re=66.7$ and $q/q_{Ray}=0.5$ .....	141
Figure 7.7 Shape evolution of the head-on collision of two equal-size droplets for $We=13$ , $Re=94.3$ and $q/q_{Ray}=0.5$ .....	142
Figure 7.8 Shape evolution of the head-on collision of two equal-size droplets for $We=13$ , $Re=94.3$ and $q/q_{Ray}=0.7$ .....	142
Figure 7.9 The limit between coalescence and repulsion regimes for two identical impacting droplets with the initial distance of $d_0=4r$ .....	143

Figure 7.10 Shape evolution of the head-on collision of two neutral equal-size droplets for $We=106.7$ , $Re=266.67$ and $q/q_{Ray}=0$ .....	144
Figure 7.11 Shape evolution of the head-on collision of two equal-size droplets for $We=106.7$ , $Re=266.67$ and $q/q_{Ray}=0.3$ .....	145
Figure 7.12 Shape evolution of the head-on collision of two equal-size droplets for $We=106.7$ , $Re=266.67$ and $q/q_{Ray}=0.5$ .....	145
Figure 7.13 Computational domain for simulating collision of droplets with different size .....	147
Figure 7.14 Snapshots of droplet motion of larger (upper) and smaller (lower) neutral spherical droplets with $R_2/R_1=1.5$ at $We=160$ and $Re=400$ .....	147
Figure 7.15 Snapshots of droplet motions between a larger (upper) and a smaller (lower) neutral spherical droplets with $R_2/R_1=1.5$ at $We=360$ and $Re=600$ .....	148



## Chapter 1

### 1 « Introduction and objectives »

#### 1.1 Introduction

Electrohydrodynamics (EHD) is the study of the fluid flow caused by electric forces. The earliest record of an EHD experiment is in William Gilbert's seventeenth century treatise "De Magnete", which describes the formation of a conical shape upon bringing a charged rod above a sessile drop [1]. Later, Lord Rayleigh (1882) studied the deformation and the bursting of charged drops in an electric field [2]. In 1834, Faraday [3] demonstrated the electric wind using a particle stream between two electrodes. Later, Maxwell [4] proposed the analysis of the wind mechanism, which is still valid even today. The first to suggest the possibility of designing a functional electrostatic blower (i.e., an EHD pump) were Robinson [5] and Stuetzer [6], during their research on the ionic wind. The effects of EHD flow on the boundary layer and heat transfer were being considered at the same time as there were studies on EHD thrust engines [7]. Another application of EHD flow is an EHD micropump, which was fabricated and experimentally tested by Richter and Sandmaier [8].

EHD flows are a form of a multi-physics problem in which the electric forces are used to drive the fluid [9, 10]. The Maxwell stress tensor plays the crucial role of coupling the electrostatics and hydrodynamics, and the electric forces can be calculated using this tensor. Electrohydrodynamic transport phenomena are fundamental to a variety of engineering applications such as electrospray ionization, electro-coalescence, mixing of droplets, Lab on a Chip (LOC) devices and electrostatic printing.

Over the last decade, EHD flow has received much attention in the research community because of its widespread industrial applications. In what follows, the various applications of EHD that have emerged in different fields of engineering and science, specifically the electrohydrodynamics of droplets and their behavior under the effect of the electric field, will be briefly reviewed. The possibility of the existence of reversed

dipoles in droplets and different scenarios of droplet deformation based on the physical properties of the fluids are reviewed. The interaction of droplets with solid walls and droplets oscillations were investigated in terms of the surface properties, such as contact angle. The role of the surface contact angle on droplet oscillation and resonant frequency due to the electric field will be explained.

Another group of investigations has been devoted to the impacting of droplets on solid surfaces. Here the spreading and retraction of droplets and their manipulation using electric forces are considered. Finally, the droplet collision phenomena in electrospray atomization, turbine blade cooling and fuel injection as one of the EHD promising applications are also reviewed.

## 1.2 Thesis objectives

The overall objective of this thesis is to develop and implement a numerical method to tackle the complex EHD problems existing in many applications. Of particular interest was to model the droplet behavior under the effect of the electric forces in various circumstances in terms of the fluid mechanics. In each case, attempts were made to tune the numerical algorithm with the physical parameters involved. In most cases, the numerical algorithm has been confirmed with the available experimental data and the electric forces extension was added after getting the positive confirmation. The main contribution of the thesis is making the commercial software, COMSOL MULTIPHYSICS™, capable of handling different EHD phenomena. The following sections describe the background for each of the areas investigated.

### 1.2.1 Droplet deformation under the effect of electric field

An electric field can be used as one of the non-invasive and active methods to control the behaviour of droplets. A fluid droplet suspended in another immiscible fluid deforms, oscillates or breaks under the effect of a sufficiently strong electric field. The deformation can be either oblate or prolate depending on the physical properties of the droplet and ambient fluids (surface tension and viscosity) [11-13]. The electrical stress applied to the droplet surface may also cause the fluid tangential motion at the surface, resulting in a strong circulating flow and fluid mixing.

Taylor [14] introduced a small deformation theory based on the leaky dielectric model of the fluid to theoretically describe the deformation of the droplets in weak electric fields. This model does not fully capture all phenomena that have been observed in experiments. In strong fields a nonaxisymmetric rotational flow may appear. Recent experimental studies have discovered non-axisymmetric shapes for the droplets [15-18]. It was found that the symmetry breaking happens due to a reverse dipole created inside the droplet. In the case of a rigid sphere, this results in physical rotation of a particle known as Quincke rotation [19]. This configuration becomes unstable above some critical strength of the electric field. It is clear that the rotation of the droplet with an axis oblique to the applied electric field will destroy the axisymmetric conditions. In order to have a comprehensive understanding of the problem, a full 3D simulation is needed. Recently a rare example of chaos under creeping flow conditions was found [20], which could find applications in small-scale fluid mixing and electromanipulation of particle motion in microfluidic technologies.

### 1.2.2 Electrowetting and oscillations of droplets on insulating surfaces

Electrowetting is the process of modification of the surface wetting properties caused by an applied electric field. More than one century ago, Lippmann [21] discovered that wetting can be effectively controlled by an electric field and also observed that the surface tension of the interface between acidic water and mercury is a function of the potential difference at this interface. Since Lippmann's findings, electrocapillary phenomenon, or electrowetting, has developed into a series of tools for manipulating microdroplets on solid surfaces. Many chemical or physical methods have been developed to control the wettability of surfaces [22-24], but in these cases the wettability cannot be controlled after being manufactured.

When a liquid droplet is slowly placed on a solid, flat substrate, it spreads to its equilibrium configuration with the contact angle specified by Young's equation [25]. Electrowetting is one of the best methods to control the wetting behavior of liquid droplets on partially wetting surfaces by reducing the apparent contact angle of sessile droplets [26, 27]. Applications of electrowetting include reprogrammable lab-on-a-chip

systems [28], autofocus cell phone lenses [29], colored oil pixels for laptops and video-speed smart paper [30, 31].

In principle, electrowetting can be applied in two different scenarios: 1) droplets sitting on a metal electrode, or 2) on a thin dielectric layer on top of an electrode. However, most of the recent electrowetting studies and applications have been carried out on a dielectric surface; electrowetting-on-dielectric (EWOD) has been the subject of the majority of the studies in this field.

Tiny droplets can be used as a medium for biochemical reactions as well as containers of biological particles. Using a patterned electrode array, droplets can be transported, mixed and split by controlling the contact angle in electrowetting [32-35].

Using AC electric fields, the droplets undergo an oscillatory force which results in the oscillation of the droplets placed on solid surfaces. The importance of this kind of oscillation can be found in studies related to high voltage outdoor insulators [36-39]. The flow field generated during droplet oscillation at low AC frequencies can also be used to enhance the mixing in a droplet [40, 41].

### 1.2.3 Droplets impacting on solid surfaces

The impacting and spreading of liquid drops on solid surfaces are important processes in many applications, such as spray coating, delivery of agricultural chemicals, ink jet printing and rapid spray cooling of heated targets [42, 44]. In recent years, inkjet technology has been employed to deposit functional materials, which are mixed with liquid, directly on a solid substrate. Example applications of inkjet printing include manufacturing of light-emitting diode (LED) display panel [45, 46] and DNA micro-arrays [47, 48].

The impact of liquid droplets on solid surfaces can be categorized into spreading, recoil, rebound and splashing. One of the most important parameters relevant to the applications mentioned earlier is the maximum spreading diameter  $D_{max}$  which is often normalized to the original diameter of the droplet prior to impact. Several experimental and theoretical studies can be found in the literature on passive retraction control of aqueous droplets on hydrophobic surfaces [49, 52].



Electric forces can be utilized to control the droplet behavior after its impact onto the surface. The effect of corona discharge on the spreading and retraction control of dielectric drops has been also experimentally investigated by Mahmoudi et al. [53, 54]. Thermal management is also a critical issue in integrated circuit design. Droplets can be used to target different sections on circuits to cool down the device [55, 56]. Different correlations for the time evolution of the spread diameter can be found in the literature [57, 60].

#### 1.2.4 Droplet collisions

Droplet collision is an important part of many applications from understanding cloud formation in climate theory [61, 62] to engineering applications such as electrospray atomization, turbine blade cooling and fuel injection [63-68]. In engines, droplet collision is one of the key factors in determining the spray characteristics, which largely affects the mixture formation and combustion process. Therefore, understanding the mechanism of droplet collision is of great interest and significance. A detailed summary of relevant experimental investigations can be found in [69].

The collision of Newtonian fluid droplets has been investigated both experimentally and numerically for decades. In general, the outcome of the droplet collisions can be categorized into four different types: bouncing, coalescence, separation, and shattering collisions. At higher Weber number for head-on or near head-on cases, reflexive separation may happen resulting in formation of satellites. Ashgriz and Poo [70] developed models for predicting the boundary between the coalescence and separation regimes.

Although experimental studies can monitor the time evolution of the droplets in collision phenomena using high speed cameras, the details of what happens inside the drops can hardly be accessed. Numerical investigations can produce more details of the pressure and velocity field inside the droplets before and after impact.

Over the years, the collision of charged droplets has always been an interesting subject. The feasibility of coalescence of two perfectly conducting, electrically charged droplets was studied from a thermodynamic point of view by Gallily et al. [71]. An analytical expression was developed for the electrical energy of the two droplets, which make the

initial contact. Recently, some interesting features during collision of charged droplets and particles have been presented in different research papers. For example it was even proven by Lekner [72] that under certain conditions two charged conducting spheres can attract each other at close approach.

Faeth [73] and O'Rourke and Bracco [74] emphasized the importance of droplet collision phenomena occurring within dense sprays and recognized the significance of the rheological properties of the droplets (i.e. hydrocarbons vs. water).

### 1.3 Thesis outline

The main subject of Chapter 2 is to introduce the numerical approach used in this thesis. Chapter 3 focuses on the deformation of suspended droplets considering different mechanical and electrical characteristics of the fluids. The behavior of droplets placed on solid surfaces is investigated in Chapters 4 and 5. The effect of the surface properties, such as the contact angle, has been investigated in these two chapters and the numerical scheme is improved accordingly. Chapter 6 covers the recent technique for spreading and retraction control of droplets using electrostatic forces. Chapter 7 proves the feasibility of applying the Level-Set method as a numerical technique to investigate the collision dynamics of electrically charged droplets. It is demonstrated that the presented numerical method is able to capture the droplet collision in the presence of the electric charges on the surface of the droplets. The complete dissertation comprises the following major sections:

#### **Chapter 2**

This chapter provides a brief review of various two-phase modeling methods available in the literature. Also, the specific method used in the current project is described in detail. This chapter covers the numerical technique implemented in COMSOL, a finite-element software, to simulate the complicated physical processes in the next chapters.

#### **Chapter 3**

There has been relatively little work previously reported on the breakup of a less conducting droplet via the oblate-type deformation. In this chapter, the 3-D deformation, oscillation and breakup of an initially uncharged and spherical droplet suspended in

another immiscible fluid with higher conductivity, under DC uniform electric field is numerically investigated. It is the first time that the deformation of such droplet is investigated numerically in a 3D configuration.

#### **Chapter 4**

The 3-D oscillations of a water droplet on a solid surface under the effect of external fields, such as gravity and a sinusoidal electric field, were investigated numerically. The electric field introduces additional interfacial stresses at the droplet interface and extensive computations were performed to assess the combined effects of electric fields, surface tension and inertia. It was found that the resonance frequency and the magnitude of the deformation strongly depend on the surface properties and the value of contact angle. A comparison of the numerical results with the known experimental data shows satisfactory agreement with respect to the shape of the droplet and the resonant frequencies.

#### **Chapter 5**

This chapter reports the 3-D oscillations and coalescence of water droplets deposited on a dielectric substrate under the effect of a rotating electric field, taking into account the effect of frequency of the applied AC voltage and the value of the contact angle. The time variation of the shape of a perfectly conducting droplet placed between two orthogonal pairs of parallel electrodes with two-phase voltage excitation was investigated. This chapter also presents a new design of an electrowetting mixer using the rotating electric field and offers a new method to effectively mix two droplets over a different range of AC frequencies.

#### **Chapter 6**

The dynamics of spreading and impact of a dielectric droplet onto a dry conductive substrate in the presence of an external vertical electric field was investigated numerically. The effects of electric field strength, surface charge, droplet properties and surface wettability were taken into account. In the first part, the spreading of a charged dielectric droplet placed on a ground electrode was simulated. In the second part, the suppression of the droplet receding phase, after it has been impacted onto a surface with

some velocity, was investigated assuming that the droplet is electrically charged and exposed to an electric field parallel to the impact axis.

### **Chapter 7**

The interaction between two identical charged droplets was investigated numerically. Numerical simulation shows that two conducting droplets carrying charges of the same polarity under some conditions may be electrically attracted confirming the recent theoretical predictions. The effects of the impact velocity, drop size ratio and electric charge on the behavior of the combined droplet were investigated.

### **Chapter 8**

This chapter summarizes the major findings of this work and proposes possible future research directions.

## References

- [1] W. Gilbert, *De Magnete* (Dover, New York, 1958), Vol. II, Chap. II, p. 89, first published ca. 1600, translated by P. F. Mottelay in 1893.
- [2] L. Rayleigh, "On the equilibrium of liquid conducting masses charged with electricity", *Phil. Mag. Ser.*, vol. 14, no. 87, pp. 184-186, 1882.
- [3] M. Faraday, "Experimental Researches in Electricity", Carlsbad, CA, USA: Faraday, 1834.
- [4] J. C. Maxwell, "Treatise in Electricity and Magnetism", Oxford, U.K.: Oxford Univ. Press, 1873.
- [5] M. Robinson, "Movement of Air in the Electric Wind of the Corona Discharge", Somerville, NJ, USA: Hamon Research-Cottrell, 1960.
- [6] O. M. Stuetzer, "Ion drag pumps," *J. Appl. Phys.*, vol. 31, no. 1, pp. 136-146, 1960.
- [7] E. K. Levy, "The effects of electrostatic fields on forced convection heat transfer," Ph.D. dissertation, Dept. Mech. Eng., Massachusetts Inst. Technol., Minneapolis, MN, USA, 1964.
- [8] A. Richter and H. Sandmaier, "An electrohydrodynamic micropump", *Proc. Invest. Micro Struct., Sensors, Actuat., Mach. Robots Micro Electro Mech. Syst.*, Napa Valley, CA, USA, pp. 99-104, 1990.
- [9] J. R. Melcher and G I Taylor, "Electrohydrodynamics: A Review of the Role of Interfacial Shear Stresses", *Annu. Rev. Fluid Mech.*, vol. 1, pp. 111-146, 1969.
- [10] D. A. Saville, "Electrohydrodynamics: The Taylor-Melcher Leaky Dielectric Model", *Annu. Rev. Fluid Mech.*, vol. 29, pp. 27-64, 1997.
- [11] J. C. Baygents, N. J. Rivette and H. A. Stone, "Electrohydrodynamic deformation and interaction of drop pairs", *J. Fluid Mech.* vol. 368, pp. 359-375, 1998.
- [12] S. Torza, R. G. Cox and S. G. Mason, "Electrohydrodynamic deformation and burst of liquid drops", *Philos. Trans. R. Soc. London, Ser. A*, vol. 269, no. 1198, pp. 295-319, 1971.
- [13] O. Vizika and D. A. Saville, "The electrohydrodynamic deformation of drops suspended in liquids in steady and oscillatory electric fields," *J. Fluid Mech.*, vol. 239, pp. 1-21, 1992.

- [14] G. I. Taylor, "Studies in electrohydrodynamics. I. Circulation produced in a drop by an electric field", *Proc. R. Soc. London, Ser. A*, vol. 291, no. 1425, pp. 159-166, 1966.
- [15] S. Krause and P. Chandratreya, "Electrorotation of deformable fluid droplets," *J. Colloid Interface Sci.*, vol. 206, no. 1, pp. 10-18, 1998.
- [16] J. W. Ha and S. M. Yang, "Electrohydrodynamics and electrorotation of a drop with fluid less conductive than that of the ambient fluid", *Phys. Fluids*, vol. 12, no. 4, pp. 764-771, 2000.
- [17] H. Sato, N. Kaji, T. Mochizuki and Y. H. Mori, "Behavior of oblatelly deformed droplets in an immiscible dielectric liquid under a steady and uniform electric field", *Phys. Fluids.*, vol. 18, 127101, 2006.
- [18] P. F. Salipante and P. M. Vlahovska, "Electrohydrodynamics of drops in strong uniform DC electric fields", *Phys. Fluids*, vol. 22, 112110, 2010.
- [19] G. Quincke, "Ueber rotation em im constanten electrischen felde," *Ann. Phys. Chem.*, vol. 59, pp. 417-86, 1896.
- [20] P. F. Salipante and P. M. Vlahovska, "Electrohydrodynamic rotations of a viscous droplet", *Phys. Rev. E*, vol. 88, 043003, 2013.
- [21] G. Lippmann, "Relations entre les phénomènes électriques et capillaires", *Ann. Chim. Phys.*, vol. 5, pp. 494-549, 1875.
- [22] J. Bico, C. Tordeux and D. Quere, "Rough wetting", *Europhys. Lett.*, vol. 55, no. 2, pp. 214-220, 2001.
- [23] D. Bonn, J. Eggers, J. Indekeu, J. Meunier and E. Rolley, "Wetting and spreading", *Rev Mod Phys.*, vol. 81, pp. 739-805, 2009.
- [24] D. Quere, "Wetting and roughness", *Annu. Rev. Mat. Research*, vol. 38, pp. 71-99, 2008.
- [25] T. Young, "An essay on the cohesion of fluids", *Philos Trans R Soc A*, vol. 95, pp. 65-87, 1805.
- [26] F. Mugele and J. C. Bare, "Electrowetting: from basics to applications", *J. Phys.: Condens. Matter*, vol. 17, pp. 705-774, 2005.
- [27] C. Quilliet and B. Berge, "Electrowetting: a recent outbreak", *Curr. Opin. Colloid Interface Sci.*, vol. 6, no. 1, pp. 34-39, 2001.

- [28] J. Lee, H. Moon, J. Fowler, T. Schoellhammer and C. J. Kim, "Electrowetting and electrowetting on dielectric for microscale liquid handling", *Sens. Actuators A.*, vol. 95, no.2-3, pp. 259-268, 2002.
- [29] B. Berge and J. Peseux, "Variable focal lens controlled by an external voltage: An application of electrowetting", *Eur. Phys. J. E*, vol. 3, pp. 159-163, 2000.
- [30] R. A. Hayes and B. J. Feenstra, "Video-speed electronic paper based on electrowetting", *Nature London*, vol. 425, pp. 383-385, 2003.
- [31] T. Roques Carmes, R. A. Hayes, B. J. Feenstra and L. J. M. Schlangen, "Liquid behavior inside a reflective display pixel based on electrowetting", *J. Appl. Phys.*, vol. 95, no. 8, pp. 43-89, 2004.
- [32] M. G. Pollack, R. B. Fair and A.D. Shenderov, "Electrowetting-based actuation of liquid droplets for microfluidic applications", *Appl. Phys. Lett.*, vol. 77, no. 11, pp. 1725-1727, 2000.
- [33] S. K. Cho, H. Moon and C. J. Kim, "Creating, transporting, cutting, and merging liquid droplets by electrowetting-based actuation for digital microfluidic circuits", *J. of Microelectromech. Sys.*, vol. 12, no. 1, 70-80, 2003.
- [34] F. Mugele, J. C. Baret and D. Steinhauser, "Microfluidic mixing through electrowetting-induced droplet oscillations", *Appl. Phys. Lett.*, vol. 88, 204106, 2006.
- [35] K. P. Nichols and Han J. G. E. Gardeniers, "A digital microfluidic system for the investigation of pre-steady-state enzyme kinetics using rapid quenching with MALDI-TOF mass spectrometry", *Anal. Chem.*, vol. 79, no. 22, pp. 8699-8704, 2007.
- [36] S. Keim, D. Koenig and V. Hinrichsen, "Experimental Investigations on Electrohydrodynamic Phenomena at Single Droplets on Insulating Surfaces", *IEEE. Conf. Electr. Insul. Dielectr. Phenom*, pp.133-136, 2003.
- [37] R. Sundararajan, S. Sundhur and T. Asokan, "Electrohydrodynamics of Water Droplets on Polymer Surfaces", *IEEE. 34<sup>th</sup> IAS Annual Meeting, Indust. App. Conf*, vol. 3, pp. 1817-1824, 1999.
- [38] S. Feier-Iova, "The Behavior of Water Droplet on Insulating Surfaces Stressed by Electric Field", *Ph.D. Thesis, TU-Darmstadt*, 2009. <http://tuprints.ulb.tu-darmstadt.de/2008/>

- [39] A. M. Imano and A. Beroual, “Deformation of Water Droplets on Solid Surface in Electric Field”, *J. Colloid and Interface Sci.*, vol. 298, no. 2, pp. 869-879, 2006.
- [40] H. Lee, S. Yun, S. H. Ko and K. H. Kang, “An electrohydrodynamic flow in AC electrowetting”, *Biomicrofluid.*, vol. 3, 044113-044125, 2009.
- [41] P. García-Sánchez, A. Ramos and F. Mugele, “Electrothermally driven flows in AC electrowetting”, *Phys. Rev. Lett E*, vol. 81, pp. 015303 (4 pp), 2010.
- [42] A. Frohn and R. Roth, “Dynamics of Droplets Springer”, Berlin, 2000.
- [43] J. D. Bernardin, C. J. Stebbins and I. Mudawar, “Mapping of impact and heat transfer regimes of water drops impinging on a polished surface”, *Int. J. Heat Mass Transfer*, vol. 40, no. 2, pp. 247267, 1997.
- [44] G. Xie, L. Luo, S. Liu, D. Guo, C. Zhang and L. Si, “Electrospreading of dielectric liquid menisci on the small scale”, *Soft Matter*, vol. 7, pp. 6076-6081, 2011.
- [45] H. S. Koo, M. Chen, P. C. Pan, L. T. Chou, F. M. Wu, S. J. Chang and T. Kawai, “Fabrication and chromatic characteristics of the greenish LCD colour-filter layer with nano-particle ink using inkjet printing technique”, *Displays*, vol. 27, no. 3, pp. 124-129, 2006.
- [46] S. Ummartyotin, J. Juntaro, C. Wu, M. Sain, H. Manuspiya, “Deposition of PEDOT: PSS nanoparticles as a conductive microlayer anode in OLEDs device by desktop inkjet printer”, *J Nanomater*, vol. 2011, pp. 606714-606721, 2011
- [47] M. J. Heller, “DNA microarray technology: devices, systems, and applications”, *Annu. Rev. Biomed. Eng.*, vol. 4, no. 1, pp. 129–153, 2002.
- [48] A. Kumar, G. Goel, E. Fehrenbach, A. K. Puniya, K. Singh, “Microarrays: the technology, analysis and application”, *Eng Life Sci.*, vol. 5, no. 3, pp. 215-222, 2005.
- [49] A. Carre, J. Gastel and M. Shanahan, “Viscoelastic effects in the spreading of liquids”, *Nature*, vol. 379, pp. 432-434, 1996.
- [50] V. Bergeron, D. Bonn, J. Yves Martin and L. Vovelle, “Controlling droplet deposition with polymer additives,” *Nature*, vol. 405, pp. 772-775, 2000.
- [51] D. Bartolo, A. Boudaoud, G. Narcy and D. Bonn, “Dynamics of non-Newtonian droplets”, *Phys. Rev. Lett.*, vol. 99, pp. 174502, 2007.
- [52] M. I. Smith and V. Bertola, “Effect of polymer additives on the wetting of impacting droplets,” *Phys. Rev. Lett.*, vol. 104, pp. 154502, 2010.



- [53] S. R. Mahmoudi, K. Adamiak and G. S. P. Castle, "Spreading of a dielectric droplet through an interfacial electric pressure", *Proc. R. Soc.*, vol. 467, pp. 3257, 2011.
- [54] S. R. Mahmoudi, G. S. P. Castle and K. Adamiak, "Retraction control of an impacted dielectric droplet through electrical pressure", *Soft Matter*, vol. 8, no. 3, pp. 808-813, 2012.
- [55] V.K. Pamula and K. Chakrabarty, "Cooling of integrated circuits using droplet-based microfluidics", *Proc. ACM Great Lakes Symposium on VLSI*, pp. 84-87, 2003.
- [56] P. Paik, V. K. Pamula and K. Chakrabarty, "Thermal effects on droplet transport in digital microfluidics with applications to chip cooling processing for integrated microfluidics", *International Conference on Thermal, Mechanics, and Thermomechanical Phenomena in Electronic Systems (ITherm)*, pp. 649-654, 2004.
- [57] C. Clanet, C. Beguin, D. Richard and D. Quere, "Maximal deformation of an impacting drop," *J. Fluid Mech.*, vol. 517, pp. 199-208, 2004.
- [58] T. Mao, D. Kuhn and H. Tran, "Spread and rebound of liquid droplets upon impact on flat surfaces", *AIChE J.*, vol. 43, no. 9, pp. 2169-2179, 1997.
- [59] M. Pasandideh-Fard, Y. Qiao, S. Chandra and J. Mostaghimi, "Capillary effects during droplet impact on a solid surface", *Phys. Fluids*, vol. 8, pp. 650-659, 1996.
- [60] P. Attane, F. Girard and V. Morin, "An energy balance approach of the dynamics of drop impact on a solid surface", *Phys. Fluids*, vol. 19, pp. 012101-17, 2007.
- [61] B. A. Tinsley, R. P. Rourbaugh, M. Hei, and K. V. Beard, "Effects of image charges on the scavenging of aerosol particles by cloud droplets and on droplet charging and possible ice nucleation processes", *J. Atmos. Sci.*, vol. 57, no. 13, pp. 2118-2134, 2000.
- [62] K. V. Beard, R. I. Durkee, and H. T. Ochs, "Coalescence efficiency measurements for minimally charged cloud drops", *J. Atmos. Sci.*, vol. 59, no. 2, pp. 233-243, 2002.
- [63] L. D. Juan and J. Fernandez De La Mora, "Charge and size distributions of electrospray drops", *J. Colloid Interface Sci.*, vol. 186, no. 2, pp. 280-293, 1997.
- [64] N. V. Krasnov and S. I. Shevchenko, "Comprehensive studies of electrohydrodynamic spraying of liquids", *Rev. Sci. Instrum.*, vol. 66, 3623-3626, 1995.
- [65] H. Okuda and A. J. Kelly, "Electrostatic atomization: Experiment, theory and industrial applications", *Phys. Plasmas*, vol. 3, pp. 2191-2196, 1996.

- [66] J. S. Eow, M. Ghadiri and A. Sharif, "Experimental studies of deformation and break-up of aqueous drops in high electric fields", *Colloids Surf. A*, vol. 225, pp. 193-210, 2003.
- [67] B. F. Lin, J. H. Huang and D. Y. Huang, "Experimental study of the effects of vegetable oil methyl ester on DI diesel engine performance characteristics and pollutant emissions", *Fuel*, vol. 88, pp. 1779-1785, 2009.
- [68] C. Oner and S. Altun, "Biodiesel production from inedible animal tallow and an experimental investigation of its use as alternative fuel in a direct injection diesel engine", *Appl. Energy*, vol. 86, no. 10, pp. 2114-2120, 2009.
- [69] N. Ashgriz, "Handbook of Atomization and Sprays", first ed., Springer, New York, pp. 157-181, 2011.
- [70] N. Ashgriz and J.Y. Poo, "Coalescence and separation in binary collision of liquid drops", *J. Fluid. Mech.*, vol. 221, pp. 183-204, 1990.
- [71] I. Gallil and G. Ailam (Volinez), "On the coalescence of electrically charged droplets", *J. of Colloid and Interface Science*, vol. 30, no. 4, pp. 537-545, 1969.
- [72] J. Lekner, "Electrostatics of two charged conducting spheres", *Proc. R. Soc. A*, pp. 0133, 2012.
- [73] G. M. Faeth, "Current status of droplet and liquid combustion", *Prog. Energy Combust. Sci.*, vol. 3, no. 4, pp. 191-224, 1977.
- [74] P. J. O'Rourke and F. V. Bracco, "Modeling of droplet interactions in thick sprays and a comparison with experiments", *Stratified Charge Auto. Eng. Conf.*, pp. 101-115 *Inst. Mech. Eng. Pub.*

## Chapter 2

### 2 «Numerical models in simulating electrohydrodynamics of droplets»

As discussed in Chapter 1, liquid/gas interfaces occur in a wide variety of natural phenomena and technical processes such as inkjets, evaporators and boilers. Two-phase flow modeling faces a number of challenges, such as having an extremely thin phase interface, large density change across the interface and topology changes. It is imperative to develop a numerical simulation method that provides an optimal solution to such a complex problem. The challenge is to resolve the interface features accurately without any artifacts. The bulk of the phases can be simulated using well-known methods, such as finite volumes, finite elements and finite differences. However, the interface requires a special numerical treatment due to problems in determining the location of the discontinuity and computation of surface stresses [1]. An under-resolved interface might imbalance the surface-stress conditions, which leads to spurious parasitic currents [2]. In contrast, trying to resolve features accurately could pose numerical stability issues and high computational cost. Hence, for problems involving interfaces, there is a trade-off between accuracy and computational cost. Modeling of two phase flow is still under development.

Existing numerical methods used to solve two-phase flow problems include the Front-Tracking method [3-5], Boundary Integral Method [6, 7], Finite Element Method [8, 9], Volume of Fluid Method [10-13], Phase Field Method [14, 15], Lattice Boltzmann Method [16] and Level-Set method [19-26].

Only a limited number of the multiphase EHD flow problems within an idealized setting can be solved analytically, for example, predicting a small deformation of a single droplet in a uniform electric field [27]. Numerical simulations are required to obtain solutions for the flow systems involving two fluids with different properties and studying the multiphase EHD flow. This chapter provides a brief review of various two-phase modeling methods available in the literature. Also, the specific method used in the

present study is described in detail. The electrohydrodynamics equations in two-phase flows and coupling of the hydrodynamic and electrostatic phenomena have also been reviewed.

## 2.1 Modeling methods for two-phase flow

The two-phase flow modeling methods can be broadly classified into three categories based on how the interface is tracked [28]:

1. Eulerian methods,
2. Lagrangian methods, and
3. Combined Lagrangian-Eulerian methods

Eulerian methods are based on a fixed grid which is not moving with the interface. Methods using moving grid to track the interface explicitly are called Lagrangian. The interface is a representation of the boundary between two different phases. In Lagrangian modeling, the computational grid is fitted to the interface and equations are solved in this grid to track the interface. A large interface deformation and topology change can both lead to numerical instability and high computational time due to the need of the remeshing at each stage.

The combined Lagrangian-Eulerian methods use some aspects of the both. The computations are carried out on a fixed grid while the interface is being tracked explicitly. The combined version is suitable for tracking moving rigid bodies as there is no sharp deformation on the interface. There are also some other methods in which no grid is used, like particle methods. The key idea of these meshless methods is to seek accurate and stable numerical solutions for integral equations or partial differential equations (PDEs) through using a set of nodes (or particles) rather than any grid.

Eulerian methods are more preferred because of lower computational cost and their easy implementations. They can be classified into front tracking and front capturing methods. In front tracking methods, the interface is tracked explicitly using supplementary Lagrangian surface grids. On the other hand, front capturing methods use the field

variables like volume fraction and distance-functions to reconstruct the interface from the fixed grid at each time step. Although front tracking methods are more accurate, not being able to handle the topology changes like breaking or coalescence of droplets is their significant drawback and will not be considered in this thesis. Volume-of-Fluid (VOF) and Level-Set methods are among the most popular front capturing methods which will be discussed here.

### 2.1.1 Volume-of-Fluid (VOF) method

In this method, which was originally developed by Hirt and Nichols [29], a volume-fraction function is defined and advected through the fixed grid. This function has a value of one on one side, zero on the other side of the interface and a fractional value on the interface. An example of its implementation is shown in Figure 2.1. The interface is reconstructed using the updated mass fractions.

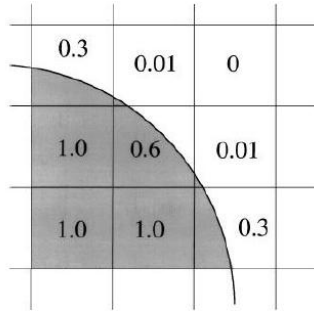


Figure 2.1 The exact volume-of-fluid function over a square grid

The volume fraction function is governed by

$$\frac{\partial \alpha}{\partial t} + \mathbf{u} \cdot \nabla \alpha = 0 \quad (2.1)$$

where  $\mathbf{u}$  is the fluid velocity. The physical property changes smoothly from the value on one side of the interface to the value on the other side in the interfacial transitional zone following the relations

$$\rho = \alpha \rho_l + (1 - \alpha) \rho_g \quad (2.2)$$

$$\mu = \alpha\mu_l + (1 - \alpha)\mu_g \quad (2.3)$$

where  $\rho_l, \rho_g$  and  $\mu_l, \mu_g$  are densities and viscosities of the reference phase and the secondary phase, respectively.

Some of the advantages of the VOF methods are:

1. The mass can be conserved.
2. The topology changes can be handled.
3. It can be easily extended to 3-D formulation.

The challenges are in making the initial approximation of the interface and interface reconstruction in order to determine the weighted value of density and viscosity in each cell. Different reconstruction methods can impose large errors in computed variables.

### 2.1.2 Level-Set method

The Level-Set method (LSM) is one of the most powerful techniques for fixed grid systems. It was developed by Osher and Sethian [19, 30] to track the interface on an Eulerian grid. LSMs are particularly useful for problems in which the topology of the evolving interface changes during the course of events and for problems in which sharp corners and cusps are present. This method is also excellent in accurately computing problems with surface tension.

It employs the concept of a signed distance function  $\phi$  which has a value of zero on the interface, which is called zero level-set. It has positive values on one side and negative values on the other to distinguish between the two different phases as conceptually shown in Figure 2.2.

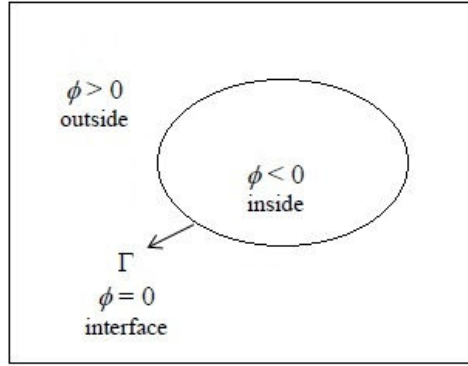


Figure 2.2 Representation of the level set function

The level set function is governed by

$$\frac{\partial \phi}{\partial t} + \nabla \cdot (\phi \mathbf{u}) = 0 \quad (2.4)$$

and if the flow is incompressible ( $\nabla \cdot \mathbf{u} = 0$ ), it can be rewritten as

$$\frac{\partial \phi}{\partial t} + \mathbf{u} \cdot \nabla \phi = 0 \quad (2.5)$$

To keep the level set function a distance function, a reinitialization process is needed. Ideally, the interface should not change its position during this reinitialization procedure. However in many applications the zero level set function can become distorted by parasitic numerical inaccuracies, if the gradients in the neighborhood of the interface are either very large or very small. For this reason, an improved reinitialization method was used [31, 32]. It was observed that the level set approach can treat even highly distorted interface and topology changes are automatically incorporated.

One of the disadvantages of this method is the mass conservation problem. Olsson et al. [33, 34] reduced the mass conservation errors by replacing the usual signed distance function with a hyperbolic tangent function. Some other researchers reduced the mass loss of the Level-Set method by coupling another method with a good mass conservation property, such as the volume of fluid method [35-40], front-tracking method [41, 42] or marker particles method [43].

The research is ongoing in this topic, and improvements and alternatives are much needed. Another approach is using the conservative LSM, which is how this technique is implemented in the commercial finite element software, COMSOL.

### 2.1.3 Conservative Level-Set method

The original LSM can be modified to improve the mass conservation by introducing a smeared out Heaviside step function. The level set function based on this has a value of one on one side and zero on other fluid. Across the interface, there is a smooth transition from zero to one. The interface is defined by the 0.5 isocontour, or level set, of  $\phi$ . The results of Olsson and Kreiss [33] show a significant improvement in the mass conservation properties of this method.

The laminar two-phase flow system studied in this thesis is coupled with the applied electric field and electric charges on the interface. Additional body forces are added to the Navier-Stokes equations for considering the surface tension ( $\mathbf{F}_{st}$ ) and electric stress ( $\mathbf{F}_{es}$ ).

$$\rho \frac{\partial \mathbf{u}}{\partial t} + \rho(\mathbf{u} \cdot \nabla)\mathbf{u} = \nabla \cdot [-P\mathbf{I} + \mu(\nabla\mathbf{u} + (\nabla\mathbf{u})^T)] + \mathbf{F}_{st} + \mathbf{F}_{es}$$

$$\nabla \cdot \mathbf{u} = 0$$
(2.6)

where  $\mathbf{u}$  denotes fluid velocity,  $\mathbf{I}$  is the identity matrix,  $\rho$  is the fluid density,  $\mu$  is the dynamic viscosity and  $P$  is the pressure.

The interface between the fluids is treated as a *free boundary* that evolves in time. The density and dynamic viscosity are represented as a function of the level set function  $\phi$  [32] as follows:

$$\rho = \rho_1 + (\rho_2 - \rho_1)\phi$$

$$\mu = \mu_1 + (\mu_2 - \mu_1)\phi$$
(2.7)

where  $\rho_{1,2}$ ,  $\mu_{1,2}$  are the density and dynamic viscosity of fluid 1 and 2 respectively.



In COMSOL, the motion of the interface is governed by a single combined advection-reinitialisation equation:

$$\frac{\partial \phi}{\partial t} + \mathbf{u} \cdot \nabla \phi = \gamma \nabla \cdot (\epsilon \nabla \phi - \phi(1 - \phi) \frac{\nabla \phi}{|\nabla \phi|}) \quad (2.8)$$

In most LSMs the right-hand side of Eq. (2-8) is zero, while in the method proposed by Olsson and her colleagues [34], the right-hand side is necessary for keeping the thickness of interface finite and for numerical stability.

Thus the terms on the left-hand side give the correct motion of the interface, while those on the right-hand side are necessary for numerical stability. The parameter  $\epsilon$  determines the thickness of the region where  $\phi$  varies smoothly from zero to one and is typically of the same order as the size of the elements of the mesh. By default,  $\epsilon$  is constant within each domain and equals the largest value of the mesh size,  $h$ , within the domain. The parameter  $\gamma$  determines the amount of reinitialization or stabilization of the level set function. It needs to be tuned for each specific problem. If  $\gamma$  is too small, the thickness of the interface might not remain constant and oscillations in  $\phi$  can appear because of numerical instabilities. On the other hand, if  $\gamma$  is too large the interface moves incorrectly. A suitable value for  $\gamma$  is the maximum magnitude of the velocity field  $\mathbf{u}$ .

In COMSOL, if the study type “*Transient with Initialization*” is used in the model, the level set variable is first initialized so that it varies smoothly between zero and one over the interface. It is equal to one inside the droplet, and zero outside the droplet and smoothly transformed within the diffuse interface with a certain thickness. For that condition, two study steps are created, “*Phase Initialization*” and “*Time Dependent*”. The Phase Initialization step solves for the distance to the initial interface,  $D_{wi}$ . The Time Dependent step then uses the initial condition for the level set function according to the following expression:

$$\phi_0 = \frac{1}{1 + e^{-D_{wi}/\epsilon}} \quad (2.9)$$

in domains initially outside the interface and

$$\phi_0 = \frac{1}{1 + e^{D_{wi}/\epsilon}} \quad (2.10)$$

in domains initially inside the interface. Here, inside refers to domains where  $\phi < 0.5$  and outside refers to domains where  $\phi > 0.5$ .

The level set function can be chosen to be the signed distance function from the interface. That means the smallest distance between a given point in the domain and the interface.

$$|\phi(r)| = d(r) = \min(|r - r_l|) \quad (2.11)$$

The level set function is positive on one side of the interface,  $\phi(r) > 0$ , and negative on the other,  $\phi(r) < 0$ . To represent the density and the viscosity in the two phases one has to use a Heaviside function

$$H(\phi) = \begin{cases} 0, & \phi < 0 \\ 1, & \phi > 0 \end{cases} \quad (2.12)$$

In numerical simulations, the abrupt jump in the fields due to Eq. (2.12) will cause instabilities in the Finite Element Method. Therefore a smeared out Heaviside function is used instead, e.g.

$$H_{sm}(\phi) = \begin{cases} 0 & \phi < \epsilon \\ \frac{1}{2} + \frac{\phi}{2\epsilon} + \frac{1}{2\pi} \sin\left(\frac{\pi\phi}{\epsilon}\right) & -\epsilon \leq \phi \leq \epsilon \\ 1 & \phi > \epsilon \end{cases} \quad (2.13)$$

where  $\epsilon$  corresponds to half the thickness of the interface. The interface thickness shall depend on the grid size in the mesh, such that it is sufficiently resolved. One can now define a new level set function

$$\tilde{\phi}(r) = H_{sm}(\phi(r)) \quad (2.14)$$

The level set function in Eq. (2.14) has the advantage that it is straightforward to represent the density and viscosity in the two different phases. One simply defines scalar fields that use the level set function to distinguish between the phases.

In addition to the flow field variables, the level set variable  $\phi$  is also solved by the model. An additional step is required to initialize  $\phi$  to ensure smooth initial distribution of the level set variable before the time-dependent computation is started.

The level set variable should have a smooth transition across a finite thickness from one limit to another. For this purpose, an additional study step called “*Transient Initialization*” predefined in COMSOL is required, during which a steady state solution for the combined level set advection-reinitialization equation (2.8) is obtained with no advection, i.e. for the following equation:

$$\frac{\partial \phi}{\partial t} = \gamma \nabla \cdot \left( \epsilon \nabla \phi - \phi(1 - \phi) \frac{\nabla \phi}{|\nabla \phi|} \right) \quad (2.15)$$

#### 2.1.4 Modeling of the surface tension force

In order to model the surface tension, we need two important geometrical parameters, namely, the local interface normal  $\mathbf{n}$  and the curvature  $\kappa$ . The unit normal to the interface is given by

$$\mathbf{n} = \frac{\nabla \phi}{|\nabla \phi|} \Big|_{\phi=0.5} \quad (2.16)$$

The curvature is defined as

$$\kappa = -\nabla \cdot \mathbf{n} \Big|_{\phi=0.5} \quad (2.17)$$

The surface tension force can be computed as the divergence of the capillary pressure tensor  $\mathbf{T}$

$$\begin{aligned} \mathbf{F}_{st} &= \nabla \cdot \mathbf{T} \\ \mathbf{T} &= \nabla \cdot (\sigma(\mathbf{I} - \mathbf{nn}^T)\delta) \end{aligned} \quad (2.18)$$

where  $\mathbf{n}$  is the interface normal,  $\delta$  is a smoothed dirac delta function centered at the 0.5 contour of  $\phi$  and  $\sigma$  is the surface tension coefficient.

$$\delta = 6|\nabla\phi||\phi(1-\phi)| \quad (2.19)$$

It is vital to keep the interface as thin as possible, and its thickness constant for a better approximation. On the other hand, the interface must be wide enough to avoid sharp transitions.

The “*Two-phase Flow Level Set Interface*” algorithm in COMSOL solves the level set advection-reinitialization equation simultaneously with the governing equations of flow. This allows time-dependant computation of laminar flow involving two phases which are immiscible, with a clear definition of both phases and the interface between them.

## 2.2 Electrostatic force calculation

The electric stress can be calculated by taking the divergence of the Maxwell stress tensor  $\mathbf{T}_M$  which couples electrostatic and hydrodynamic phenomena, while assuming that the fluid is incompressible. Neglecting the effect of magnetic field, the Maxwell stress tensor can be defined as follows:

$$\mathbf{T}_{Mij} = \varepsilon_r \varepsilon_0 E_i E_j - \frac{1}{2} (\varepsilon_r \varepsilon_0 E^2) \delta_{ij} \quad (2.20)$$

The final results in terms of the force per unit volume is given as

$$\mathbf{F}_{es} = \nabla \cdot \mathbf{T}_M = -\frac{1}{2} \mathbf{E} \cdot \mathbf{E} \nabla \varepsilon + q^v \mathbf{E} + \nabla \left( \frac{1}{2} \mathbf{E} \cdot \mathbf{E} \frac{\partial \varepsilon}{\partial \rho} \right) \quad (2.21)$$

where  $\mathbf{E}$  is electric field strength,  $\varepsilon$  is the permittivity of fluid and  $q^v$  is the volume charge density near the interface. The first term on the right-hand side of Eq. (2.21) is due to the polarization stress and it acts along the normal direction of the interface. The second term is due to the interaction of the electric charges with the electric field, acting

along the direction of the electric field. The last term results from the changes in material density, usually called the electrostriction force density. This term is neglected in this study as the fluid is assumed to be incompressible. As the electric charges are located on the interface, both the polarization electric stress and the charge field interaction electric stress would thus be exerted on the interface. In order to calculate the electric force, the electric field strength  $\mathbf{E}$  and volume charge density  $q^v$  in Eq. (2.21) are estimated using the various electric field models discussed in the following section.

In electrohydrodynamics, the dynamic currents are small, and hence the magnetic induction effects can be ignored. Therefore, the electric field intensity is irrotational ( $\nabla \times \mathbf{E} = 0$ ).

The Gauss law in a dielectric material with permittivity  $\varepsilon$  can be written in terms of the electric displacement

$$\begin{aligned} \mathbf{D} &= \varepsilon_0 \varepsilon_r \mathbf{E} \\ \nabla \cdot \mathbf{D} &= \nabla \cdot (\varepsilon_0 \varepsilon_r \mathbf{E}) = q^v \end{aligned} \quad (2.22)$$

and the charge conservation can be expressed as follows,

$$\frac{Dq^v}{Dt} = \frac{\partial q^v}{\partial t} + \mathbf{U} \cdot \nabla q^v = -\nabla \cdot (\sigma \mathbf{E}) \quad (2.23)$$

where  $\frac{D}{Dt}$  is the material derivative,  $\sigma$  denotes the electrical conductivity, and  $\mathbf{U}$  represents the velocity of the fluid.  $\varepsilon_0$  is the permittivity of vacuum, and  $\varepsilon_r$  is the relative permittivity (ratio of the permittivity of a substance to that of vacuum).

Charge relaxation time can be defined by  $t_E = \varepsilon / \sigma$ . The viscous time scale of the fluid motion is given by  $t_v = \rho L^2 / \mu$ , where  $\rho$  and  $\mu$  are the density and viscosity of the fluid, and  $L$  is the characteristic length scale.

If the fluid is electrically conductive and satisfies the relation  $t_E \ll t_v$ , the charge may accumulate at the interface almost instantaneously as compared to the time scale of fluid motion. On the other hand, for the weakly conducting fluid, it may behave as a perfect dielectric material when  $t_E \gg t_v$ . There is no free electric charge in the perfect dielectric fluid system.

### 2.2.1 Leaky dielectric model

When both liquids in a two-fluid system are electrically conductive and satisfy the condition  $t_E \ll t_v$ , the charge conservation in the bulk of an inhomogeneous continuous medium can reach steady state much faster than the time scale of the fluid motion. The charge conservation equation (Eq. (2.23)) can be simplified with an quasi-static assumption, and expressed by the divergence of the current density due to the electrical conduction

$$\nabla \cdot (\sigma \mathbf{E}) = 0 \quad (2.24)$$

In the absence of any time-varying magnetic field, the curl of the electric field is zero ( $\nabla \times \mathbf{E} = 0$ ). The electric field can be re-expressed in terms of electric potential ( $V$ ) by

$$\mathbf{E} = -\nabla V \quad (2.25)$$

This would then mean that the charge conservation equation in the liquid can be written as

$$\nabla \cdot (\sigma \nabla V) = 0 \quad (2.26)$$

In a two-fluid system, the electrical conductivity is constant within each fluid, and Eq. (2.26) for electric potential ( $V$ ) can be reduced to Laplace equation ( $\nabla^2 V = 0$ ) in each medium.

At the interface between the two fluid media, the electric potential and electric current are continuous

$$\|V\| = 0 \text{ and } \|\sigma \nabla V \cdot \mathbf{n}\| = 0 \quad (2.27)$$

where  $\| \ \|$  represents a jump across the interface. The above boundary conditions at the interface between two fluids can be embedded in the governing equation Eq. (2.26) for electric potential with variable electric conductivity  $\sigma$  in the different fluid regions of the system.

Based on Eq. (2.23), we can obtain the distribution of volume charge density,

$$q^v = \nabla \cdot (\varepsilon \mathbf{E}) \quad (2.28)$$

With the calculated distributions of electric charge density and electric field strength, the electric stress within the bulk of incompressible fluid in the vicinity of interface can then be determined from

$$\mathbf{F}_{es} = \nabla \cdot \mathbf{T}_M = -\frac{1}{2} \mathbf{E} \cdot \nabla \epsilon + q^v \mathbf{E} \quad (2.29)$$

### 2.2.2 Perfect dielectric model

When both liquids in a two-fluid system have low electrical conductivities and satisfy the condition  $t_E \gg t_v$ , they can be considered as dielectric materials. An externally applied electric field polarizes the molecules of the dielectric material. The formed molecular dipoles will also modify the electric field, which again change the polarization field. The results of this infinite regress can be obtained directly by solving for the electric displacement from the free-charge configuration using Eq. (2.22). As a perfect dielectric medium has inhomogeneous isotropic polarizability and no free charge is present in the medium ( $q^v = 0$ ), the governing equation for the electric field can be written as

$$\nabla \cdot (\epsilon \mathbf{E}) = 0 \quad (2.30)$$

In the absence of any time-varying magnetic field, the curl of the electric field is zero ( $\nabla \times \mathbf{E} = 0$ ). The electric field can be expressed as the gradient of electric potential,  $\mathbf{E} = -\nabla V$ . Hence, equation (2.30) can be re-written in terms of electric potential  $V$  as

$$\nabla \cdot (\epsilon \nabla V) = 0 \quad (2.31)$$

Since there is no free charge at the interface between the two fluids with different permittivities, the normal component of electric displacement and the electric potential are continuous across the interface,

$$\|V\| = 0 \text{ and } \|\epsilon \nabla V \cdot \mathbf{n}\| = 0 \quad (2.32)$$

The electric stress on the interface between two dielectric fluids can be determined from Eq. (2-21) as

$$\mathbf{F}_{es} = -\frac{1}{2}\mathbf{E} \cdot \mathbf{E} \nabla \varepsilon \quad (2.33)$$

The direction of the electric force for a perfect dielectric drop is in the normal direction of the interface, since this direction is determined by the gradient of the electrical permittivity  $\nabla \varepsilon$ , pointing from the medium with a higher permittivity to the one with a lower permittivity. Furthermore, the electric stress acts only on the interface since the electrical permittivity gradient exists only across the interface.

Since the conductivity and relative permittivity are constant, but different, for each fluid, the volume fraction changes from zero in one fluid to one in the other. In order to represent all the physical properties at the interface, the two phase relative permittivity ( $\varepsilon_r$ ) and conductivity ( $\sigma_r$ ) can be defined based on the volume fraction of the phases:

$$\begin{aligned} \varepsilon_r &= \varepsilon_{in} Vf_{in} + \varepsilon_{ex} Vf_{ex} \\ \sigma_r &= \sigma_{in} Vf_{in} + \sigma_{ex} Vf_{ex} \end{aligned} \quad (2.34)$$

$Vf_{in}$  and  $Vf_{ex}$  are the volume fractions of the droplet and the continuous phase, respectively. Using Eq. (2.34), the physical properties change smoothly from the value on one side to the value on the other side. The solution of the Navier-Stokes equations with an interface is not an easy task. This is complicated further when electrostatic effects are coupled to the fluid dynamics. Commercial codes have to be extended and adapted for multidisciplinary subjects such as EHD problems. The governing equations for two-phase flow and electric field have been solved with the software COMSOL using the Finite Element Method (FEM).

## 2.3 Finite Element Method

In the FEM, an indirect approach of seeking a solution satisfying some conditions which simultaneously satisfy the original problem is taken. The solution obtained in this way is known as the “weak” solution (but despite its name it is by no means less correct).



The basic concept of FEM is the subdivision of the computational domain into elements of arbitrary shape and size. The calculation domain composed of the continuous phase  $\Omega_1(t)$  and the drop phase  $\Omega_2(t)$  is discretized using proper elements. The shapes of  $\Omega_1(t)$  and  $\Omega_2(t)$  change with time, following the deformation of the interface.

FEM is a technique for obtaining a numerical approximation to some unknown function  $u(x)$ . The exact function is approximated by forming the expansion:

$$u(x) \approx \tilde{u}(x) = \sum_{j=1}^n u_j b_j(x) \quad (2.35)$$

where  $b_j(x)$  are known basis functions (*e.g.* sinusoidals or polynomials) and  $u_j$  are scalar coefficients. Polynomials are popular because they are simple functions to manipulate mathematically. The task of trying to find the exact function  $u(x)$  in an infinite dimensional search space is then reduced to calculating  $n$  discrete values that produce the best approximation of the solution.

The accuracy of the approximation depends on the form of the chosen basis functions  $b_j(x)$ , and the number of terms used in the expansion. In general, as

$$n \rightarrow \infty, \tilde{u}(x) \rightarrow u(x) \quad (2.36)$$

In general, there are two ways to derive integral formulations for continuum problems: the Variational principle and the Method of Weighted Residual (MWR). A variational principle means that the physical problem can be expressed by the extremum of a functional. Although many physical problems can be described by variational equations (*e.g.* potential flow), there is no guarantee to find a corresponding variational principle for all problems (*e.g.* for flow governed by the Navier-Stokes equations). On the other hand, construction of an equivalent integral formulation, *i.e.* a weak formulation of the governing differential equations, based on MWR is always possible.

In some cases the natural boundary condition is adequate and no action is required. Natural boundary conditions are those that automatically will be satisfied after solution of

the problem. If the natural boundary condition is not adequate, it is often possible to modify the functional (variational form) to change this.

Finite Element bases are constructed implicitly in an element by element manner in terms of shape functions. Higher order shape functions provide a more rapid convergence of the solution, but introduce other difficulties: First of all, the programming of the finite element implementation is more complex, especially when mesh adaptation is used. Secondly, the resulting matrix bandwidth is increased due to the higher number of interconnected nodes, making the matrix solution process slower. Thirdly, the matrix assembly time is greatly increased due to the larger number of Gaussian quadrature points needed for the exact evaluation of the integrals.

The only restriction for the subdivision of the computational domain into elements is that the elements may not overlap and that they have to cover the complete computational domain. Which type of element is most appropriate for a particular problem depends on several factors, such as domain geometry, required accuracy, computational costs, etc. The mesh and solver steps are usually carried out automatically using default settings, which are tuned for each specific fluid flow interface.

The mesh generator discretizes the domains into triangular or quadrilateral mesh elements in 2D geometries. If the boundary is curved, these elements represent only an approximation of the original geometry. In 3D geometries, the domain can be discretized into tetrahedral, hexahedral (brick), prism, or pyramid mesh elements in 3D geometries as shown in Figure 2.3. These four elements can be used, in various combinations, to mesh any 3D model. Tetrahedral and triangular elements are in general better suited than quadrilaterals for the meshing of complex geometries.

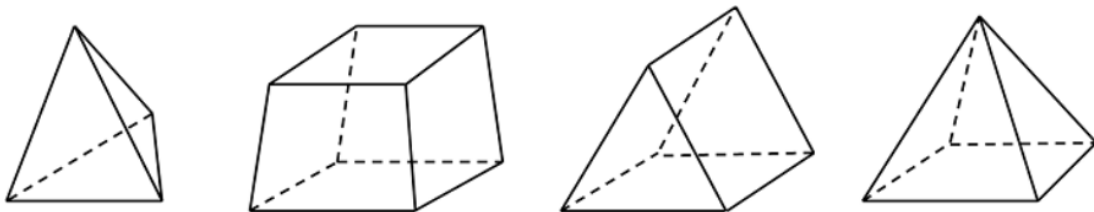


Figure 2.3 Different 3D element types

Tetrahedral elements are the default element type for most problems within COMSOL. These elements are also known as a *simplex*, which simply means that any 3D volume, regardless of shape or topology, can be meshed with these elements. The primary motivation for using brick and prism elements is that they can significantly reduce the number of elements in the mesh. These elements can have very high aspect ratios (the ratio of longest to shortest edge) whereas the algorithm used to create a tetrahedral mesh will try to keep the aspect ratio close to unity. It is reasonable to use high aspect ratio brick and prism elements when the solution varies gradually in certain directions, or if accurate results in those regions are not of the highest importance.

Note that there is no direct relationship between the number of degrees of freedom and memory used to solve the problem. This is because the different element types have different computational requirements. A second-order tetrahedral has 10 nodes per element, while a second-order brick has 27 nodes. This means that the individual element matrices are larger, and the corresponding system matrices will be denser, when using a brick mesh. The memory (and time) needed to compute a solution depends upon the number of degrees of freedom solved for, as well as the average connectivity of the nodes, and other factors.

The incompressible fluid flow module in COMSOL is somewhat more general than this and is able to account for arbitrary variations in viscosity and small variations in density. This section provides a summary of the participating equations and boundary condition approximations. Different boundary conditions are defined in Table 2.1.

Table 2.1 Summary of the boundary conditions

Boundary Type	Equations
Inlet-Pressure, No Viscous Stress	$P = \text{Pressure}$ $\mu(\nabla\mathbf{u} + (\nabla\mathbf{u})^T)\mathbf{n} = 0$
Wall-No Slip	$\mathbf{u} = 0$
Wall- Wetted	$\mathbf{n} \cdot \mathbf{u} = 0$ $\mathbf{F}_{fr} = -\frac{\mu}{\beta}\mathbf{u}$
Outlet- Pressure, No Viscous Stress	$P = 0$ $\mu(\nabla\mathbf{u} + (\nabla\mathbf{u})^T)\mathbf{n} = 0$
Initial Interface	$\phi_0 = 0.5$

A wetted wall is utilized at locations where the fluid interface is expected to move along the wall. Two parameters define this condition: slip length, which is coupled to mesh size, and contact angle  $\theta$ .

A pressure-based outlet boundary condition is used at two sides of the continuous phase domain to prevent boundary layer effects on the droplet motion. The Level-Set method requires specification of the initial distribution of the two fluids in the domain along with the initial location of the interface separating them.

COMSOL is employed to perform the numerical simulations. Second order quadratic basic functions are used for the level set variable to provide smoother solutions than piece-wised linear basic functions.

For convenience, prebuilt physics interfaces in the modules of AC/DC and computational fluid dynamics by COMSOL are used. More specifically, the leaky dielectric model consists of the “*Electric Current*” and “*Two Phase Laminar Flow, Level Set*” interfaces, and the perfect dielectric model consists of the “*Electrostatic*” and “*Two-Phase Laminar Flow, Level Set*” interfaces, respectively. The coupling terms between electric governing equation, Navier–Stokes equations and level set equation need to be implemented.

## References

- [1] S. Ruben and Z. Stéphane, “Direct numerical simulation of free-surface and interfacial flow”, *Annu. Rev. Fluid Mech.*, vol. 31, no. 1, pp. 567-603, 1999.
- [2] D. Jamet, D. Torres and J. Brackbill, “On the theory and computation of surface tension: The elimination of parasitic currents through energy conservation in the second-gradient method”, *Journal of Computational Physics*, vol. 182, no. 1, pp. 262-276, 2002.
- [3] S. O. Unverdi and G. A. Tryggvason, “Front-tracking method for viscous, incompressible, multi fluid flows”, *J. Comput. Phys.*, vol. 100, pp. 25-37, 1992.
- [4] J. Hua and J. Lou, “Numerical simulation of bubble rising in viscous liquid”, *J. Comput. Phys.*, vol. 222, no. 2, pp. 769-795, 2007.
- [5] J. Hua, B. Zhang and J. Lou, “Numerical simulation of microdroplet formation in coflowing immiscible liquids”, *AIChE J.*, vol. 53, no. 10, pp. 2534-2548, 2007.
- [6] L. Y. Yeo, O. K. Matar, E. S. P. de Ortiz and G. E. Hewitt, “Film drainage between two surfactant-coated drops colliding at constant approach velocity”, *J. Colloid Interface Sci.*, vol. 257, no. 1, pp. 93-107, 2003.
- [7] C. Pozrikidis, “Expansion of a two-dimensional foam”, *Eng. Anal. Boundary Elem.*, vol. 26, no. 6, pp. 495-504, 2002.
- [8] P. K. Notz, A. U. Chen and O. A. Basaran, “Satellite drops: Unexpected dynamics and change of scaling during pinch-off”, *Phys. Fluids*, vol. 13, no. 3, pp. 549-552, 2001.
- [9] C. Zhou, P. Yue and J. J. Feng, “Formation of simple and compound drops in microfluidic devices”, *Phys. Fluids*, vol. 18, no. 9, pp. 092105-14, 2006.
- [10] M. W. Weber and R. Shandas, “Computational fluid dynamics analysis of microbubble formation in microfluidic flow-focusing devices”, *Microfluid. Nanofluid.*, vol. 3, no. 2, pp. 195-206, 2007.
- [11] M. R. Davidson, D. J. E. Harvie and J. J. Cooper-White, “Flow focusing in microchannels”, *ANZIAM J.*, 46(E), pp. C47-C58, 2005.
- [12] A. J. Abrahamse, A. van der Padt, R. M. Boom and W. B.C. de Heij, “Process fundamentals of membrane emulsification: Simulation with CFD”, *AIChE J.*, vol. 47, pp. 1285-1291, 2001.

- [13] M. Ohta, M. Yamamoto and M. Suzuki, "Numerical-analysis of a single drop formation process under pressure pulse condition", *Chem. Eng. Sci.*, vol. 50, no. 18, pp. 2923-2931, 1995.
- [14] M. De Menech, "Modeling of droplet breakup in a microfluidic T-shaped junction with a phase-field model", *Phys. Rev. E*, vol. 73, 031505, 2006.
- [15] O. Kuksenok, D. Jasnow, J. Yeomans and A. C. Balazs, "Periodic droplet formation in chemically patterned microchannels", *Phys. Rev.Lett.*, vol. 91, 108303, 2003.
- [16] M. M. Dupin, I. Halliday and C. M. Care, "Simulation of a microfluidic flow-focusing device", *Phys. Rev. E*, vol. 73, 055701(R), 2006.
- [17] S. Van der Graaf, T. Nisisako, C. G. P. H Schroen, R. G. M. van der Sman and R. M. Boom, "Lattice Boltzmann simulations of droplet formation in a T-shaped microchannel", *Langmuir*, vol. 22, no. 9, pp. 4144-4152, 2006.
- [18] Z. Yu, O. Heraminger and L. S. Fan, "Experiment and lattice Boltzmann simulation of two-phase gas-liquid flows in microchannels", *Chem. Eng. Sci.*, vol. 62, no. 24, pp. 7172-7183, 2007.
- [19] S. Osher, J. A. Sethian, "Fronts propagating with curvature-dependent speed: Algorithms based on Hamilton-Jacobi formulations", *J. Comput. Phys.*, vol. 79, no. 1, pp. 12-49, 1988.
- [20] M. Sussman, P. Smereka and S. A Osher, "level set approach for computing solutions to incompressible two-phase flow", *J. Comput. Phys.*, vol. 114, pp. 146-159, 1994.
- [21] Y. C. Chang, T. Y. Hou, B. Merriman and S. Osher, "A level set formulation of Eulerian interface capturing methods for incompressible fluid flows", *J. Comput. Phys.*, vol. 124, pp. 449-464, 1996.
- [22] R. P. Fedkiw, T. Aslam, B. Merriman and S. Osher, "A non-oscillatory Eulerian approach to interfaces in multimaterial flows (the ghost fluid method)", *J. Comput. Phys.*, vol. 152, no. 2, pp. 457-492, 1999.
- [23] M. Kang, R. P. Fedkiw and X. D. Liu, "A boundary condition capturing method for multiphase incompressible flow", *J. Sci. Comput.*, vol. 15, no. 3, pp. 323-360, 2000.

- [24] M. Sussman and E. G. Puckett, "A coupled level set and volume-of-fluid method for computing 3D and axisymmetric incompressible two-phase flows", *J. Comput. Phys.*, vol. 162, no. 2, pp. 301-337, 2000.
- [25] M. Tatineni and X. L. Zhong, "Numerical simulation of unsteady low-Reynolds-number separated flows over airfoils", *AIAA J.*, vol. 38, no. 7, pp. 1295-1298, 2000.
- [26] T. Cubaud, M. Tatineni, X. L. Zhong and C. M. Ho, "Bubble dispenser in microfluidic devices", *Phys. Rev. E*, vol. 72, 037302, 2005.
- [27] G. I. Taylor, "Studies in electrohydrodynamics. I. Circulation produced in a drop by an electric field," *Proc. R. Soc. London, Ser. A* vol. 291, no. 1425, pp. 159-166, 1966.
- [28] W. Shyy, M. Francois, H. Udaykumar, N. N'dri and R. Tran-Son-Tay, "Moving boundaries in micro-scale biofluid dynamics," *Applied Mechanics Reviews*, vol. 54, no. 5, pp. 405-454, 2001.
- [29] C. Hirt and B. Nichols, "Volume of fluid (VOF) method for the dynamics of free boundaries," *Journal of Computational Physics*, vol. 39, no. 1, pp. 201-225, 1981.
- [30] J. A. Sethian and S. Peter, "Level set methods for fluid interfaces," *Annu. Rev. Fluid Mech*, vol. 35, no. 1, pp. 341-372, 2003.
- [31] S. R. Hysing and S. Turek, "The eikonal equation: Numerical efficiency vs. Algorithmic complexity on quadrilateral grids," *Algoritmy*, pp. 22-31, 2005.
- [32] J. A. Sethian, "Level Set Methods and Fast Marching Methods: Evolving Interfaces in Computational Geometry, Fluid Mechanics, Computer Vision, and Materials Science", Cambridge University Press, 1999.
- [33] E. Olsson and G. Kreiss, "A conservative level set method for two phase flow", *J. Comput. Phys.*, vol. 210, no. 1, pp. 225-246, 2005.
- [34] E. Olsson, G. Kreiss and S. Zahedi, "A conservative level set method for two phase flow II", *J. Comput. Phys.*, vol. 225, no. 1, pp. 785-807, 2007.
- [35] M. Sussman and E. G. Puckett, "A coupled level set and volume-of-fluid method for computing 3D and axisymmetric incompressible two-phase flows", *J. Comput. Phys.*, vol. 162, no. 2, pp. 301-337, 2000.
- [36] M. Sussman, K. M. Smith, M. Y. Hussaini, M. Ohta and R. Zhi-Wei, "A sharp interface method for incompressible two-phase flows", *J. Comput. Phys.*, vol. 221, no. 2, pp. 469-505, 2007.

- [37] M. Sussman, “A second order coupled level set and volume-of- fluid method for computing growth and collapse of vapor bubbles”, *J.Comput. Phys.*, vol. 187, no. 1, pp. 110-136, 2003.
- [38] S. P. Van Der Pijl, A. Segal, C. Vuik and P. VuikWesseling, “A mass-conserving level set method for modeling of multi-phase flows”, *Int. J.Numer. Methods Fluids*, vol. 47, no. 4, pp. 339-361, 2005.
- [39] D. L. Sun and W. Q. Tao, “A coupled volume-of-fluid and level set (VOSET) method for computing incompressible two-phase flows”, *Int.J. Heat Mass Transfer*, vol. 53, no. 4, pp. 645-655, 2010.
- [40] T. Wang, H. Li, Y. Feng and D. Shi, “A coupled volume-of-fluid and level set (VOSET) method on dynamically adaptive quadtree grids”, *Int. J. Heat Mass Transfer*, vol. 67, pp. 70-73, 2013.
- [41] S. Shin, I. Yoon and D. Juric, “The local front reconstruction method for direct simulation of two and three dimensional multiphase flows”, *J. Comput. Phys.*, vol. 230, no. 17, pp. 6605-6646, 2011.
- [42] S. Basting and M. Weismann, “A hybrid level set–front tracking finite element approach for fluid structure interaction and two-phase flow applications”, *J. Comput. Phys.*, vol. 255, pp. 228-244, 2013.
- [43] D. Enright, R. Fedkiw, J. Ferziger and I. Mitchell, “A hybrid particle level set method for improved interface capturing”, *J. Comput. Phys.*, vol. 183, no. 1, pp. 83-116, 2002.



## Chapter 3

### 3 « Numerical simulation of electrically deformed droplets less conductive than the ambient fluid »

#### 3.1 Introduction

Drop deformation under the influence of an electric field has attracted a lot of attention in the recent past due to its applications in several electrohydrodynamics based processes, such as electro-spraying, electro-emulsification, electro-coalescence and others. If the fluids are perfect dielectrics, the electric stress discontinuity just has a normal component that can be balanced by the interfacial tension at steady state and the droplet always deforms into the prolate shape. Assuming slightly conducting materials creates a tangential electric stress at the interface due to the mobile charges; the effect of electric field on these surface charges will drag the fluid into motion. The direction of the flow depends on the charge distribution on the surface and under certain conditions the droplet can deform into the oblate shape. Taylor [1] proposed a small deformation theory, based on the leaky dielectric model, to theoretically analyze the deformation of the droplets in weak electric fields. In order to characterize the droplet deformation, the degree of deformation is conventionally defined by:

$$D = \frac{l_1 - l_2}{l_1 + l_2} \quad (3.1)$$

where  $l_1$  and  $l_2$  are the axes of the droplet in the direction parallel and perpendicular to the electric field, respectively. A positive  $D$  represents a deformation of the droplet that has an increased length along the direction of the electric field (prolate), while a negative  $D$  represents a deformation of the droplet, which deforms perpendicularly to the direction of the electric field (oblate). Taylor's analysis predicted a relationship between droplet deformation  $D$  and electric field strength as

$$D = \frac{9a\varepsilon_{ex}E^2}{16\gamma S(2+R)^2} \times \left[ S(R^2 + 1) + 3(RS - 1) \frac{2\lambda + 3}{2\lambda + 5} - 2 \right] \quad (3.2)$$

where  $a$  is the radius of the undeformed droplet and  $\gamma$  is the surface tension. The subscripts “in” and “ex” denote the values of parameters for the droplet and the ambient fluid, respectively. The ratios of physical properties are defined as:

$$R = \frac{\sigma_{in}}{\sigma_{ex}}, \quad S = \frac{\varepsilon_{ex}}{\varepsilon_{in}}, \quad \lambda = \frac{\mu_{in}}{\mu_{ex}}, \quad (3.3)$$

where  $\sigma$  is electrical conductivity,  $\varepsilon$  is permittivity, and  $\mu$  is viscosity.

According to Taylor’s model, the conduction response of the fluids can be characterized by the product of the  $R$  and  $S$

$$RS = \frac{t_{c,ex}}{t_{c,in}}, \quad \text{where } t_{c,in} = \frac{\varepsilon_{in}}{\sigma_{in}} \text{ and } t_{c,ex} = \frac{\varepsilon_{ex}}{\sigma_{ex}}$$

If  $RS > 1$ , the interface charge distribution is dominated by the droplet and the fluid motion is from the equator to the pole, while if  $RS < 1$ , the charge distribution is dominated by the exterior fluid and the fluid motion is from the poles to the equator [2, 3]. Various breakup modes and steady state shapes were investigated using numerical simulations. In most cases, the numerical simulations of droplet deformation have been limited to axisymmetric cases [4-7]. Lac and Homsy [3] considered a naturally buoyant and uncharged droplet suspended in another liquid subjected to a uniform electric field assuming creeping flow conditions and axial symmetry of the problem. They presented a review for various modes of droplet deformation, assuming a wide range of conductivity and permittivity ratios. Various breakup modes and steady state shapes were investigated. A comparison of the drop deformations from the simulation and the theoretical predictions was also proposed by Hua et al. [6] considering three different electric field models: a leaky dielectric model for droplets with finite electrical conductivity, a perfect dielectric model for electrically insulating droplets and a simplified constant surface charge model for charged droplets.

In the studies mentioned above, the oblate deformation simulations should be valid only for small electric capillary numbers to avoid the electrorotation and symmetry breaking of the problem. The Taylor model does not fully capture all phenomena that have been observed in experiments. The deformation and bursting of liquid droplets suspended in liquid dielectrics and exposed to an electric field were measured experimentally by several authors [8-11]. The bursting mode was found to show considerable variation with the electrical properties of the systems [8]. They also found that when the permittivity of the droplet is smaller than that of the ambient fluid, the droplets were flattened into a sheet, which then turned over until it was no longer parallel to the electrodes. Vizika and Saville [10] experimentally investigated the deformation of droplets in AC and DC fields. They observed that silicone oil droplets in castor oil change their shape from oblate to prolate under sufficient DC electric field, but they did not explain this behaviour. Ha and Yang [12] did a comprehensive study for droplets more conductive than the ambient fluid, experimentally investigating the deformation and breakup of Newtonian and non-Newtonian droplets. Three different cases of highly conducting droplets, conducting droplets and slightly conducting droplets were examined. They found that the electrohydrostatic theory is satisfactory when the ratio of resistivities for the droplet and continuous-phase is less than  $10^{-5}$ .

Recent experimental studies have discovered non-axisymmetric shapes for the droplets [13-16]. It was found that the symmetry breaking happens only for droplets with  $RS < 1$  due to the reverse dipole created inside the droplet. The rotational flow is created and the major axis of the droplet makes an oblique angle with respect to the electric field. The effect of AC and DC fields on continuous electrorotation of droplets with the rotation of the symmetric axis of each droplet was investigated by Krause and Chandratreya [13]. It was found that the rotation velocities in the DC field were in agreement with a theoretical treatment for electrorotation of solid spheres in DC fields (See the Introduction of Ref. 17). Ha and Yang [14] experimentally investigated the electrorotation of a less conducting droplet suspended in a more conducting liquid and its effect on deformation and burst behaviour of the droplet. It was stated that in the case of highly viscous droplets, the deviation from the rigid body theory is small. They also found the threshold electric field strength beyond which the droplet breaks up. The deformation and break up

of a droplet in a steady and uniform electric field was investigated experimentally by Sato et al. [15]. Three different modes were reported for silicone oil suspended in more conducting castor oil. A peculiar oscillatory motion of the droplets accompanied by cyclic oblate-to-prolate and prolate-to-oblate variations in shape was found. Salipante and Vlahovska [16] presented a systematic experimental study of the non-axisymmetric rotational flow in strong electric fields. The critical electric field, droplet inclination angle and the rate of rotation were measured for small and high viscosity droplets. It was found that the droplet inclination angle increases with an increase in field.

It is difficult to measure the conductivities of the oily fluids used in these experiments with conventional methods due to their extremely low conductivities. It can be concluded that some of the discrepancies noted between experiments can result from inaccurate measurement of conductivities. On the other hand, it is clear that the rotation of the droplet with an oblique axis to the applied electric field will destroy the problem symmetry. In order to have a comprehensive understanding of the problem, a full 3D simulation is needed.

In the present study, we numerically investigate the deformation, oscillation and breakup of a weakly conducting droplet suspended in an ambient medium with a higher conductivity. It is the first time that the deformation of such droplet is investigated numerically in a 3D configuration. There has been also relatively little work on the breakup of a less conducting droplet via the oblate-type deformation.

## 3.2 Problem statement

Figure 3.1 illustrates the 3D model considered in this study. A small liquid droplet is suspended in another immiscible fluid and is exposed to a uniform electric field parallel to the Y-axis. This field is generated by applying different electric potentials to the parallel plates in the X-Z planes.

The center of the droplet is placed in the middle of the rectangular cube. The liquids are assumed to be incompressible Newtonian with the same density,  $\rho$ , so that the drop is under neutrally buoyant condition. The interface separating the two fluids is assumed to have a constant interfacial tension coefficient. The size of the computational domain is 10

times the droplet radius in the direction of the electric field and 8 times the droplet radius in the directions normal to the electric field. At the initial stage, the shape of the droplet is assumed to be spherical, the center of droplet is located at the centre of the parallel-plate capacitor and both fluids are motionless.

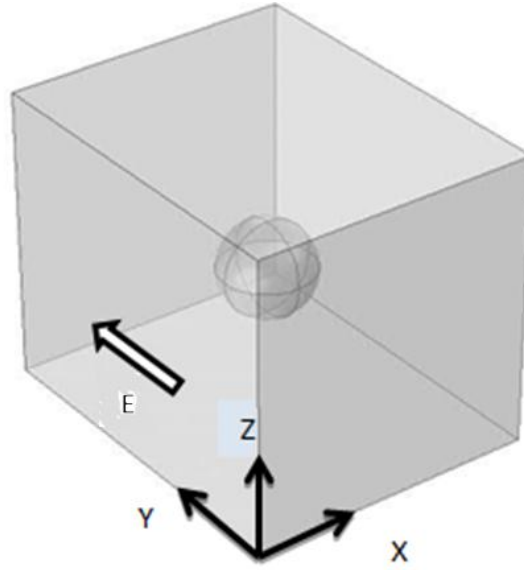


Figure 3.1 Model of a suspended droplet in an electric field

In order to investigate the dynamics of droplet deformation in an electric field it is necessary to solve the Navier-Stokes equations, describing the fluid motion, as well as track the interfaces between both fluids. The laminar two-phase flow system studied here is coupled with the applied electric field and the electric charge conservation law. Additional body forces are added to the Navier-Stokes equations for considering the surface tension ( $\mathbf{F}_{st}$ ) and electric stress ( $\mathbf{F}_{es}$ ).

$$\rho \frac{\partial \mathbf{u}}{\partial t} + \rho(\mathbf{u} \cdot \nabla)\mathbf{u} = \nabla \cdot [-P\mathbf{I} + \mu(\nabla\mathbf{u} + (\nabla\mathbf{u})^T)] + \mathbf{F}_{st} + \mathbf{F}_{es} \quad (3.4)$$

$$\nabla \cdot \mathbf{u} = 0$$

where  $\mathbf{u}$  denotes fluid velocity,  $\mathbf{I}$  is the identity matrix,  $\rho$  is the fluid density,  $\mu$  is the dynamic viscosity and  $P$  is the pressure. In the current simulation, no-slip boundary

conditions are applied for the electrodes and pressure outlet conditions are applied for other boundaries.

To describe the evolution of the droplet shape, the Level-Set method [18], suitable for free boundary problems, is applied. In the Level-Set method, the interface is considered to have a finite thickness of the same order as the mesh size instead of zero thickness. The physical property changes smoothly from the value on one side of the interface to the value on the other side in the interfacial transitional zone. The method describes the evolution of the interface between the two fluids tracing an iso-potential curve of the level set function ( $\phi$ ). In general, in droplet  $\phi = 1$  and in ambient fluid  $\phi = 0$ . The interface is represented by the 0.5 contour of the level set function ( $\phi = 0.5$ ). The movement of the interface is governed by a differential equation for this function. To keep the level set function a distance function, a reinitialization process is needed. Ideally, the interface should not change its position during this reinitialization procedure, but in many applications the zero level set can become distorted by parasitic numerical inaccuracies, if the gradients in the neighborhood of the interface are either very large or very small. For this reason, an improved reinitialization method is used.

Level-Set methods automatically deal with topological changes and it is in general easy to obtain high order of accuracy. The time evolution of the interface is modeled via transport of the level set function  $\phi$  due to the underlying physical velocity field. The function  $\phi$  is governed by the equation

$$\frac{\partial \phi}{\partial t} + \mathbf{u} \cdot \nabla \phi = \alpha \nabla \cdot \left( \epsilon_{ls} \nabla \phi - \phi(1 - \phi) \frac{\nabla \phi}{|\nabla \phi|} \right) \quad (3.5)$$

where  $\epsilon_{ls}$  is the parameter controlling the interface thickness and  $\alpha$  is the reinitialization parameter. A suitable value for  $\alpha$  is the maximum velocity magnitude occurring in the model. The density and viscosity, which are different for oil and water, are automatically calculated from the level set variable  $\phi$ , as well as the surface tension force.

The surface tension force is given by

$$\mathbf{F}_{st} = \nabla \cdot \mathbf{T} \quad (3.6)$$

$$\mathbf{T} = \gamma(\mathbf{I} - (\mathbf{n}\mathbf{n}^T))\delta$$

where  $\mathbf{n}$  is the interface normal and  $\delta$  is the Dirac-delta function that is nonzero only at the fluid interface. The interface normal is calculated from

$$\mathbf{n} = \frac{\nabla\phi}{|\nabla\phi|} \quad (3.7)$$

The use of a Dirac-delta function will ideally create a sharp interface in the mathematical formulation. However, to implement this in the numerical simulation, the Dirac-delta function should be approximated by

$$\delta = 6|\phi(1 - \phi)||\nabla\phi| \quad (3.8)$$

The electric force causes the deformation and it can be calculated from the electric field distribution, which depends on the position and shape of the droplet. In the absence of any time-varying magnetic field, the curl of the electric field is zero ( $\nabla \times \mathbf{E} = 0$ ) and the electric field can be expressed in terms of the electric potential  $V$ .

$$\mathbf{E} = -\nabla V \quad (3.9)$$

The charge conservation in each medium can be expressed as follows

$$\nabla \cdot (\sigma \nabla V) = 0 \quad (3.10)$$

where  $\sigma$  is the electric conductivity of the medium.

Assuming that the electric relaxation time is less than the time scale of the fluid motion, in a two-fluid system the electrical conductivity is constant within each fluid and Eq. (3.10) for electric potential ( $V$ ) can be reduced to Laplace equation in each medium

$$\nabla^2 V = 0 \quad (3.11)$$

It is assumed that there is no space charge in the fluids except the surface charge on the interface, created by the difference between permittivities and conductivities of both

fluids. At the interface between the two fluid media, the electric potential and normal component of electric current density are continuous.

$$\|V\| = 0 \text{ and } \|\sigma \nabla V \cdot \mathbf{n}\| = 0 \quad (3.12)$$

where  $\| \ \|$  represents a jump across the interface. The above boundary conditions at the interface between two fluids can be embedded in the governing equation Eq. (3.10) for electric potential with variable electric conductivity  $\sigma$  in the different fluid regions of the system.

After solving Eq. (3.10), the electric potential can be obtained and then the electric field strength can be calculated using Eq. (3.9). The current density ( $\mathbf{J}$ ) and the electric displacement ( $\mathbf{D}$ ) can also be found from

$$\mathbf{J} = \sigma \mathbf{E} + \frac{\partial \mathbf{D}}{\partial t} \quad (3.13)$$

$$\mathbf{D} = \varepsilon_0 \varepsilon_r \mathbf{E}$$

where  $\varepsilon_0$  is the permittivity of vacuum and  $\varepsilon_r$  is the relative permittivity of medium (ratio of the absolute permittivity and that of vacuum). Assuming that the fluids are incompressible, the electric stress can be calculated by taking the divergence of the Maxwell stress tensor, which couples electrostatic and hydrodynamic phenomena. Neglecting the effect of magnetic field, the Maxwell stress tensor can be defined as follows:

$$\mathbf{T}_{Mij} = \varepsilon_r \varepsilon_0 E_i E_j - \frac{1}{2} (\varepsilon_r \varepsilon_0 E^2) \delta_{ij} \quad (3.14)$$

The momentum equation is modified by inserting the electric force,  $F_{es}$ , which can be determined by calculating the divergence of the Maxwell stress tensor ( $\mathbf{T}_M$ ):

$$\mathbf{F}_{es} = \nabla \cdot \mathbf{T}_M \quad (3.15)$$

The conductivities and relative permittivities for each fluid are constant, but different. The volume fraction changes from zero in one fluid to one in the other one. In order to



have all the physical properties in the interface, the two phase relative permittivity ( $\varepsilon_r$ ) and conductivity ( $\sigma_r$ ) can be defined based on the volume fraction of the phases:

$$\begin{aligned}\varepsilon_r &= \varepsilon_{in}Vf_{in} + \varepsilon_{ex}Vf_{ex} \\ \sigma_r &= \sigma_{in}Vf_{in} + \sigma_{ex}Vf_{ex}\end{aligned}\tag{3.16}$$

where  $Vf_{in}$  and  $Vf_{ex}$  are the volume fractions of the droplet and the continuous phase, respectively. Using Eq. (3.16), the physical properties change smoothly from the value on one side to the value on the other side. The governing equations for two-phase flow and electric field have been solved with the commercial software COMSOL based on the Finite Element Method (FEM) [19].

### 3.3 Simulation validation

In order to validate the numerical algorithm, two different breakup modes of the prolate type deformation are compared with the available experimental data of Ha and Yang [12]. There is a large set of parameters to consider and in the results that follow we assume that the drop phase and the suspending fluid have the same parameters as measured in [12]. Two different systems (denoted NN6 and NN21) were chosen from their experimental system. According to their measurements, the relevant parameters are as follows:

Table 3.1 List of experimental parameters

System	$R = \frac{\sigma_{in}}{\sigma_{ex}}$	$S = \frac{\varepsilon_{ex}}{\varepsilon_{in}}$	$\lambda = \frac{\mu_{in}}{\mu_{ex}}$	$\gamma(\text{N/m})$
NN6	$> 10^5$	0.05	0.043	0.0054
NN21	$\sim 10$	0.73	0.874	0.0033

For a highly conducting droplet (NN6), the droplet first deforms into an elongated ellipsoid. After reaching the critical deformation, the drop begins to stretch rapidly and the blobs at each ends move away leaving two daughter droplets at the ends and a main body in the middle (Figure 3.2).

For a slightly conducting drop (NN21), having the viscosity comparable to the ambient phase, the droplet elongates into the thin thread with sharply pointed ends rather than relaxes into an ellipsoid like the highly conducting drop (Figure 3.3). Although the drop ends become pointed, they did not refer this mode to tip streaming.

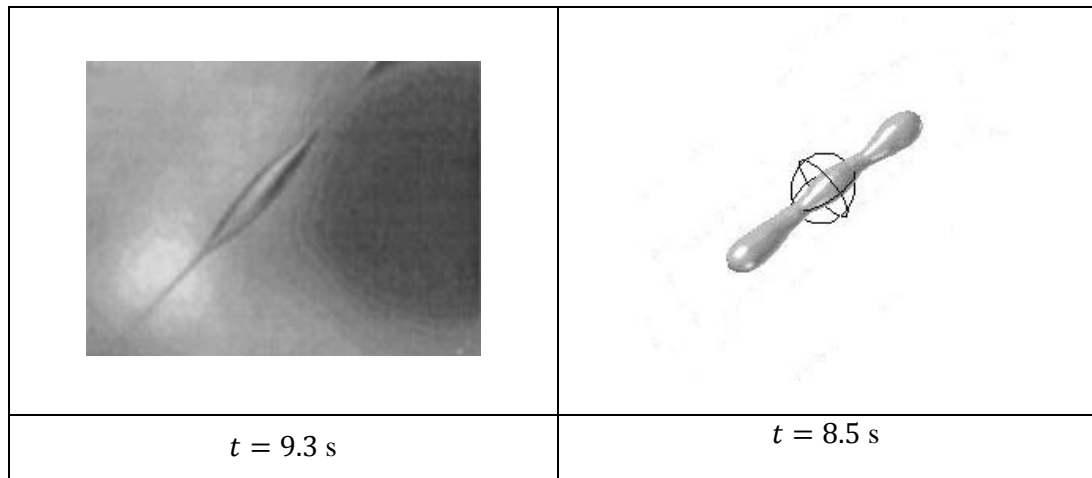


Figure 3.2 Droplet breakup in NN6 configuration [13]: experimental data (left) and numerical results (right). The applied electric field strength is 4.5 kV/cm

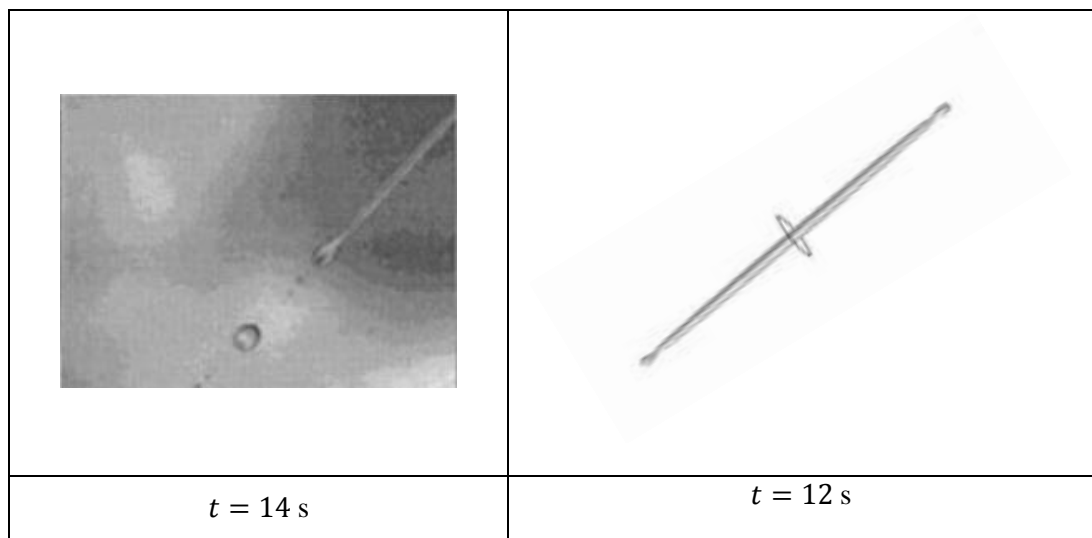


Figure 3.3 Droplet breakup in NN21 configuration [13]: experimental data (left) and numerical results (right). The applied electric field strength is 3.2 kV/cm

In the range of electric capillary numbers covered in the experiments, the measured deformations and break-up match very well the numerical results. For a highly conducting droplet (NN6), according to the details of the experiments, the droplet begins to stretch rapidly on frame 140 (the frame rate is 15 frames/s) which seems to agree perfectly with our numerical results ( $t = 8.5$  s). For the NN21 system, experimental figures illustrate the forming of the pinching necks on frame 210 ( $t = 14$  s) which is also in good agreement with our numerical results ( $t = 12$  s).

To check the sensitivity of the numerical simulations on the size of the computational domain, the electrodes distance has been checked for three different values of 8a, 10a and 12a (where  $a$  is the radius of an undeformed droplet). The drop shapes for the 10a and 12a are almost identical, but differences are evident when compared to the 8a solution. Since time-dependent highly accurate solutions are computationally expensive we employ the 10a distance for all the computations reported in what follows.

### 3.4 Results and discussion

The simulations were done for different conductivity and viscosity ratios. The degree of droplet deformation can be plotted as a function of the electric capillary ( $Ca_E$ ) number for given ratios of the viscosities, permittivities, and conductivities of the droplet and continuous phases. The electric capillary number describes the relative strength of the electric force with respect to the capillary interfacial force.

$$Ca_E = \frac{a\epsilon_{ex}E^2}{\gamma} \quad (3.17)$$

The problem depends on a single dynamic parameter,  $Ca_E$ , and three material property ratios:  $R$ ,  $S$  and  $\lambda$  [4]. Three different modes of the droplet distortion can be distinguished:

- (A) At very low electric fields the droplet deforms into a symmetric oblate shape.
- (B) Increasing electric field causes the oscillatory oblate-prolate motion.

(C) The droplet turns into the torus shape, which leads to a breakup, when the electric field intensity is further increased.

### 3.4.1 Small deformation

In order to verify the accuracy of the numerical model, the deformations of a droplet with  $a = 1.3$  mm at low electric field calculated numerically have been compared with the analytical results of the small deformation theory [1]. In this case the droplet deforms into an oblate shape with the axis of symmetry parallel to the direction of the electric field. Figure 3.4 compares the numerical results for droplet deformation with those obtained from the asymptotic Taylor theory for  $R = 0.15$ ,  $S = 1.38$  and  $\lambda = 1.31$ . The numerical results show good agreement with Taylor's theory up to  $D \approx -0.05$ . This is because Taylor's theoretical analysis is based on the assumption of small droplet deformation. When the droplet deformation is small, the deformation increases almost linearly with the electrical capillary number, which agrees well with the prediction by Taylor's theory. For stronger electric fields ( $Ca_E > 0.27$ ), the droplet starts to oscillate and the numerical results deviate from the Taylor's theory.

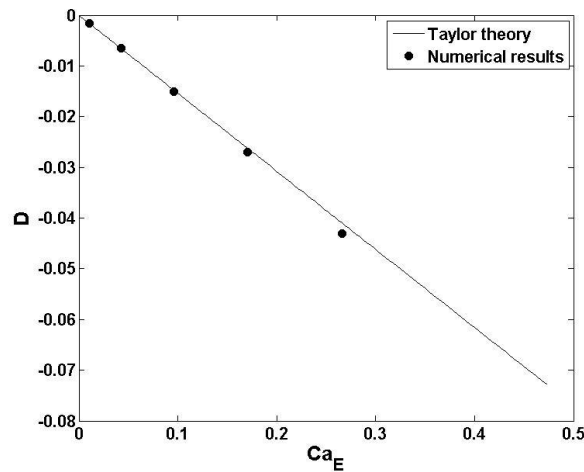


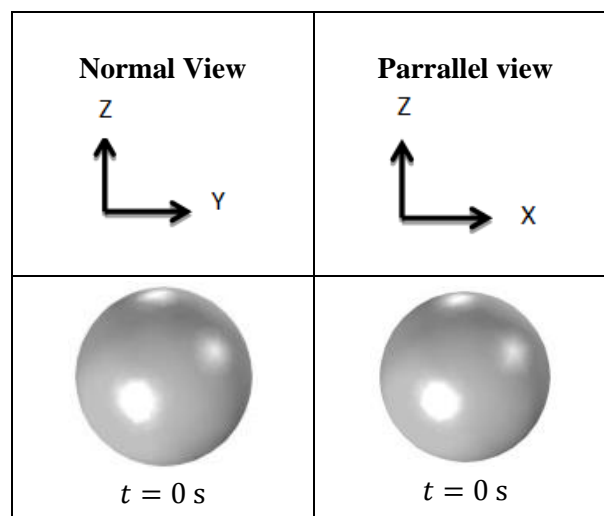
Figure 3.4 Droplet deformation versus electric capillary number for  $R=0.15$ ,  $S=1.38$  and  $\lambda=1.31$

### 3.4.2 Oscillatory oblate-prolate motion

This phenomenon is very interesting from a mechanical point of view, because using a DC electric field with a constant strength causes elongation and contraction of droplets and the droplet experiences highly nonlinear oscillatory motion when the magnitude of the electric field is increased. Figure 3.5 shows the image sequence from two directions, illustrating the oscillatory motion of a droplet for a  $a = 1.3$  mm droplet exposed to the electric field  $E = 4$  kV/cm ( $Ca_E = 1.9$ ). The physical properties of the droplet and the surrounding fluid are:

$$\lambda = 1.31, \quad R = 0.15, \quad S = 1.38.$$

Sufficiently strong electric field causes the droplet to oscillate between the oblate and prolate shapes. The major axis of the droplet makes an oblique angle comparing to the first regime and this angle varies during the oscillation between the oblate and prolate deformation. The droplet shape changes from an oblate shape with tilted symmetric axis into the prolate shape with horizontal axis and then from prolate shape to oblate shape. While the field is constant in this regime, the droplet maintained a cyclic motion without breaking up. If the electric field strength is kept constant, this is a steady-state oscillation with a constant amplitude.



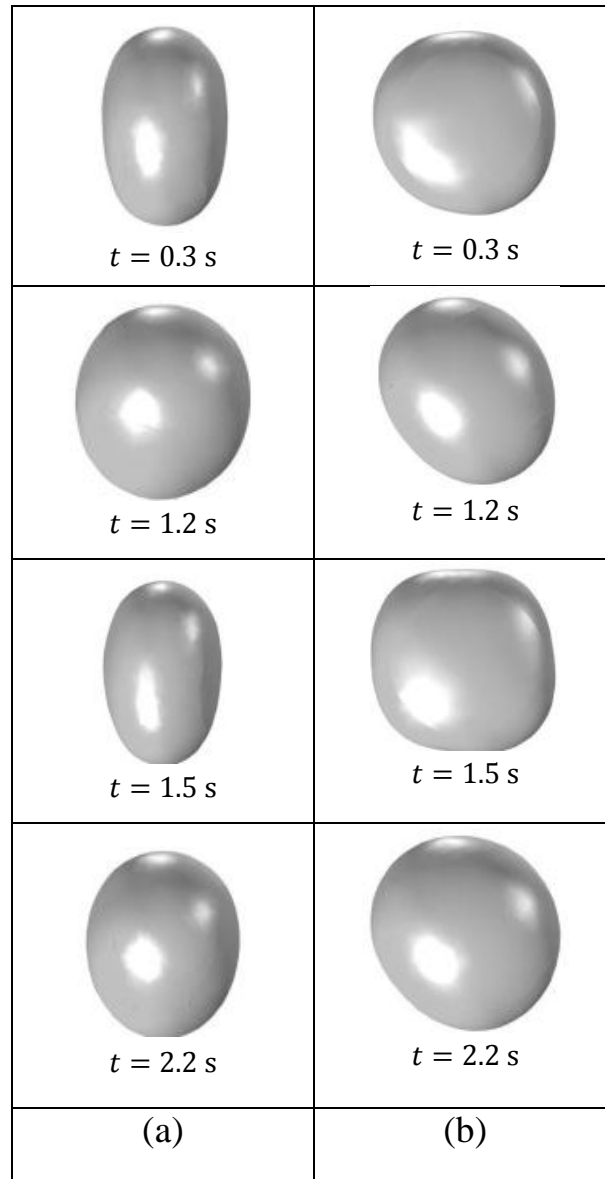


Figure 3.5 Sequence of images showing the oscillation of the 1.3 mm droplet for  $E=4$  kV/cm. (a) Observation normal to the applied electric field. (b) Observation parallel to the applied electric field.

It is obvious that the major axis of the droplet tilts, if it is observed from the direction parallel to the electric field. The droplet elongates in the direction which is normal to the electric field until  $t = 0.3$  s, then it starts coming back to its original position. At  $t = 1.2$  s the major axis of the droplet makes a tilt angle, then at  $t = 1.5$  s the major axis of the droplet loses the tilt angle and a new cycle is again repeated. Increasing the electric field

in this mode causes a decrease of the amplitude of oscillation in the direction parallel to the electric field.

The nature of oblate–prolate droplet oscillation is different from the ordinary resonant oscillation of the droplets. In Figure 3.6, the frequency of the oscillation is plotted versus  $Ca_E$  for  $R = 0.15$ ,  $S = 1.38$  and  $\lambda = 1.31$ . By increasing the electric field, the frequency of the oscillation will increase while the amplitude of the oscillation along the electric field (prolate deformation) will decrease.

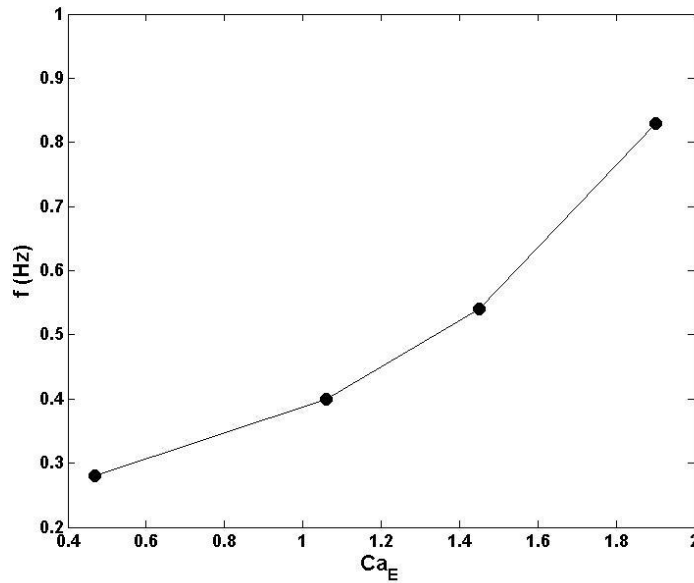


Figure 3.6 Frequency of droplet oscillation versus electric capillary number ( $Ca_E$ ) for  $R=0.15$ ,  $S=1.38$  and  $\lambda=1.31$

The frequencies were calculated based on the time interval between two maximum prolate deformations. For a sufficiently high electric field ( $Ca_E \geq 2.5$ ), no oscillations are observed and the break up will happen in a symmetric manner.

### 3.4.3 Break up

Further increasing of the electric field causes the droplet break up, which occurs in a symmetric manner. The droplet will first deform into a torus shape and this happens very fast comparing with the oscillation mode. This is the first time that this kind of break up has been captured numerically. Figure 3.7 illustrates the electrohydrodynamic burst of the

droplet with the radius of  $a = 1.3$  mm in  $E = 7$  kV/cm electric field and with the same physical properties as in the previous sections. The breakup starts with creation of the hole in the middle of the droplet. This hole grows and changes the droplet shape to the torus. The hole inside the droplet continues to grow and eventually leads to the droplet breakup.

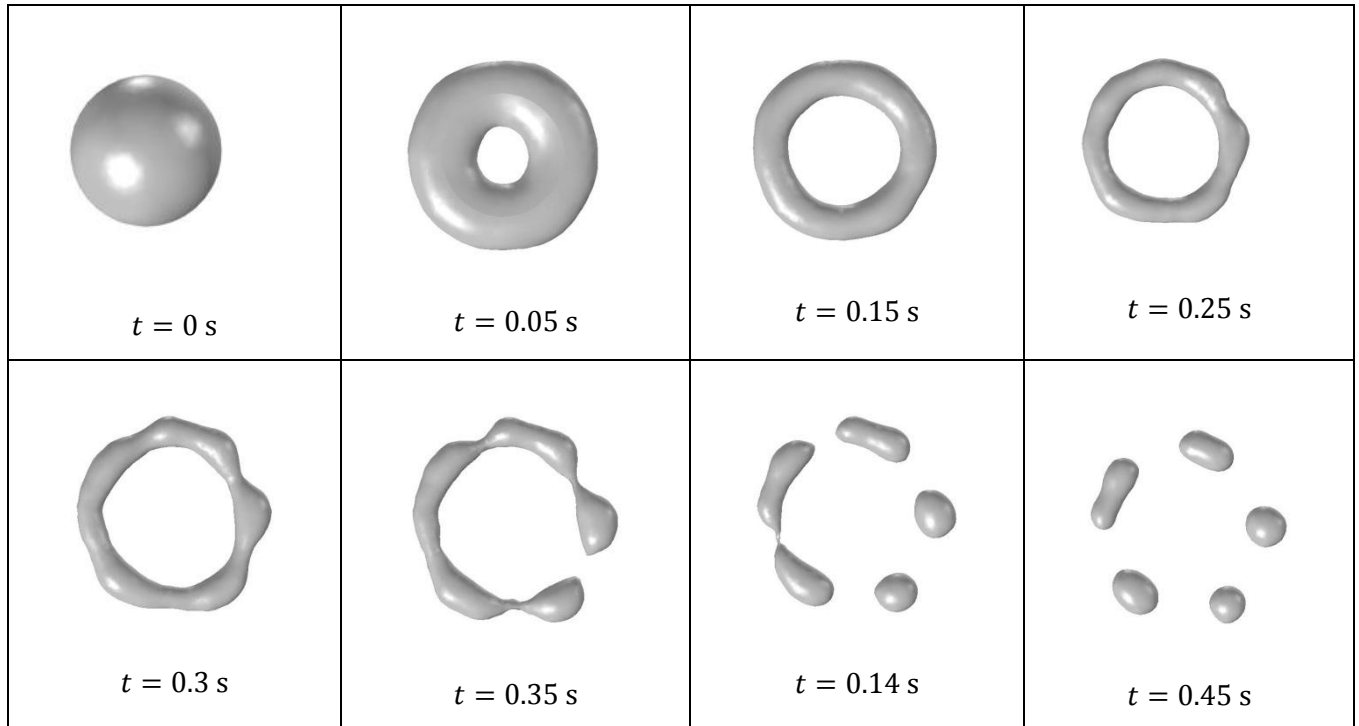


Figure 3.7 Sequence of images showing the breakup of the 1.3 mm droplet for  $E=7$  kV/cm

Charges carried by conduction accumulate at the interface. The electric field acting on these surface charges creates a tangential stress which drags the fluid into motion and forces the fluid away from the center. If  $RS < 1$ , the conduction in the ambient fluid is faster than that in the droplet, so charges at the droplet poles are repelled from the electrodes, pushing the droplet into an oblate shape caused by a hydrodynamic shear force acting on the interface. If the electric field strength exceeds some critical value, the droplet becomes flatter under the action of high electric field and the torus like shape is



formed. The torus expands in time to form a fluid ring, which subsequently disintegrates due to the capillary instabilities.

#### 3.4.4 Effect of viscosity and conductivity ratios on droplet breakup

It was observed by Ha and Yang [20, 21] that for the prolate-type deformation of a more conducting droplet, the critical electric capillary number weakly depends on the viscosity ratio. This is due to the fact that for a more conducting droplet the flow that results from the electrical stress is too weak to induce hydrodynamic effect on the droplet deformation and breakup. On the other hand the viscosity ratio can have significant effect on the breakup in this case. Figure 3.8 illustrates the effect of viscosity on the critical electric capillary number of this kind of breakup for two different conductivity ratios ( $R$ ). It is obvious that for highly viscous droplets, a stronger electric field is required for the droplet breakup. For a less viscous droplet, however, the electric energy will be transformed to viscous dissipation associated with the strong internal fluid motions. As a result, the higher electric energy is required to break up a less viscous droplet. It can be understood from Figure 3.6 that even though there is no variation in the electric field strength, the behaviour of the droplet may be controlled by changing the ratio of viscosity of the fluids in the system.

It is also clear that the conductivity ratio ( $R$ ) has a significant effect on the critical electric capillary number of the breakup and may change the behavior of the droplet. By decreasing the conductivity ratio ( $R = 0.05$ ) and keeping the same viscosity ratio ( $\lambda = 1.31$ ) and permittivity ratio ( $S = 1.38$ ), the breakup starts at lower electric capillary numbers ( $Ca_E=1.9$ ). For  $R = 0.15$ , the numerical results have also been compared with the available experimental data of Ha and Yang [14]. As mentioned before, the difference between numerical and experimental results can be attributed to the difference in measuring the conductivities of the oily fluids. The electrical conductivity of insulating oils is a material parameter which strongly depends on temperature and electric field strength and can also vary with ageing. These differences can reach easily one or even several orders of magnitude in different experimental conditions.

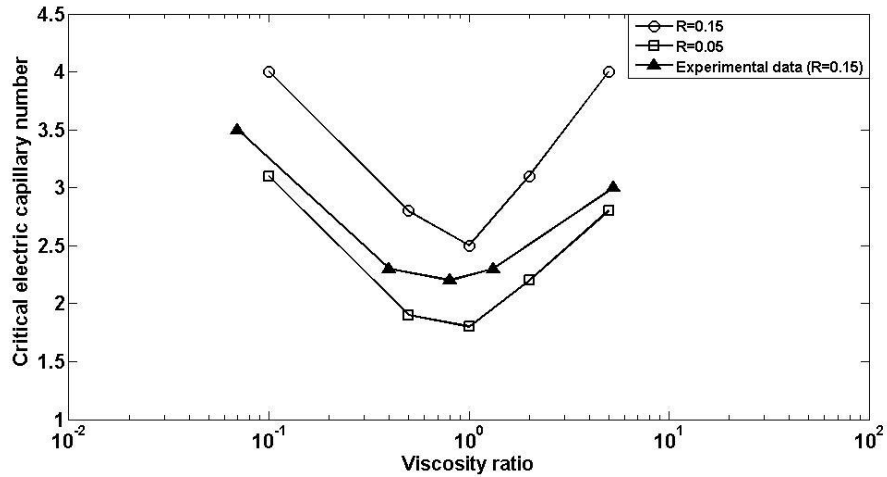


Figure 3.8 Critical electric capillary number as a function of the viscosity ratio for  $S=1.38$

Increasing the conductivity of the continuous phase will speed up the breakup and the rate of growing of the hole inside the droplet, so that the breakup will happen at a lower electric capillary number. Decreasing the conductivity ratio ( $R$ ) causes the induced electrical flow to become more powerful, resulting in faster breakup. Figure 3.9 shows the growing rate of the hole development inside the droplet at  $t = 0.05$  s for different values of  $R$ .

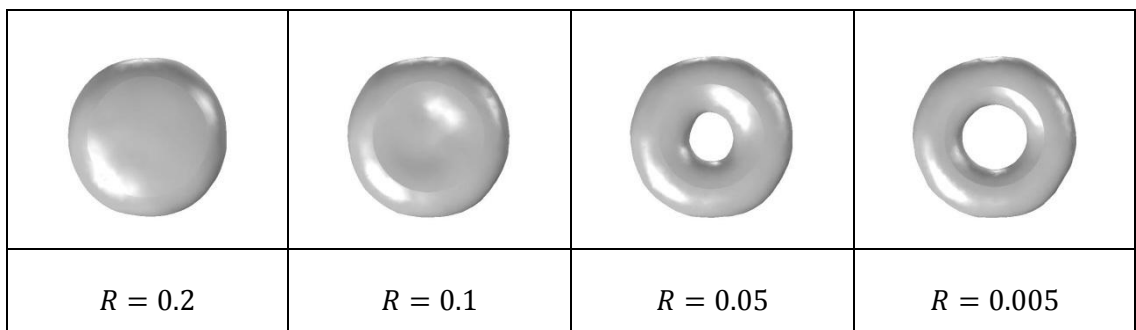


Figure 3.9 Droplet shape for different conductivity ratios ( $R$ ) at  $t=0.05$  s

It is obvious that for  $R = 0.2$  and  $R = 0.1$ , there is no hole at  $t = 0.05$  s, but for  $R = 0.05$  the hole has already been formed inside the droplet. Generally, a larger difference in the electrical conductivities will result in larger electric charge accumulation on the droplet surface, which induces larger deformation.

Figure 3.10 illustrates schematically an X-Y view of the flow patterns inside and outside the droplet. When a droplet reaches a steady prolate or oblate shape under the influence of an external electric field, circulating flow patterns of fluid can be formed both inside and outside of the droplet. The Taylor circulations are visible at  $t = 0$  and the fluid motion is from pole to equator. As time proceeds, the developed circulating flow patterns diminish, the flow pattern will change and the droplet will not keep a steady circulating flow as was predicted by Taylor's theory.

Because the fluid interface cannot support tangential stresses, the high tangential electric stress at the droplet interface accelerates the fluid in the breakup mode very quickly and the droplet will be squeezed into a plane under the effect of the high electric field intensities. This changing of the flow pattern will cause the droplet to be stretched in a plane parallel to the electrodes which finally lead to the axisymmetric breakup of the droplet.

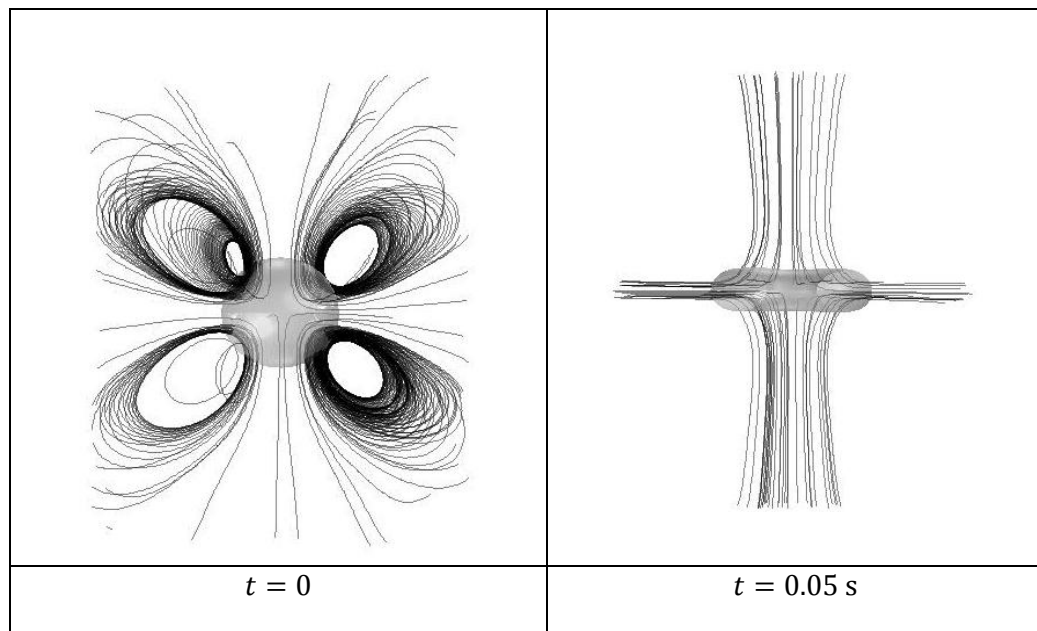


Figure 3.10 Flow patterns of the droplet for  $E=7 \text{ kV/cm}$  (XY view)

### 3.5 Conclusions

We have studied numerically the deformation of a droplet suspended in a uniform DC electric field. We observed that droplets experienced an oblate-prolate oscillatory motion with the tilted major axis. We have determined three types of behaviour for the droplets, which are less conducting than ambient fluid:

- Small deformation perpendicular to the electric field in accordance with Taylor theory, which happens at small electric capillary numbers.
- Oscillatory motion between the oblate and prolate deformation observed for moderate capillary numbers. The frequency of the oscillation was also investigated.
- Further increasing of the electric field causes the droplet to break up passing through a torus shape. The investigation of the effect of viscosity ratio on the droplet break up shows that there exists a minimum of the critical electric capillary number, at which breakup occurs. It was also observed that the onset of breakup will move to lower electric capillary numbers when the conductivity ratio ( $R$ ) decreases. We also characterized a specific kind of deformation (torus shape) which leads to the breakup and for the first time the effect of conductivity ratio ( $R$ ) on the breakup of less conducting droplet was investigated.

It was also revealed that the differences in experimental conditions such as measuring the conductivity ratio may change the value of critical electric capillary number and the droplet behaviour.

## References

- [1] G. I. Taylor, "Studies in electrohydrodynamics. I. Circulation produced in a drop by an electric field", *Proc. R. Soc. London, Ser. A*, vol. 291, no. 1425, pp. 159-166, 1966.
- [2] J. Q. Feng and T. C. Scott, "A computational analysis of electrohydrodynamics of a leaky dielectric drop in an electric field", *J. Fluid Mech.*, vol. 311, pp. 289-326, 1996.
- [3] E. Lac and G. M. Homsy, "Axisymmetric deformation and stability of a viscous drop in a steady electric field", *J. Fluid Mech.*, vol. 590, pp. 239-264, 2007.
- [4] J. Q. Feng, "Electrohydrodynamic behaviour of a drop subjected to a steady uniform electric field at finite electric Reynolds number," *Proc. R. Soc. London, Ser. A*, vol. 455, pp. 2245-2269, 1999.
- [5] N. Dubash and A. J. Mestel, "Behaviour of a conducting drop in a highly viscous fluid subject to an electric field", *J. Fluid Mech.*, vol. 581, pp. 469-493, 2007.
- [6] J. Hua, L. K. Lim and C. Wang, "Numerical simulation of deformation/motion of a drop suspended in viscous liquids under influence of steady electric fields", *Phys. Fluids*, vol. 20, pp. 113302-16, 2008.
- [7] A. M. Benselama, J. L. Achard and P. Pham, "Numerical simulation of an uncharged droplet in a uniform electric field", *J. of Electrostatics*, vol. 64, no. 7, pp. 562-568, 2006.
- [8] R. S. Allan and S. G. Mason, "Particle behavior in shear and electric fields. I. Deformation and burst of fluid drops", *Proc. R. Soc. London, Ser. A*, vol. 267, no. 1328, pp. 45-61, 1962.
- [9] S. Torza, R. G. Cox and S. G. Mason, "Electrohydrodynamic deformation and burst of liquid drops", *Philos. Trans. R. Soc. London, Ser. A*, vol. 269, no. 1198, pp. 295-319, 1971.
- [10] O. Vizika and D. A. Saville, "The electrohydrodynamic deformation of drops suspended in liquids in steady and oscillatory electric fields", *J. Fluid Mech.*, vol. 239, pp. 1-21, 1992.
- [11] N. Benteitis and S. Krause, "Droplet deformation in DC electric fields: the extended leaky dielectric model", *Langmuir*, vol. 21, no. 14, pp. 6194-6209, 2005.

- [12] J. W. Ha and S.M. Yang, “Deformation and breakup of Newtonian and non-Newtonian conducting drops in an electric field”, *J. Fluid Mech.*, vol. 405, pp. 131-156, 2000.
- [13] S. Krause and P. Chandratreya, “Electrorotation of deformable fluid droplets”, *J. Colloid Interface Sci.*, vol. 206, no. 1, pp. 10-18, 1998.
- [14] J. W. Ha and S. M. Yang, “Electrohydrodynamics and electrorotation of a drop with fluid less conductive than that of the ambient fluid”, *Phys. Fluids*, vol. 12, pp. 764-772, 2000.
- [15] H. Sato, N. Kaji, T. Mochizuki, and Y. H. Mori, “Behavior of oblately deformed droplets in an immiscible dielectric liquid under a steady and uniform electric field”, *Phys. Fluids*, vol. 18, pp. 127101-10, 2006.
- [16] P. F. Salipante and P. M. Vlahovska, “Electrohydrodynamics of drops in strong uniform DC electric fields”, *Phys. Fluids*, vol. 22, pp. 112110-9, 2010.
- [17] T. B. Jones, “Quincke rotation of spheres”, *IEEE Trans. Ind. Appl. IA-20*, vol. 845, pp. 845-849, 1984.
- [18] E. Olsson , G. Kreiss, “A conservative level set method for two phase flow”, *J. of Comp. Phys.*, vol. 210, no. 1, pp. 225-246, 2005.
- [19] Comsol Multiphysics User’s Guide, (COMSOL 4.2).
- [20] J. W. Ha and S. M. Yang, “Effects of surfactant on the deformation and stability of a drop in a viscous fluid in an electric field”, *J. Colloid Interface Sci.*, vol. 175, no. 2, pp. 369-385, 1995.
- [21] J.W. Ha and S.M. Yang, “Breakup of a multiple emulsion drop in a uniform electric field”, *J. Colloid Interface Sci.*, vol. 213, no. 1, pp. 92-100, 1999.

## Chapter 4

### 4 « Electric-field-induced oscillations of water droplets deposited on insulating surfaces »

#### 4.1 Introduction

Electric field is widely used as a tool to control the shape, the motion and the generation of small droplets of conductive liquids [1-4]. Electrowetting is one of the best methods to control the wetting behavior of liquid droplets on partially wetting surfaces by reducing the apparent contact angle of sessile droplets [5-7]. A water droplet located on a hydrophobic insulating surface deforms by the action of electric field and its motion depends on the material property of the droplet and the surface.

Under a DC electric field, a droplet located on an insulated surface elongates along the direction of the electric field and can form a water filament to bridge the electrodes [8]. On the other hand, the shape of the water droplet varies with time under an AC electric field, depending on the frequency of the electric field. High voltage AC outdoor insulators are conventionally classified into two categories: the ceramic insulators (glass or porcelain) and composite insulators (polymeric insulators). Physical robustness and low weight of composite insulators have made them become dominant over ceramic insulators over the last years [9, 10]. As a result of a higher degree of hydrophobicity, the water tends to remain in droplets on these materials, which have led to study the behaviour of individual droplets on polymeric surfaces. The vibration and distortion of the droplets in an AC field has been investigated experimentally [11-15]. The interaction of droplets on a surface of composite insulator and generation of conductive regions and filaments was studied experimentally in [16-18]. Krivda and Birtwhistle [19] showed that natural vibrations of a water droplet change its shape during the AC cycle and so can effectively increase the risk of flashover by reducing the insulation path.

Tiny droplets can be used as a medium for biochemical reactions as well as containers of biological particles. Using a patterned electrode array, droplets can be transported, mixed and split by controlling the contact angle in electrowetting [20-23].

When a liquid droplet is slowly placed on a solid, flat substrate, it spreads to its equilibrium configuration with the contact angle specified by Young's equation (see Figure 4.1):

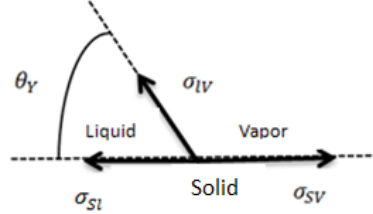


Figure 4.1 Force balance at the contact line

$$\cos \theta_Y = \frac{\sigma_{SV} - \sigma_{SL}}{\sigma_{LV}} \quad (4.1)$$

The surface energy (tension) between the two phases indicated by subscripts is denoted by  $\sigma$ . Thus, according to Young's equation, the contact angle  $\theta$  is a material parameter dependent only on the involved surface energies.

Electrowetting is well understood as long as the applied voltage is low. Sufficiently far away from the contact line, the voltage dependence of the contact angle is given by the Lippmann-Young equation [5],

$$\cos \theta_L = \cos \theta_Y + \eta \quad (4.2)$$

where  $\theta_L$  is the Lippmann contact angle,  $\theta_Y$  is Young's contact angle,  $\eta = \frac{\epsilon_0 \epsilon_r V^2}{2 \sigma d}$  is a dimensionless number representing the ratio of electrostatic and capillary forces,  $V$  is the applied electric potential,  $\sigma$  is the surface tension of the liquid,  $\epsilon_r$  and  $d$  are the dielectric constant and the thickness of the insulating layer, respectively,  $\epsilon_0$  is the electric susceptibility of vacuum.

It was found that the contact angle approaches Young's angle in the vicinity of the substrate, when the Lippmann angle is small [24]. The principles underlying common techniques for actuation of droplets and films have been recently reviewed by Darhuber



and Troian [25]. Applications of electrowetting include reprogrammable lab-on-a-chip systems [26], autofocus cell phone lenses [27], colored oil pixels for laptops and video-speed smart paper [28, 29].

The work presented here deals with a numerical study of droplet oscillation placed on different hydrophobic surfaces under the effect of applied AC voltage, including the effect of ambient gas. All of the previous numerical studies assumed conventional electrowetting configuration which can be modeled using axi-symmetric system [30-32]. There are no previous works on three dimensional numerical simulations of droplet oscillation in the tangential electric field. The simulation results demonstrate that the current numerical method may provide an effective approach to quantitatively analyze complex electrohydrodynamic problems. According to the available experimental data, three different kinds of hydrophobic surfaces with different static contact angles were investigated to clarify the resonance phenomenon mentioned in [11]. The electric field introduces additional interfacial stresses at the droplet interface and extensive computations were performed to assess the combined effects of electric fields, surface tension and inertia.

## 4.2 Problem statement

Figure 4.2 illustrates the 3-D model considered in this study. A small liquid droplet is deposited on a solid surface, surrounded by another immiscible fluid and exposed to an AC electric field, which is parallel to the solid surface. This field is generated by applying a sinusoidal electric potential difference to the parallel electrodes in the  $X$ - $Z$  planes.

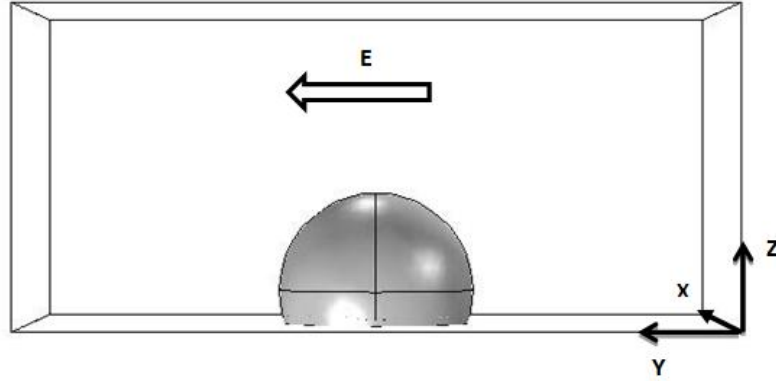


Figure 4.2 Model of a droplet deposited on a dielectric substrate and exposed to an electric field

The center of the droplet is placed in the middle of the rectangular cube. The interface separating the two fluids is assumed to have a constant interfacial tension coefficient. The size of the computational domain is 10 times the droplet radius in the direction of the electric field and 8 times the droplet radius in the directions normal to the electric field. At the initial stage, the shape of the droplet is assumed to be spherical and both fluids are motionless.

In order to investigate the dynamics of droplet deformation in an electric field it is necessary to solve the Navier-Stokes equations, describing the fluid motion, as well as to track the interface between both fluids. The two-phase flow system studied here is coupled with the applied electric field generated by the external voltage and electric charges accumulated on the droplet surface. Additional body forces are added to the Navier-Stokes equations for considering the surface tension ( $\mathbf{F}_{st}$ ) and electric stress ( $\mathbf{F}_{es}$ ).

$$\rho \frac{\partial \mathbf{u}}{\partial t} + \rho(\mathbf{u} \cdot \nabla)\mathbf{u} = \nabla \cdot [-p\mathbf{I} + \mu(\nabla\mathbf{u} + (\nabla\mathbf{u})^T)] + \rho\mathbf{g} + \mathbf{F}_{st} + \mathbf{F}_{es} \quad (4.3)$$

$$\nabla \cdot \mathbf{u} = 0$$

where  $\mathbf{u}$  denotes fluid velocity,  $\rho$  is the fluid density,  $\mathbf{g}$  is the gravitational acceleration,  $\mu$  is the dynamic viscosity,  $\mathbf{I}$  is the 3×3 identity matrix and  $p$  is the pressure. No-slip boundary conditions are applied for the electrodes. To describe the evolution of the

droplet shape, the Level-Set method [33], suitable for free boundary problems, is used. The method describes the evolution of the interface between the two fluids tracing an iso-potential curve of the level set function ( $\phi$ ). In general, inside the droplet  $\phi$  equals to one ( $\phi = 1$ ) and in ambient fluid  $\phi$  equals to zero ( $\phi = 0$ ). The interface is represented by the 0.5 contour of the level set function ( $\phi = 0.5$ ). The function  $\phi$  is governed by

$$\frac{\partial \phi}{\partial t} + \mathbf{u} \cdot \nabla \phi = \alpha \nabla \cdot \left( \epsilon_{ls} \nabla \phi - \phi(1 - \phi) \frac{\nabla \phi}{|\nabla \phi|} \right) \quad (4.4)$$

where  $\epsilon_{ls}$  is the parameter controlling the interface thickness and  $\alpha$  is the reinitialization parameter. The density and viscosity, which are different for oil and water, are automatically calculated from the level set variable  $\phi$ , as well as the surface tension force.

The electric forces cause the droplet deformation and they can be calculated from the electric field distribution, which depends on the position and shape of the droplet. In the absence of any time-varying magnetic field, the curl of the electric field is zero ( $\nabla \times \mathbf{E} = 0$ ) and the electric field can be expressed in terms of the electric potential  $V$ .

$$\mathbf{E} = -\nabla V \quad (4.5)$$

In a two-fluid system, assuming that the electric relaxation time is shorter than the time scale of the fluid motion, the electrical conductivity is constant within each fluid and the governing equation for the potential can be expressed in each medium as follows:

$$\nabla^2 V = 0 \quad (4.6)$$

$\mathbf{D}$  is the electric displacement,

$$\mathbf{D} = \epsilon_0 \epsilon_r \mathbf{E} \quad (4.7)$$

where  $\epsilon_0$  is the permittivity of vacuum and  $\epsilon_r$  is the relative permittivity. It is assumed that there is no space charge in the fluids except the surface charge on the interface, created by the difference between permittivities and conductivities of both fluids. Assuming that the fluids are incompressible, the electric stress can be calculated by taking the divergence of the Maxwell stress tensor, which couples electrostatic and

hydrodynamic phenomena. Neglecting the effect of magnetic field, the Maxwell stress tensor can be defined as:

$$\mathbf{T}_{Mij} = \varepsilon_r \varepsilon_0 E_i E_j - \frac{1}{2} (\varepsilon_r \varepsilon_0 E^2) \delta_{ij} \quad (4.8)$$

The momentum equation is modified by inserting the electric force,  $F_{es}$ , which can be determined by calculating the divergence of the Maxwell stress tensor ( $\mathbf{T}_M$ ):

$$\mathbf{F}_{es} = \nabla \cdot \mathbf{T}_M \quad (4.9)$$

The relative permittivity for each fluid is constant, but different. The volume fraction changes from zero in one fluid to one in the other one. In order to have all the physical properties at the interface, the two-phase relative permittivity ( $\varepsilon_r$ ) can be defined based on the volume fraction of both phases: permittivity of the droplet ( $\varepsilon_{in}$ ) and permittivity of the surrounding medium ( $\varepsilon_{ex}$ ):

$$\varepsilon_r = \varepsilon_{in} Vf_{in} + \varepsilon_{ex} Vf_{ex} \quad (4.10)$$

where  $Vf_{in}$  and  $Vf_{ex}$  are the volume fractions of the droplet and the continuous phase (fluid surrounding the droplet), respectively. Based on Eq. 4.10, inside the droplet,  $Vf_{in} = 1$  and  $Vf_{ex} = 0$  and  $\varepsilon_r = \varepsilon_{in}(1) + \varepsilon_{ex}(0) = \varepsilon_{in}$ . As the  $Vf_{in}$  changes from one (inside the droplet) to zero (outside the droplet), the relative permittivity changes smoothly from the value on one side to the value on the other side by Eq. (4.10).

Regardless of the contact angle value, there is no solution to the Navier–Stokes equations that would simultaneously satisfy all classical boundary conditions on the free surface and the solid boundary [34-37].

The wetted wall boundary condition is suitable for solid walls in contact with a fluid-fluid interface. For the Level-Set method, this boundary condition enforces the slip condition  $\mathbf{u} \cdot \mathbf{n}_{wall} = 0$  and adds a frictional force of the form

$$\mathbf{F}_{fr} = -\frac{\mu}{\beta} \mathbf{u} \quad (4.11)$$

where  $\beta$  is the slip length.

It was found that the *local* contact angle in electrowetting is equal to Young's angle independently of the applied voltage [38, 39]. COMSOL [40], a commercial software implementing the finite element method, was used for solving the above equations. The components of the electric field are calculated by the Electrostatics interface. Their predefined variable names, along with the variable names of the permittivities can be used directly to set up expressions calculating the components of the Maxwell stress tensor. The Laminar Two-Phase Flow and Level-Set interface sets up the equations for the fluid motion according to the Navier-Stokes equations.

For simplicity, we assume that the droplet has initially a constant semi-spherical cap shape. To quantify the degree of the deformation of the water droplet, an aspect ratio which corresponds to the width on the height ratio of the water droplet is shown in Figure 4.3.

$$A = \frac{W}{H} \quad (4.12)$$

The aspect ratios of water droplet at the moment of the elongation and shrinking are, respectively, defined as  $A_e$  and  $A_s$ .

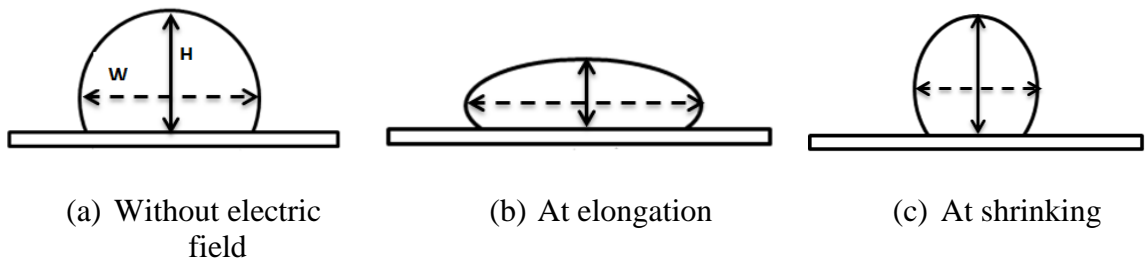


Figure 4.3 Definition of the aspect ratio

We consider here a single spherical sessile droplet under applied external fields (such as gravity and electric potentials). According to Figure 4.4, if  $\theta$  increases,  $R$  must decrease to keep the volume constant. The droplet volume,  $v$ , is given by

$$v(R, \theta) = \pi R^3 \left( \frac{2}{3} - \frac{3 \cos \theta}{4} + \frac{\cos 3\theta}{12} \right) \quad (4.13)$$

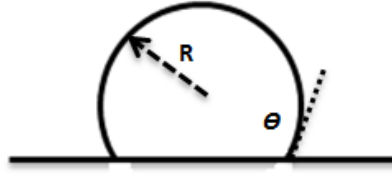


Figure 4.4 Spherical drop geometry defined by radius  $R$  and contact angle  $\theta$

### 4.3 Results and discussion

3-D simulations of droplet oscillation under the effect of electric field on different hydrophobic surfaces were performed for the following parameters: the densities  $\rho_{water} = 1000 \text{ Kg/m}^3$ ,  $\rho_{air} = 1.25 \text{ Kg/m}^3$ , viscosities  $\mu_{water} = 1 \times 10^{-3} \text{ Pa s}$ ,  $\mu_{air} = 1.82 \times 10^{-5} \text{ Pa s}$ , surface tension  $\sigma = 7.2 \times 10^{-2} \text{ N/m}$ , relative permittivities  $\epsilon_{water} = 80$ ,  $\epsilon_{air} = 1$ , gravity  $9.8 \text{ m/s}^2$ . As a validation, the numerical result will be compared with the experimental ones [11], in which a water droplet oscillates on a hydrophobic substrate.

To study the importance of using appropriate contact angles, the numerical simulations were conducted using three different equilibrium contact angles. Based on the available experimental data, the values of the contact angles are shown in Table 4.1; each value given is an average of three measurements [11]. Unfortunately, the dynamic contact angle was not measured in the experiment.

Table 4.1 Contact angles of a water droplet on different materials

Material	SR	PTFE	PGF
Static contact angle (°)	110	100	90

A single water droplet with a volume of  $10 \mu\text{l}$  has been assumed in all cases. In order to keep the volume of the droplet constant (4.13), the radius of the droplet has to decrease with the increasing contact angle. First, the effect of the AC frequency for a water droplet

placed on a specific hydrophobic surface has been studied in order to identify the frequency that causes the maximum deformation. Subsequently, different hydrophobic surfaces were considered and the effect of contact angle on the droplet deformation was simulated. It was assumed that the droplet phase and the suspending fluid are the perfect conductor and perfect insulator, respectively.

The simulations were initialized by suddenly applying a sinusoidal electric potential to the right electrode. When an initially circular liquid droplet is exposed to an external time-varying electric field it deforms with a time-dependent shape and orientation.

Depending on the hydrophobic insulating sheet, a water droplet was significantly deformed only at a particular frequency range of the AC electric field. It was found that for a surface with the contact angle of  $110^\circ$ , the water droplet oscillates distinctively around 34 Hz electric field. Figure 4.5 shows snapshots of the numerical results for  $\theta=110^\circ$ ,  $f = 34$  Hz and  $V = 5$  kV. The droplet first elongates in the direction of the electric field to a maximum value ( $t = 10$  ms), which doesn't coincide with the instant of maximum of applied voltage, and it deforms into a flat shape. As it was observed experimentally, the motion of the water droplet was always delayed with respect of the time variation of the applied voltage. It should also be noted that the droplet deforms twice in one complete cycle of the electric field.

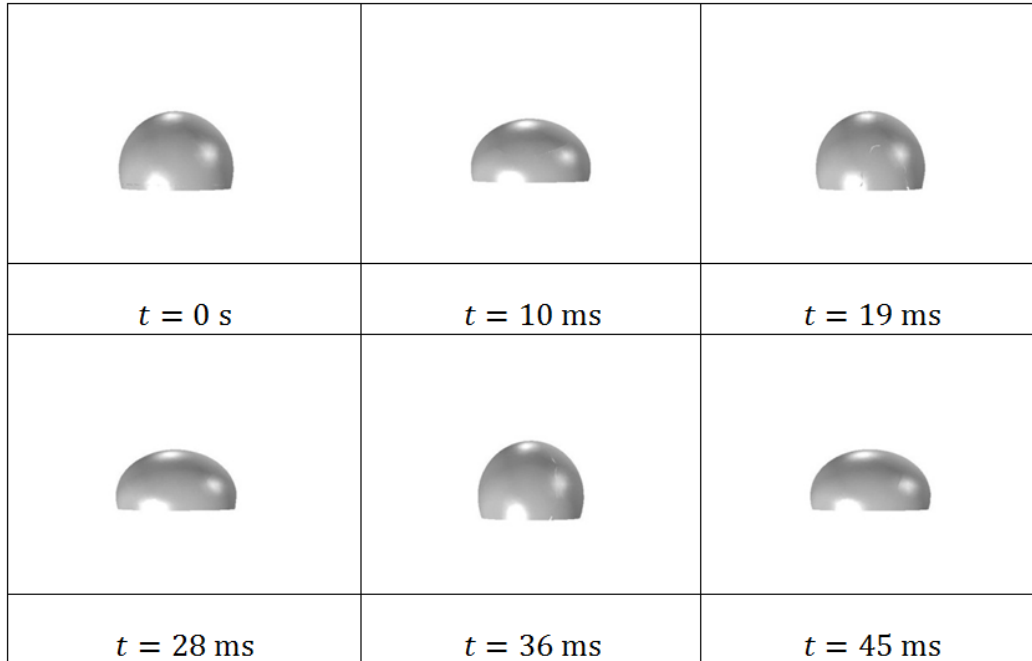


Figure 4.5 Snapshots of numerical result for  $\theta=110^\circ$ ,  $f=34 \text{ Hz}$  and  $V=5 \text{ kV}$

The numerical results show good agreement with the experimental study of Yamada et al. [11] for the SR surface with the static contact angle of around  $110^\circ$ . The static contact angle of a water droplet on the SR sheet was the largest among all the materials used in their study. The ratio of  $\frac{A_e}{A_s}$  for a  $10 \mu\text{l}$  water droplet as a function of the frequency of the applied voltage for  $5 \text{ kV}$  is shown in Figure 4.6. The droplet vibrates strongly between  $30$  and  $40 \text{ Hz}$ . This phenomenon could be regarded as resonance of the water droplet.

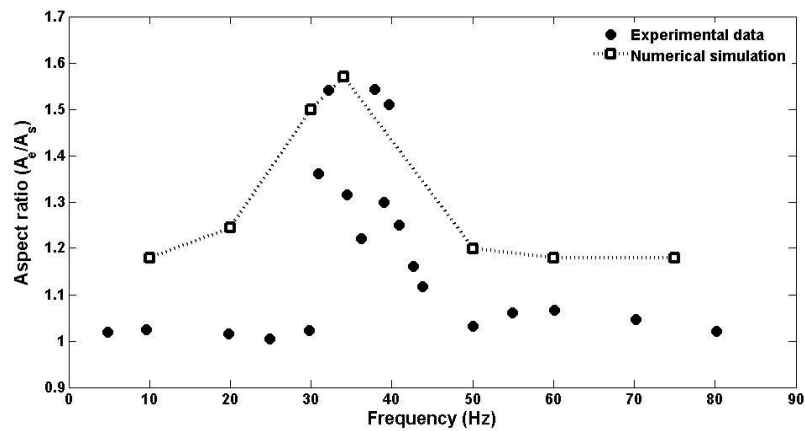




Figure 4.6 Aspect ratio  $A_e/A_s$  as a function of the frequency of the applied AC electric field for  $\theta=110^\circ$

It can also be observed that the experimental ratio  $A_e/A_s$  is practically equal to one, while the numerical simulation overestimates this number. This is because not only the electric field, but also some other surface factors in experiments, such as roughness and changing in wetting conditions, may affect the droplet behavior.

It was also observed experimentally [11] that there is a noticeable difference between the contact angles during elongation and shrinking phases for a water droplet placed on the SR sheet at the resonant frequency comparing to PTFE and PGF sheets. In practice, the surface of the SR sheet is stickier than the PTFE and PGF surfaces. Changing the surface properties Eq. (4.1) during the elongation and shrinking phases changes the surface energies and consecutively the contact angle, which would affect the behavior of a water droplet on each sheet.

To study the effect of the surface contact angle on the droplet deformation the numerical simulation was also conducted for different surface contact angles. Figure 4.7 shows the time variation of the deformation of a 10 $\mu$ L water droplet deposited on the surface with the contact angle of  $90^\circ$  (PGF). In this case, the numerical results also show good agreement with the experimental study of Yamada et al. [11]

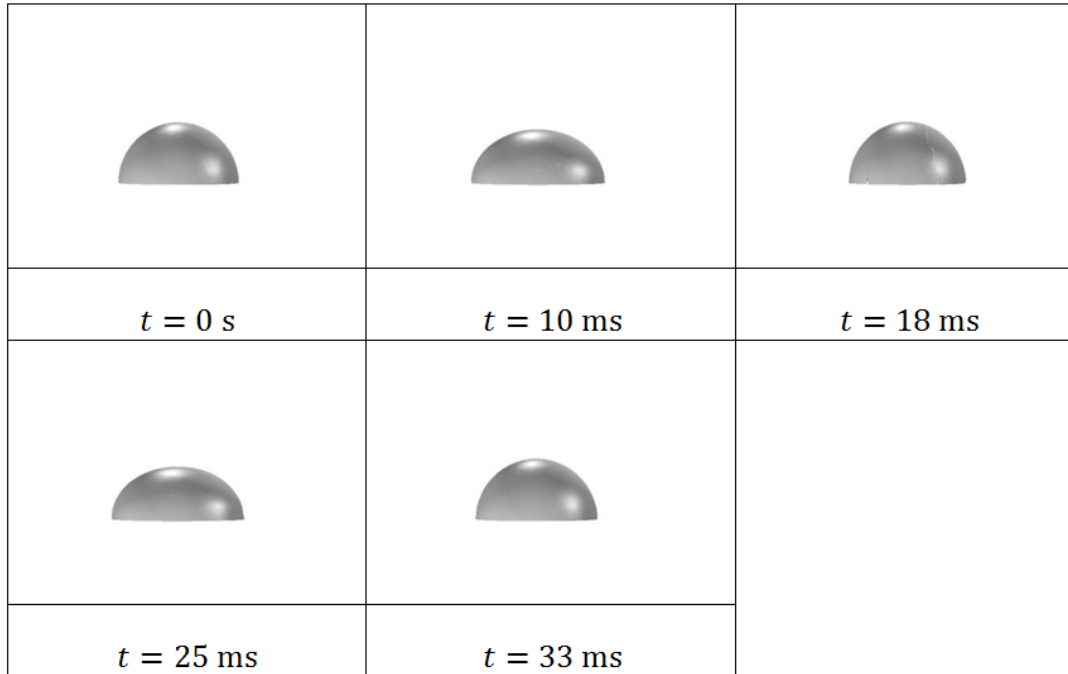


Figure 4.7 Snapshots of numerical result for  $\theta=90^\circ$ ,  $f=40 \text{ Hz}$  and  $V=5 \text{ kV}$

The resonance frequency not only depends on the volume of the water droplet, but also on the surface properties of the hydrophobic insulating sheet. It is clear from Figure 4.8 that the water droplet located on the surface with the contact angle of  $90^\circ$  significantly deforms in the frequency of 40 Hz, which is higher than that for  $\theta = 110^\circ$ .

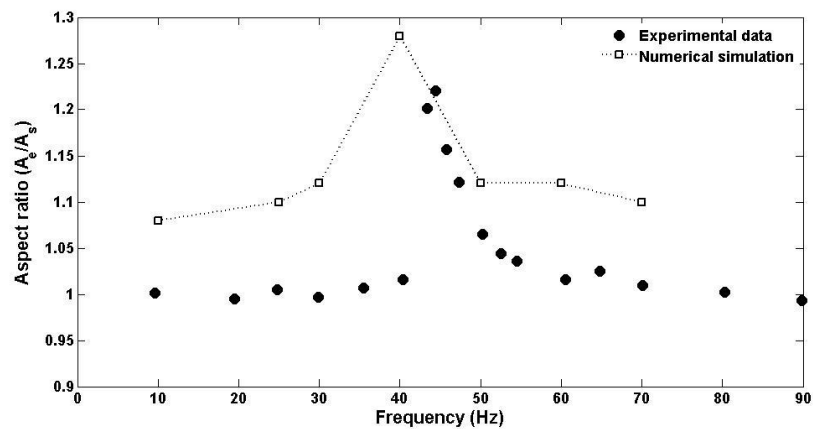


Figure 4.8 Aspect ratio  $A_e/A_s$  as a function of the frequency of the applied AC electric field for  $\theta=90^\circ$

We believe that the contact angle is a key factor affecting the droplet resonance: the resonance frequency of the water droplet deposited on a hydrophobic surface increases with a decreasing contact angle. This means that a droplet with a smaller contact angle will require an electrostatic force with a shorter duration (higher frequency) in order to become dominant over the inertia. It can be deduced that the natural oscillation frequency of a droplet maintained at constant volume increases by decreasing the contact angle.

Figure 4.9 shows the snapshots of the droplet deformation assuming the contact angle of  $100^\circ$  for  $f = 35$  Hz (resonance frequency) and  $f = 50$  Hz (commercial frequency) of the applied voltage of 5 kV. The snapshots were taken at the moment of maximum elongation and maximum shrinking for each of those frequencies. Comparing the maximum elongation snapshots (2, 4, 6 and 8), it is clear that the droplet deforms more strongly for  $f = 35$  Hz.

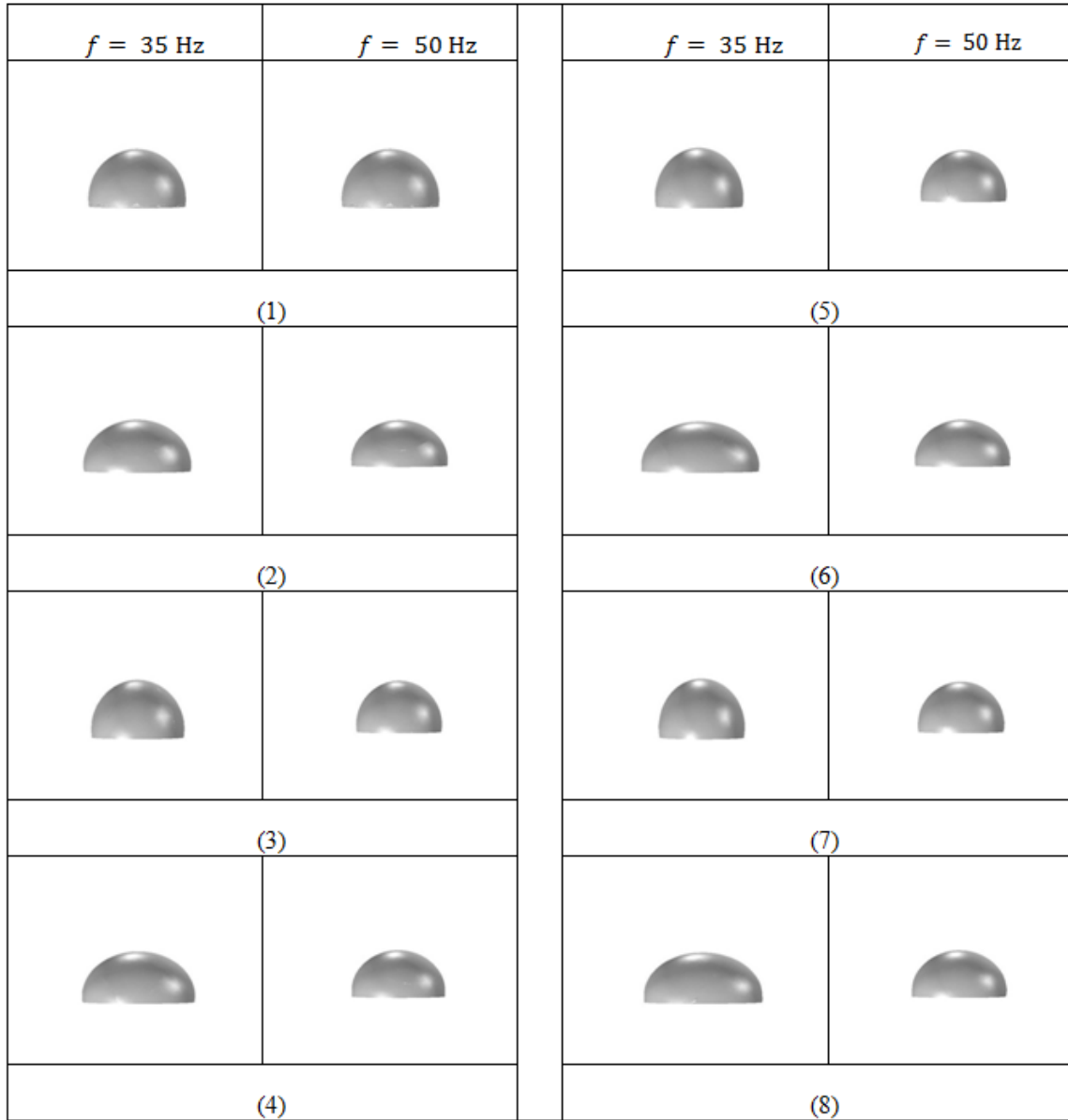


Figure 4.9 Snapshots of a  $10 \mu\text{l}$  water droplet located on a surface with  $\theta=100^\circ$  in (a) resonant frequency of 35 Hz and (b) commercial frequency of 50 Hz

Figure 4.10 shows the effect of the volume of the droplet on the resonant frequency for the SR sheet. The resonance frequency of the water droplet on the SR sheet decreased with increasing droplet volume. The resonant frequencies are in good agreement with the experimental data of Yamada et al. [11] for the range of 5 to  $30 \mu\text{L}$ . The differences

between the experimental data and numerical results could be the result of the contact angle changing due to the stickiness of the surface. Considering the dynamic contact angle is a promising way to consider the effect of the surface parameters.

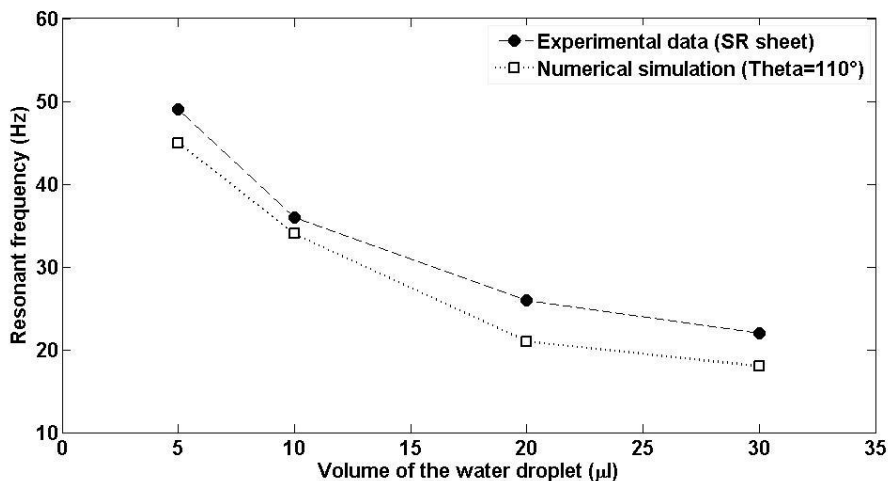


Figure 4.10 Resonant frequencies as a function of the volume of the water droplet

## 4.4 Conclusions

The effect of an electric field on a periodic deformation of viscous droplets placed on hydrophobic surfaces has been studied in this article. The numerical approach is based on the classical Navier–Stokes equations for the fluid motion and the level set technique for the evolution of the fluid–fluid interface. Moreover, the Maxwell stress tensor is employed to incorporate the interfacial stresses generated by the electric field into the momentum equations as volumetric source terms.

The presented algorithm can reproduce droplet oscillations on a surface considering different contact angles. It has been found that the resonance frequency of the water droplet depends on the surface property of the hydrophobic materials and the electrostatic force. The numerical results show that even by using the static contact angle, the dependence of the resonance frequency on the contact angle is in good agreement with the available experimental data and the resonant phenomenon can be observed.

## References

- [1] G. Taylor, "Disintegration of water drops in an electric field", Proc. Roy. Soc. A, vol. 280, no. 1382, pp. 383-397, 1964.
- [2] G. I. Taylor, "Studies in electrohydrodynamics. I. Circulation produced in a drop by an electric field", Proc. R. Soc. London, Ser. A, vol. 291, no. 1425, pp. 159-166, 1966.
- [3] J. B. Fenn, M. Mann, C. K. Meng, S. F. Wong and C. M. Whitehouse, "Electrospray ionization for mass spectrometry of large biomolecules", Science, vol. 246, no. 4926, pp. 64-71, 1989.
- [4] A. A. Darhuber and S. M. Troian, "Principles of microfluidic actuation by modulation of surface stresses", Ann. Rev. Fluid Mech., vol. 37, pp. 425-455, 2005.
- [5] G. Lippmann, "Relations entre les phénomènes électriques et capillaires," Ann. Chim. Phys., vol. 5, pp. 494-549, 1875.
- [6] F. Mugele and J. C. Bare, "Electrowetting: from basics to applications", J. Phys.: Condens. Matter, vol. 17, pp. 705-774, 2005.
- [7] C. Quilliet and B. Berge, "Electrowetting: a recent outbreak", Curr. Opin. Colloid Interface Sci., vol. 6, no. 1, pp. 34-39, 2001.
- [8] Y. Higashiyama, S. Yanase, T. Sugimoto, "Behavior of water droplet located on a hydrophobic insulating sheet under DC field", Proc. of the IEEE IAS Annual Meeting, vol. 3, pp. 1808-1813, 1998.
- [9] J.S. Looms, "Insulators for High Voltages", (London: Peter Peregrinus/IEE), 1988.
- [10] A. Haddad and D. F. Warne, "Advances in High Voltage Engineering", (London: IEE), ISBN 0 85296 158 8, 2004.
- [11] T. Yamada, T. Sugimoto, Y. Higashiyama, M. Takeishi, and T. Aoki, "Resonance phenomena of a single water droplet located on a hydrophobic sheet under AC electric field", IEEE Trans. on Ind. Appl., vol. 39, no. 1, pp. 59-65, 2003.
- [12] Y. Higashiyama, T. Yamada and T. Sugimoto, "Vibration of water droplet located on a hydrophobic sheet under AC field", Proc. IEEE, IAS Annual Meeting (Phoenix), vol. 3, pp. 1825-1830, 1999.
- [13] Y. Higashiyama, T. Yamada and T. Sugimoto, "Effect of resonance of a water droplet located on a hydrophobic sheet on AC flashover", Proc. IEEE, IAS Annual Meeting (Pittsburgh), vol. 3, pp. 2198-2203, 2002.

- [14] Y. Higashiyama, T. Takada, T. Sugimoto, "Resonant vibration and flashover phenomena of a water droplet located on a hydrophobic sheet under AC field", *J. of Electrostat.*, vol. 63, no. 6, pp. 883-889, 2005.
- [15] T. Schutte and S. Hornfeldt, "Dynamics of stressed water drops on insulating surfaces", *IEEE Int. Symp, Electr. Ins.*, pp. 202-207, 1990.
- [16] G. G. Karady, "Flashover mechanism of non-ceramic insulators", *IEEE Trans. Dielectr. Electr. Insul.*, vol. 6, pp. 718-723, 1999.
- [17] G. G. Karady, M. Shah and R. L. Brown, "Flashover mechanism of silicone rubber insulators used for outdoor insulation-I", *IEEE Trans. Power Delivery*, vol. 10, pp. 1965-1971, 1995.
- [18] M. Shah, G. G. Karady and R. L. Brown, "Flashover mechanism of silicone rubber insulators used for outdoor insulation-II", *IEEE Trans. Power Delivery*, vol. 10, no. 4, pp. 1972-1978, 1995.
- [19] A. Krivda and D. Birtwhistle, "Breakdown between water drops on wet polymer surfaces", *IEEE Conf. on Electr. Insul. and Dielectr. Phenomena*, pp. 572-80, 2001.
- [20] M. G. Pollack, R. B. Fair, and A.D. Shenderov, "Electrowetting-based actuation of liquid droplets for microfluidic applications", *Appl. Phys. Lett.*, vol. 77, pp. 1725-1727, 2000.
- [21] S. K. Cho, H. Moon, and C. J. Kim, "Creating, transporting, cutting, and merging liquid droplets by electrowetting-based actuation for digital microfluidic circuits", *J. of Microelectromech. Sys.*, vol. 12, no. 1, pp. 70-80, 2003.
- [22] F. Mugele, J. C. Baret, and D. Steinhauser, "Microfluidic mixing through electrowetting-induced droplet oscillations", *Appl. Phys. Lett.*, vol. 88, pp. 204106-3, 2006.
- [23] K. P. Nichols and Han J. G. E. Gardeniers, "A digital microfluidic system for the investigation of pre-steady-state enzyme kinetics using rapid quenching with MALDI-TOF mass spectrometry", *Anal. Chem.*, vol. 79, pp. 8699-8704, 2007.
- [24] J. Buehrle, S. Herminghaus, and F. Mugele, "Interface profiles near three-phase contact lines in electric fields", *Phys. Rev. Lett.*, vol. 91, no. 8, pp. 86101-4, 2003.
- [25] A. A. Darhuber and S. M. Troian, "Principles of microfluidic actuation by modulation of surface stresses", *Ann. Rev. Fluid Mech.*, vol. 37, pp. 425-559, 2005.

- [26] J. Lee, H. Moon, J. Fowler, T. Schoellhammer, and C. J. Kim, "Electrowetting and electrowetting-on dielectric for microscale liquid handling", *Sens. Actuators A*, vol. 95, no. 2, pp. 259-268, 2002.
- [27] B. Berge and J. Peseux, "Variable focal lens controlled by an external voltage: An application of electrowetting", *Eur. Phys. J. E*, vol. 3, pp. 159-163, 2000.
- [28] R. A. Hayes and B. J. Feenstra, "Video-speed electronic paper based on electrowetting", *Nature London*, vol. 425, pp. 383-385, 2003.
- [29] T. Roques Carmes, R. A. Hayes, B. J. Feenstra, and L. J. M. Schlangen, "Liquid behavior inside a reflective display pixel based on electrowetting", *J. Appl. Phys.*, vol. 95 pp. 43-89, 2004.
- [30] J. S. Hong, S. H. Ko, K. H. Kang and I. S. Kang, "A numerical investigation on AC electrowetting of a droplet", *Microfluid Nanofluid.*, vol. 5, pp. 263-271, 2008.
- [31] H. Lee, S. Yun, S. H. Ko, and K. H. Kang, "An electrohydrodynamic flow in AC electrowetting", *Biomicrofluid.*, vol. 3, pp. 044113-12, 2009.
- [32] P. García-Sánchez, A. Ramos and F. Mugele, "Electrothermally driven flows in AC electrowetting", *Phys. Rev. Lett E*, vol. 81, pp. 015303(R), 2010.
- [33] E. Olsson , G. Kreiss, "A conservative level set method for two phase flow", *J. of Comp. Phys.*, vol. 210, pp. 225-246, 2005.
- [34] Y. D. Shikhmurzaev, "Capillary flows with forming interfaces", Chapman & Hall/CRC: Boca Raton, FL, 2007.
- [35] Y.D. Shikhmurzaev, "Singularities at the moving contact line. mathematical, physical and computational aspects", *Physica D: Nonlinear Phenomena*, vol. 217, pp. 121-133, 2006.
- [36] C. Huh, L.E. Scriven, "Hydrodynamic model of steady movement of a solid/liquid/fluid contact line", *J. of Colloid and Interface Sci.*, vol. 35, pp. 85-101, 1971.
- [37] E.B. Dussan and S.H. Davis, "On the motion of a fluid–fluid interface along a solid surface", *J. of Fluid Mech.*, vol. 65, pp. 71-95, 1974.
- [38] F. Mugele and J. Buehrle, "Equilibrium drop surface profiles in electric fields", *J. Phys. Condens. Matter*, vol. 19, pp. 375112 (20 pp), 2007.
- [39] K. Adamiak, "Capillary and electrostatic limitations to the contact angle in electrowetting-on-dielectric", *Microfluid. and Nanofluid.*, vol. 2, pp. 471-480, 2006.



[40] Comsol Multiphysics User's Guide, (COMSOL 4.2), <http://www.comsol.com/>

## Chapter 5

### 5 « Oscillation, pseudo-rotation and coalescence of sessile droplets in a rotating electric field »

#### 5.1 Introduction

Using an electric field as a tool to control the shape, the motion, and the generation of small droplets has recently received significant attention because of its lack of moving parts and low power consumption [1-4]. Electrowetting is one of the best methods to control the wetting behavior of liquid droplets on partially wetting surfaces by reducing the apparent contact angle of sessile droplets [5-7]. A water droplet located on a hydrophobic insulating surface deforms by the action of electric field and its motion depends on the material properties of the droplet and the surface. Under a DC electric field, a droplet elongates in the direction of the electric field and can form a water filament to bridge the electrodes [8].

Electrowetting using AC actuation voltages has also drawn attention [9-13]. The main advantage of using AC voltages over DC includes a decrease in the contact angle hysteresis. The shape of the water droplet varies with time under an AC electric field, depending on the frequency of the electric field. The interaction of droplets deposited on a surface of a composite insulator and generation of conductive regions and filaments was studied experimentally in [14-16]. Krivda and Birtwhistle [17] showed that the natural vibrations of a water droplet result in a change of its shape during the AC cycle and so can effectively increase the risk of flashover by reducing the length of the insulation path. Oscillations of sessile droplets in electrowetting on a dielectric with a coplanar-electrode configuration under the actuation of AC voltage with different frequencies were studied experimentally by Hong et al. [18]. It was found that the experimental resonance frequencies and the number of lobes at different resonance modes agree reasonably well with the previous linear analysis. The transient response of a millimeter-sized sessile droplet to an electrical actuation was experimentally investigated by Dash et al. [19]. Systematic experiments were conducted over a frequency range of 5-200 Hz and actuation voltages of 40-80 V<sub>rms</sub> to determine the

dependence of droplet oscillation on these parameters. The dependence of the contact angle and contact radius on the applied frequency and voltage of a periodic sinusoidal signal was revealed. The experimentally determined resonance frequencies were shown to be well estimated by Lamb's expression [20] for the natural frequency of a droplet. Amplitude and phase spectra and the beat phenomenon of water droplet oscillation driven by AC electrowetting have been studied using a frequency scanning method by Lai et al. [21]. It was found that at resonant frequencies of water droplets phase differences between the driving voltage and the droplet motion are  $\pm 90^\circ$ .

When a liquid droplet is slowly placed on a solid, flat substrate, it spreads to its equilibrium configuration with the contact angle specified by Young's equation:

$$\cos \theta_Y = \frac{\sigma_{SV} - \sigma_{SL}}{\sigma_{LV}} \quad (5.1)$$

where the surface energy (tension) between the various phases indicated by subscripts (S – solid, V – vapour, L – liquid) is denoted by  $\sigma$ . Thus, according to Young's equation, the contact angle  $\theta$  is a material parameter dependent only on the involved surface energies. Electrowetting is well understood as long as the applied voltage is low. Sufficiently far away from the contact line, the voltage dependence of the contact angle is given by the Lippmann equation [5]

$$\cos \theta_L = \cos \theta_Y + \eta \quad (5.2)$$

where  $\theta_L$  is the Lippmann contact angle,  $\theta_Y$  is Young's contact angle,  $\eta = \frac{\epsilon_0 \epsilon_r V^2}{2 \sigma_{LV} d}$  is a dimensionless number representing the ratio of electrostatic and capillary forces,  $V$  is the applied electric potential,  $\epsilon_r$  and  $d$  are the dielectric constant and the thickness of the insulating layer, respectively, and  $\epsilon_0$  is the dielectric permittivity of vacuum. It was found that the contact angle approaches Young's angle in the vicinity of the substrate, when the Lippmann angle is small [22, 23].

The rotation of particles in an electric field has also been considered in the literature to investigate the rotation of living cells and human peripheral blood lymphocytes [24, 25].

The rotation and stability of a weakly conducting droplet around its axis of symmetry under the action of the external electric field was investigated by Dolinsky and Elperin [26, 27]. It was shown that depending upon the ratios of the particle electric conductivity and permittivity to the corresponding parameters of the host medium the direction of rotation of the particle can be in the same or opposite to the direction of rotation of the external electric field.

The flow field generated during droplet oscillation at low AC frequencies can be used to enhance the mixing in a droplet [28, 29]. Mugele et al. [30] studied the frequency dependence of the internal flow field on a droplet using tracer particle tracking. Paik et al. [31] studied the mixing caused by droplet motion between parallel plates. The effect of shape oscillation on the internal mixing pattern of a droplet has been studied by Miraghaie et al. [32].

The first part of this paper is devoted to the numerical study of droplet oscillation placed on different hydrophobic surfaces under the effect of applied rotating AC electric field including the effect of the ambient gas. The first set of simulations investigated the effect of the rotating AC frequency and identified the resonant frequency. Subsequently, different hydrophobic surfaces were considered.

In the second part of this study, the coalescence and merging of two droplets are reported. This is the first time that the electro-coalescence of droplets placed on a hydrophobic surface has been numerically investigated considering the effect of the frequency of the applied AC field.

## 5.2 Problem statement

Fig. 1 illustrates the top view and the 3-D model of the configuration considered in our study for a droplet behaviour in the rotating electric field. A small liquid droplet is deposited on a solid surface, surrounded by another immiscible fluid and exposed to a rotating AC electric field, which is parallel to the solid surface. This field is generated by applying a sinusoidal electric potential difference to the orthogonal electrodes having  $90^\circ$  phase shift relative to each other.

The center of the droplet is placed in the middle of the square. The interface separating the two fluids is assumed to have a constant interfacial tension coefficient. The electrodes distance is 10 times the droplet radius and the size of the computational domain in the vertical direction is 5 times the droplet radius. At the initial stage, the shape of the droplet is assumed to be a spherical cap and both fluids are motionless. In order to check the effect of domain size on the numerical results, three different distances between electrodes have been tested: 8, 10, and 12 times the initial droplet radius. It was found that the calculated aspect ratios did not vary significantly, if the electrode distance is 10 times the radius or higher. Therefore, all further simulations were performed using this domain size. The wetting boundary condition is applied to the bottom wall and pressure-outlet with no viscous stress is applied to the other boundaries.

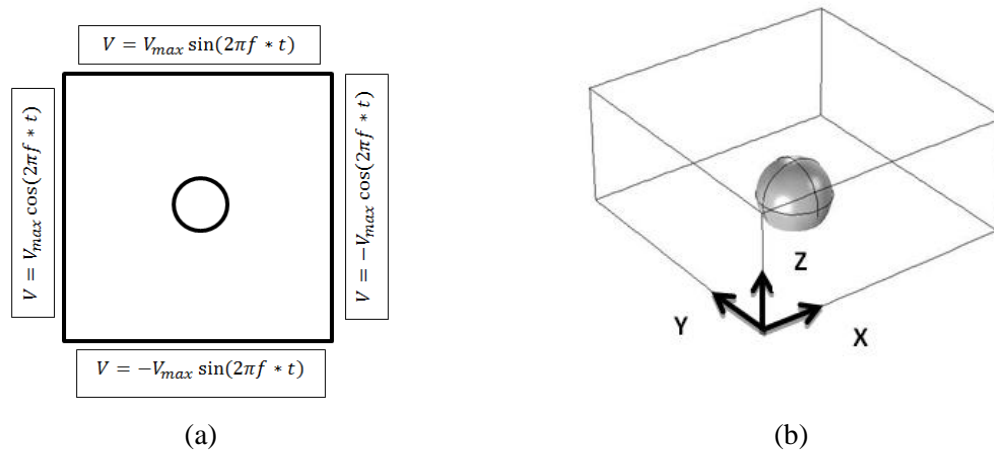


Figure 5.1 Model of a sessile droplet in a rotating field (a) Top view, (b) 3-D model.

The details of the numerical algorithm have already been described in Chapter 2. In order to investigate the dynamics of droplet deformation in an electric field it is necessary to solve the Navier-Stokes equations, governing the fluid motion, as well as track the interface between both fluids. The laminar two-phase flow studied here is coupled with the applied electric. Additional body forces are added to the Navier-Stokes equations for considering the surface tension and electric stress.

To describe the evolution of the droplet shape, the Level Set Method [35], suitable for free boundary problems, is applied. In this method, the interface is considered to have a finite thickness of the same order as the mesh size instead of zero thickness. The physical

properties of both media change smoothly from the value on one side of the interface to the value on the other side in the interfacial transitional zone.

The electric forces cause the droplet deformation and they can be calculated from the electric field distribution, which depends on the position and shape of the droplet. Assuming that the fluids are incompressible, the electric stress can be calculated by taking the divergence of the Maxwell stress tensor, which couples electrostatic and hydrodynamic phenomena. COMSOL [36], commercial software implementing the Finite Element Method, was used for solving the above equations.

As the droplet oscillation is more prominent in the width rather than the height of the droplet, in order to quantify the degree of the deformation of the water droplet, the width of the droplet ( $W$ ) in a  $Z$ - $X$  plane passing through the center of the computational domain has been considered (Figure 5.2).

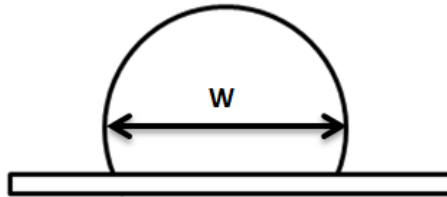


Figure 5.2 Definition of the droplet width ( $W$ )

The aspect ratio ( $A$ ) of the droplet can be defined using the initial width of the spherical cap ( $W_0$ ):

$$A = \frac{W}{W_0}$$

Without any external effects the droplet shape is controlled by the surface tension and is a section of a sphere. The volume of such a droplet depends on the radius and contact angle, and is given by

$$v(R, \theta) = \pi R^3 \left( \frac{2}{3} - \frac{3 \cos \theta}{4} + \frac{\cos 3\theta}{12} \right) \quad (5.3)$$

### 5.3 Numerical results and discussion

A series of 3-D simulations of droplet oscillation under the effect of the rotating electric field on different hydrophobic surfaces with different contact angles were performed for the following parameters: the densities  $\rho_{water} = 1000 \text{ Kg/m}^3$ ,  $\rho_{air} = 1.25 \text{ Kg/m}^3$ , viscosities  $\mu_{water} = 1 \times 10^{-3} \text{ Pa} \cdot \text{s}$ ,  $\mu_{air} = 1.82 \times 10^{-5} \text{ Pa} \cdot \text{s}$ , surface tension  $\sigma = 7.2 \times 10^{-2} \text{ N/m}$ , relative permittivity of air  $\epsilon_{air} = 1$ , gravity  $9.8 \text{ m/s}^2$ . A single water droplet with a volume of  $10 \text{ }\mu\text{l}$  was assumed in all cases. In order to keep the volume of the droplet constant (Eq. (5.3)), the radius of the droplet has to decrease with the increasing contact angle.

The first set of simulations calculates the transient response of a sessile droplet in order to investigate the effect of the rotating AC frequency and also to identify the frequency that causes the maximum deformation. Subsequently, different hydrophobic surfaces were considered and the effect of contact angle on the droplet deformation was simulated. It was assumed that the droplet phase is a perfect conductor and the ambient fluid is a perfect insulator. The droplet initial shape is perfectly matched with the assigned boundary condition on the bottom surface to exclude any unwanted transient oscillations - without electric forces the droplet would remain stationary.

The simulations were initialized by suddenly applying two phase of sinusoidal electric potentials to the electrodes. When an initially spherical liquid droplet is exposed to an external time-varying electric field it deforms with a time-dependent shape and orientation. As the electrical forces are proportional to the square of the applied voltage, one cycle of the applied signal produces two cycles of droplet oscillation. The speed and the direction of the oscillation are consistent with the rotating field. Systematic simulations were conducted over a frequency range of 10–90 Hz. Depending on the contact angle, a water droplet is significantly deformed only at a particular frequency range of the rotating AC electric field. It was found that for a surface with the contact angle of  $100^\circ$ , the water droplet deformation is very pronounced for the frequencies of

the electric field close to 35-Hz. Figure 5.3 shows the top view snapshots of the numerical results for  $\theta = 100^\circ$ ,  $f = 35$  Hz and actuation voltage of  $V_{max} = 2$  kV. It is clear that the droplet apparently rotates clockwise, while it has been elongated.

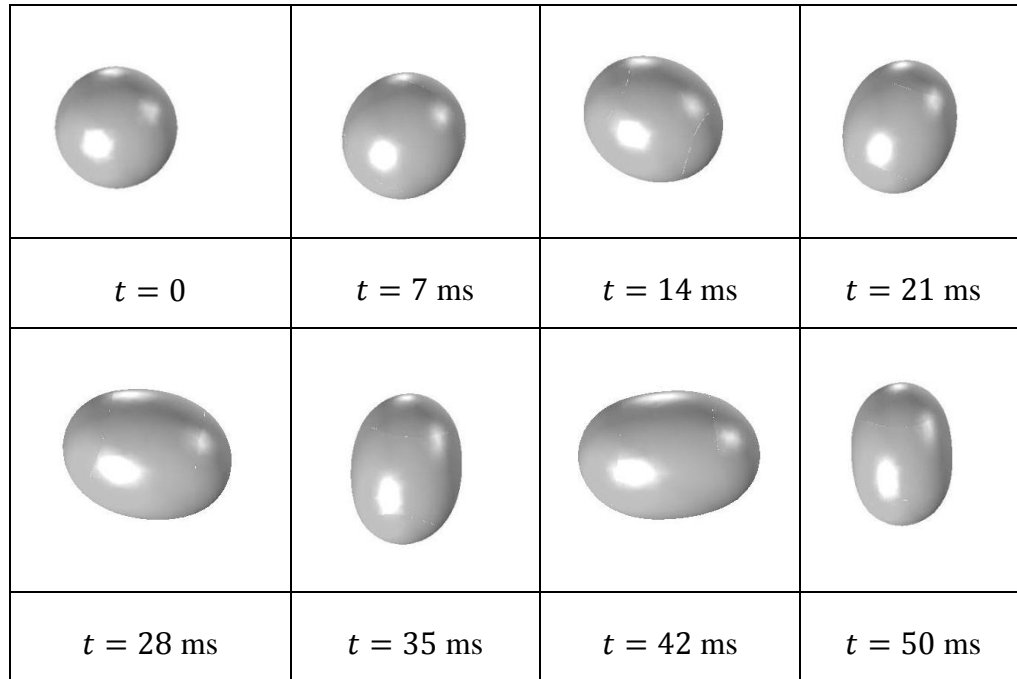


Figure 5.3 Top view snapshots of the numerical results for a rotating droplet for  $\theta=100^\circ$  and  $f=35$  Hz

### 5.3.1 Droplet oscillation

The numerically determined response of the droplet to different actuation frequencies for a  $10 \mu\text{l}$  water droplet and for the frequency intervals of 5 Hz is shown in Figure 5.4. The droplet vibrates strongly at  $f = 35$  Hz. This phenomenon could be regarded as resonance of the water droplet and happens when the frequency of the driving electric force matches with the natural frequency of the oscillating droplet. We note that, for the case of the rotating electric field, excitation frequencies are equal to twice the frequency of the AC voltage applied between the electrodes because of the quadratic dependence of the droplet deformation on the field strength.



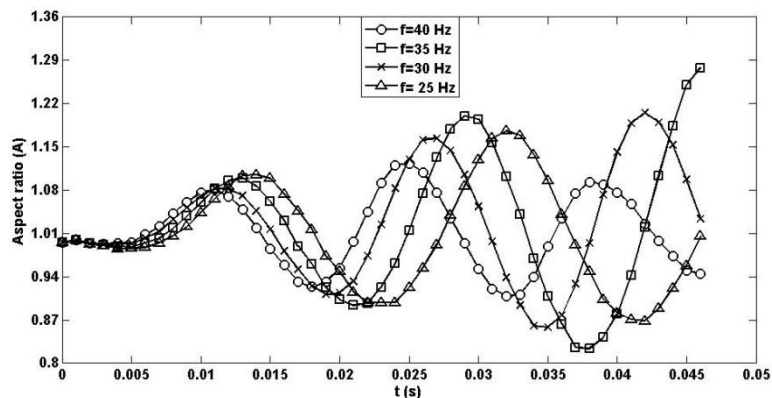


Figure 5.4 Droplet aspect ratio ( $A$ ) as a function of the time for different frequencies of electric field and contact angle  $\theta=100^\circ$

To study the effect of the surface contact angle on the frequency-dependent oscillations, the numerical simulation was also conducted for different surface contact angles. Figure 5.5 illustrates the time deformation of a 10  $\mu\text{L}$  water droplet deposited on the surface with the contact angle of  $130^\circ$ .

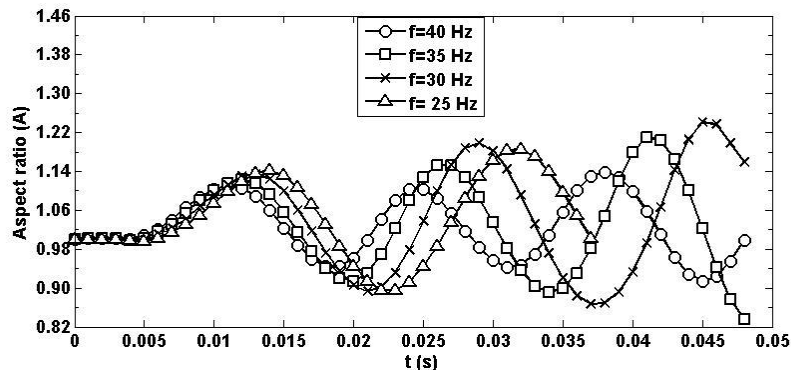


Figure 5.5 Droplet aspect ratio ( $A$ ) as a function of the time for different frequencies of electric field and contact angle  $\theta=130^\circ$

It may be observed that by increasing the contact angle, the resonance frequency is decreasing. This was also reported previously in our recent paper [33] that the resonance frequency of the water droplet deposited on a hydrophobic surface increases with a decreasing contact angle for a droplet placed in an AC voltage. Although the change in resonance frequency is not large, it agrees with predictions from Noblin's expression [39].

The presence of the solid boundary could introduce additional frictional interactions with a sessile drop that are not experienced by levitated droplets [37, 38]. A recent model proposed by Noblin et al. [39] offers a more intuitive interpretation of the origin of the vibrational modes of sessile droplets. The contact angle dependence of the frequency of the  $n^{\text{th}}$  vibrational mode of a sessile droplet can be expressed as:

$$f_n = \frac{\alpha\pi}{2} \left( \frac{n^3\sigma}{24m} \frac{(\cos^3\theta - 3\cos\theta + 2)}{\theta^3} \right)^{1/2} \quad (5.4)$$

where  $m$  is the mass of the droplet and  $\alpha$  is a constant in the order of unity, which accounts for the simplifying assumptions made in the application of the above formula to droplets of a finite size and to the fact that the theory of the droplets considered here uses a simplified one- dimensional approach.

Based on the above equation, for fixed values of droplet mass and surface contact angle, the resonant frequencies decrease by decreasing the surface tension according to:

$$\frac{f_{n2}}{f_{n1}} = \left( \frac{\sigma_2}{\sigma_1} \right)^{1/2} \quad (5.5)$$

The effect of the surface tension has been investigated for the case of  $\theta = 100^\circ$  and  $V_{max} = 2$  kV in Figure 5.6. It is obvious that by decreasing the surface tension to half of the actual value, not only the resonant frequency is decreasing to 25 Hz according to Eq. (5.5), but also the maximum deformation increases.

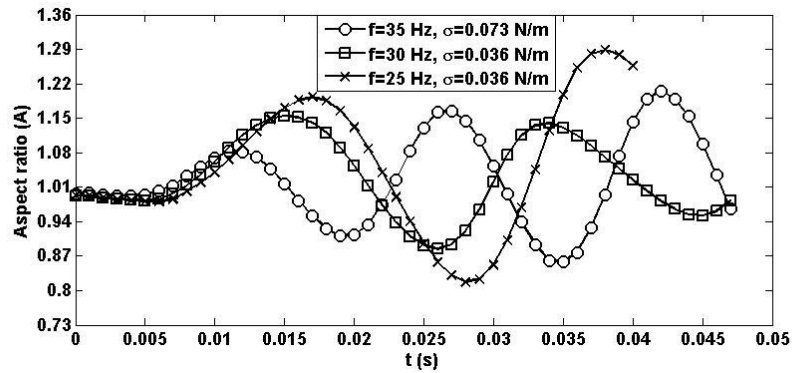


Figure 5.6 Effect of surface tension on droplet resonant frequency for  $\theta=100^\circ$

The values of  $\alpha = 1.1$  and  $n = 2$  could be used to predict the frequencies of the lowest vibrational mode of sessile droplets with different contact angles. Figure 5.7 compares the resonance frequencies obtained from our numerical results with those predicted by Eq. (5.4) for different values of  $\alpha$ .

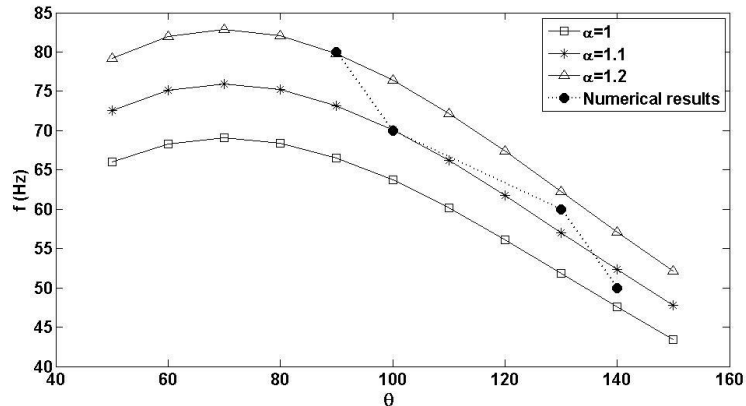


Figure 5.7 Comparison between the droplet oscillation frequency obtained from numerical simulation and Noblin's expression.

The difference may be due to the following factors: (1) the theory of the droplets considered here uses a simplified one-dimensional approach; (2) the three phase contact line is assumed to remain fixed during vibration and the resonance frequency may be shifted due to contact line friction. Frequencies are shown to be well estimated by Noblin's expression.

### 5.3.2 Droplet pseudo-rotation

In this section the internal flow generated within the droplet due to motion of the contact line and droplet deformation is investigated.

If one just follows the snapshots of the droplet shapes, it seems that the droplet is rotating around an axis passing through the center. By looking into the vectors of velocity (Figure 5.8) in a plane parallel to the bottom wall, it was found that actually there is no rotation of fluid inside the droplet. It is the periodic deformation that looks like rotating droplet from the outside and the direction of the velocity depends on the direction of the deformation in the X-Y plane.

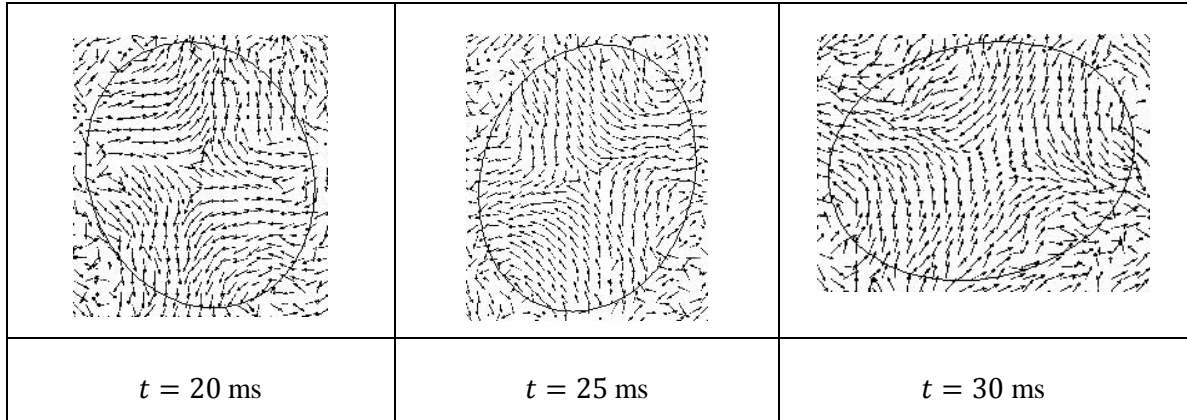


Figure 5.8 Fluid velocity vectors inside the droplet for  $\theta=100^\circ$  and  $f=25 \text{ Hz}$

The results are shown after the first cycle of the droplet oscillation to neglect transients during the initiation of droplet motion.

### 5.3.3 Coalescence of two droplets

In this section, the coalescence of two identical droplets placed on a hydrophobic surface under the effect of the rotating electric field is reported (Figure 5.9). The conducting drops are assumed to be electrically neutral. The coalescence, which in most cases would not occur naturally without applied electric field, is promoted by the induced attractive electrical force. Various coalescence regimes occur depending on the frequency of the electric field. Close to the droplet resonant frequency, the droplets can actually touch each other because of the high deformation (regime1). At other frequencies, the closest facing parts of the interfaces are attracted together because of the opposite polarity induced surface charges, that eventually lead to coalescence (regime2).

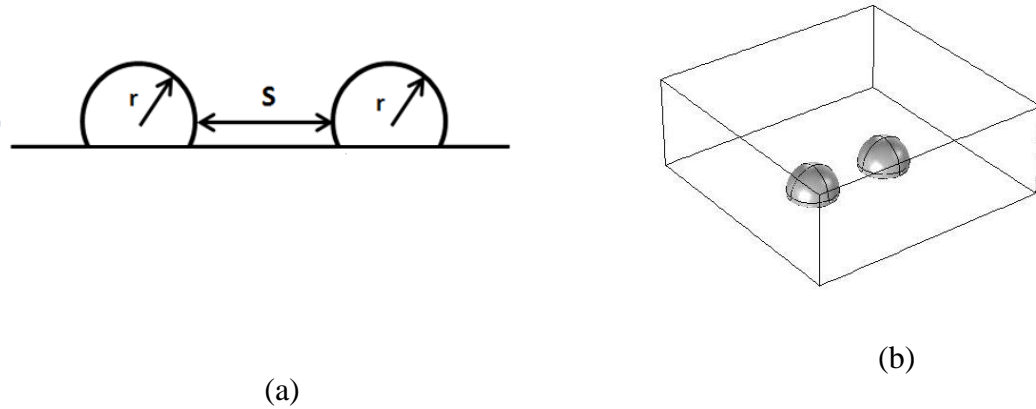


Figure 5.9 Schematic of two liquid droplets placed on a solid substrate subjected to rotating electric field. (a) Droplets position, (b) 3-D model.

$d = \frac{S}{r}$  is the normalized edge-to-edge droplet separation.  $S$  and  $r$  are the edge-to-edge droplet distance and initial radius of the droplets, respectively. The applied AC frequency ( $f$ ) can also be non-dimensionalized by the natural resonant frequency ( $f_r$ ) for different surface contact angles:

$$\bar{f} = \frac{f}{f_r} \quad (5.6)$$

The electric capillary number ( $Ca_E$ ) describes the relative strength of the electric force with respect to the capillary interfacial force

$$Ca_E = \frac{a\epsilon_{ex}E^2}{\sigma} \quad (5.7)$$

where  $E$  is the applied electric field intensity,  $\epsilon_{ex}$  is the permittivity of the ambient fluid and  $a$  is the volume-averaged radius of the droplet.

The first coalescence regime for a 10  $\mu\text{L}$  water droplet deposited on the surface with the contact angle of  $100^\circ$  is illustrated in Figure 5.10. The resonant frequency of  $f_r = 35$  was found for this configuration (Figure 5.4). The normalized edge-to-edge droplet separation and frequency are  $d = 1.3$  mm and  $\bar{f} = 1$ , respectively. In the frequency range of  $0.86 < \bar{f} < 1.14$ , the droplets are mixed because of the high deformation that makes the droplets actually touch each other.

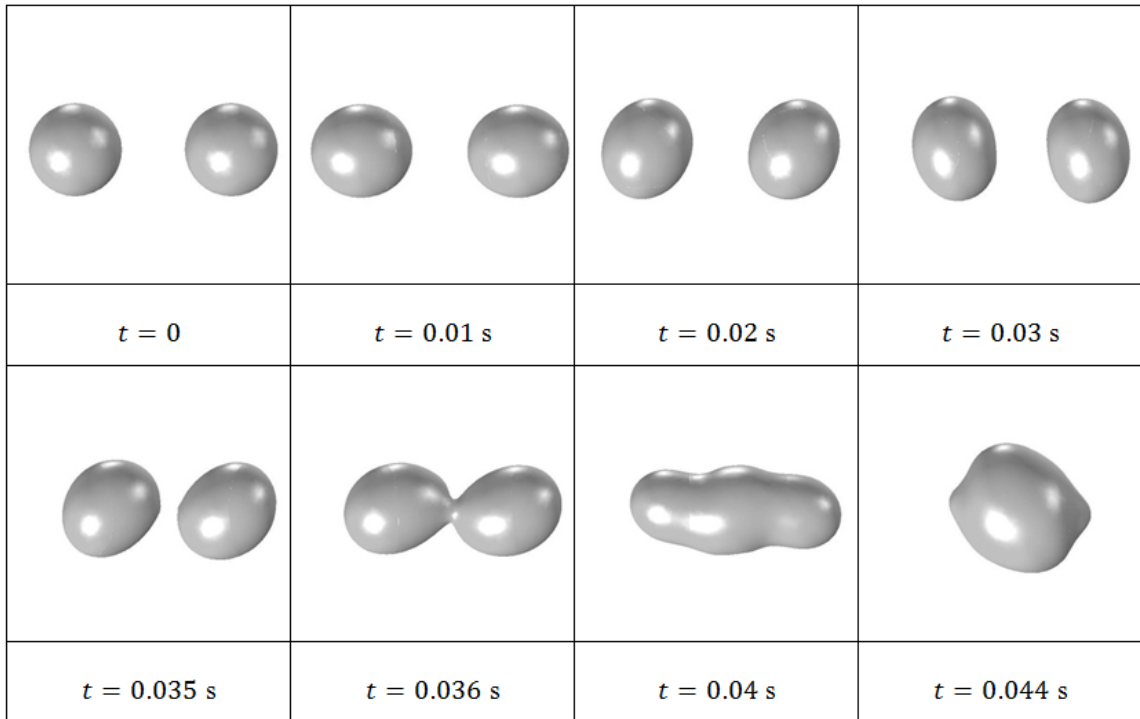


Figure 5.10 Time evolution of the first coalescence regime for  $\theta=100^\circ$ ,  $\bar{f} = 1$  and  $Ca_E=0.016$

A few randomly selected frames of the second coalescence regime for  $\bar{f} = 1.66$  are shown in Figure 5.11. By applying frequencies which are far from the resonant frequency ( $\bar{f} \leq 0.86$  or  $\bar{f} \geq 1.14$ ), the mechanism causing the coalescence becomes different. Here, the deformation is not large enough and the droplets cannot touch each other. In this mode, the droplets are pulled together because of the electrically induced dipole force between the droplets. Charges induced on the water drops will cause them to attract each other. It is clear from Figure 5.11 that after  $t = 0.03$  s, the distance between

the droplets is decreasing. At  $t = 0.037$  s, sharp deformations are created on the surface of the droplets which leads to coalescence of the droplets.

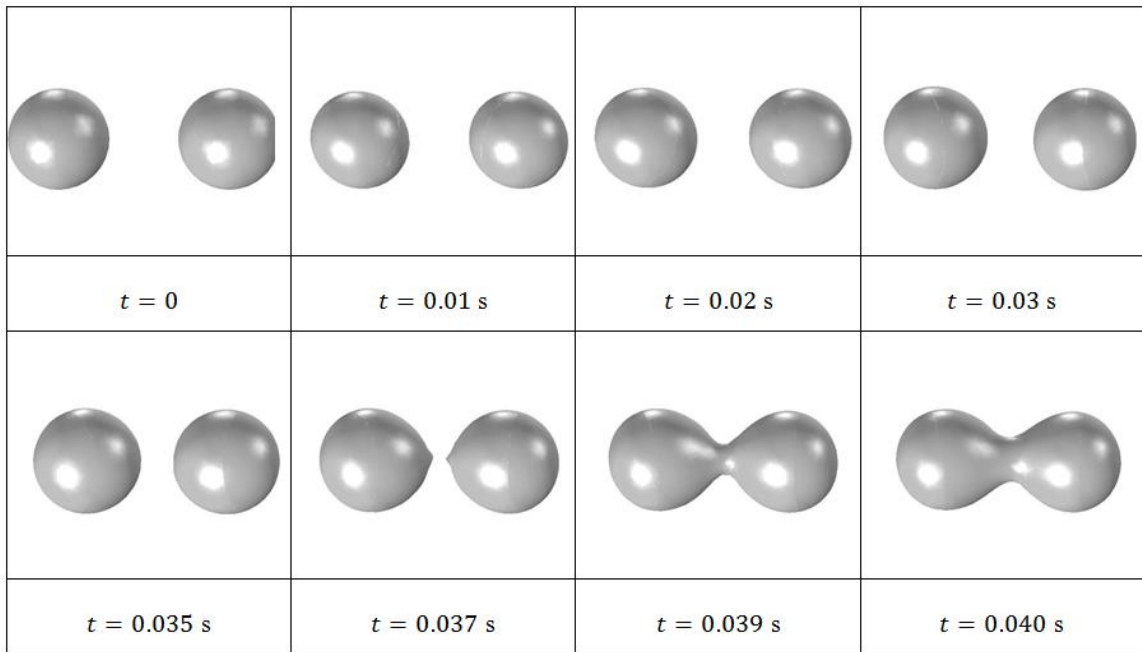


Figure 5.11 Time evolution of droplet shapes in the second coalescence regime for  $\theta=100^\circ$ ,  $\bar{f} = 1.66$  and  $Ca_E=0.016$

The second coalescence regime is similar to the experimental study of Eow and Ghadiri [40], where a high voltage DC potential was used. The two drops were observed to approach each other. When the two drops became very close together, drop-drop coalescence occurred.

Figure 5.12 is a diagram in the  $(\bar{f}, Ca_E)$  - space showing the different coalescence behaviors of the droplets as predicted by our numerical simulations. In this graph, the dashed lines are the boundaries that separate the two mixing regimes. The space between the lines refers to the first coalescence regime while the outer region represents the second coalescence regime. By increasing the electric capillary number ( $Ca_E$ ), the first mixing regime starts at lower frequencies due to the shifting of the resonant frequency to a lower value.

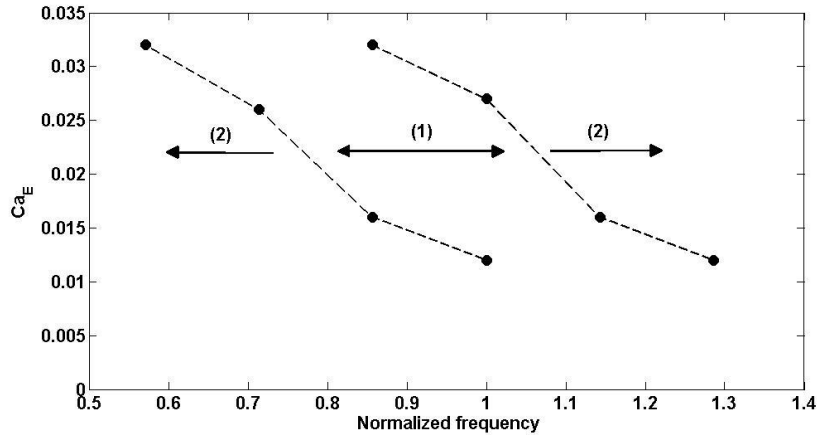


Figure 5.12  $(\bar{f}, Ca_E)$  diagram for  $\theta=100^\circ$ . The dashed lines correspond to the boundaries between two coalescence regimes.

It is well-known that the resonant frequency decreases by increasing the contact angle. The frequencies can be normalized with the new resonant frequency of  $f_r = 30$  for  $\theta = 130^\circ$ . Using the same procedure, the  $(\bar{f}, Ca_E)$  – space were obtained for the increased contact angles (Figure 5.13).

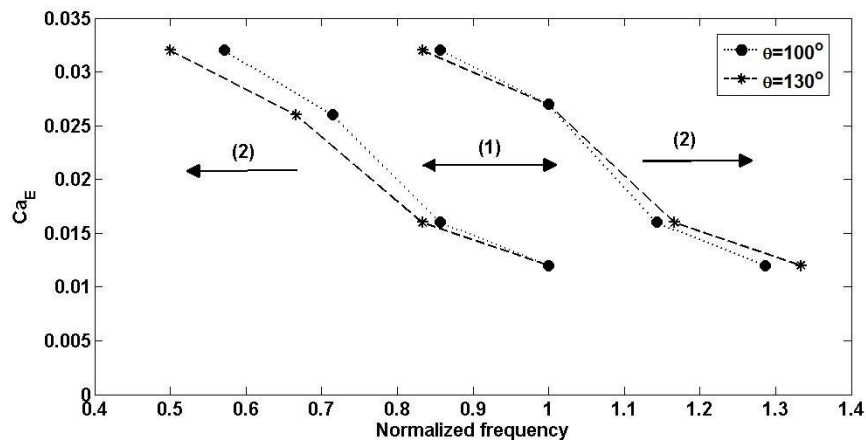


Figure 5.13  $(\bar{f}, Ca_E)$  diagram for two different contact angles ( $\theta=130^\circ$  and  $\theta=100^\circ$ ). The lines correspond to the boundaries between two coalescence regimes.

By increasing the normalized edge-to-edge droplet separation ( $d$ ), the first coalescence regime happens in a narrower band of frequencies. It can be deduced that the deformation



due to the narrower range of frequency (closer to the resonant frequency) would be sufficient for the close facing parts of the droplet interfaces to touch each other.

## 5.4 Experimental confirmation

The behavior of a single water droplet was also investigated experimentally to prove the existence of this type of pseudo-rotation. Two pairs of brass cylindrical electrodes with a diameter of 10 mm, 15mm high and with a hemispherical cap were placed to form an orthogonal electric field (Figure 5.14). The rounded electrodes were used to avoid unnecessary corona discharge.

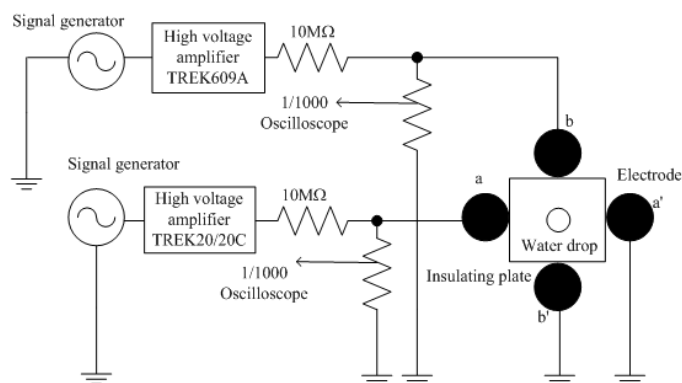
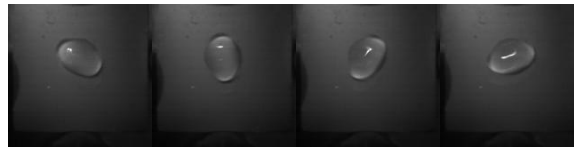


Figure 5.14 Experimental set up for producing the rotating electric field.

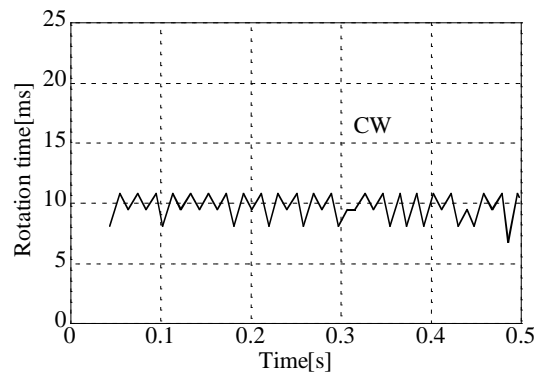
The distance between the electrodes was set at 15 mm. The set of the electrodes and the sheet were fixed on a plexi-glass plate. A hydrophobic insulating silicone rubber (SR) sheet was placed on the plate. Initially a single de-ionized water droplet with a conductivity of  $230 \frac{\mu\text{S}}{\text{m}}$  was gently placed on the SR sheet at the center between the parallel rod electrodes by a micropipette.

To produce the pseudo-rotation of a water droplet, a two phase sinusoidal high voltage of 26 Hz generated by two high voltage amplifiers (Trek Inc., 609A-3 and 20/20C) was applied to the electrodes. The pseudo-rotational motion of the water droplet was captured with a high-speed video camera (Photoron Co, Ultima SE) with a speed of 750 frames/s. Figure 5.15(a) shows the appearance of a 30  $\mu\text{l}$  water droplet under the influence of the

rotating electric field on the SR sheet with an applied voltage of 7.5 kV and a frequency of 26 Hz. This corresponds to the resonance frequency of a 30  $\mu\text{l}$  water droplet [33]. The water droplet elongates in shape and undergoes pseudo-rotation clockwise. Figure 5.15(b) shows the time variation of the time to rotate every quarter of one revolution measured from the high-speed pictures. The time to rotate each quarter revolution takes 8 to 10.5 ms. On average, it was found that it takes approximately 38.5 ms for one full revolution which coincides with the length of one period of a 26 Hz sinusoidal signal.



(a) Shape of a water droplet during pseudo-rotational motion



(b) Time to rotate a droplet for 90 degrees angle.

Figure 5.15 Clockwise pseudo-rotational motion of a droplet for  $f=26$  Hz

#### 5.4.1 Mixing of two droplets

The pseudo-rotational motion of the droplet plays an important role to stir the liquid. To confirm the stirring or mixing ability of small amount of liquid by the rotating field, a water droplet dyed with indigo carmine and another droplet of ion-exchanged water was mixed. Two droplets with a volume of 15  $\mu\text{l}$  were placed at the center region separately and resonant frequency of 26 Hz for 30  $\mu\text{l}$  was applied to the electrodes.

Figure 5.16 shows typical examples of high-speed pictures demonstrating the coalescence of two droplets taken with the speed of 4500 fps. When the two-phase voltage was applied to the orthogonal electrode pairs, the two droplets coalesced due to deformation of their shape (first coalescence regime), then the coalescent droplet started to pseudo-rotate. During these revolutions, the dyed and clear droplets were stirred and mixed gradually. After two seconds later, two droplets were completely mixed. The time to have uniform color of indigo carmine was defined as the mixing time.

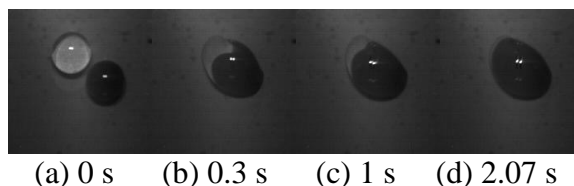


Figure 5.16 Mixing of two droplets with ion-exchanged water and indigo carmin dyed water.

To confirm the mixing performance of liquid of different viscosity by this method, the viscosity of a water droplet was adjusted by adding a concentration of starch syrup  $C_{12}H_{22}O_{11}$  in the water. The change of concentration of starch syrup from 10 to 60% corresponds to viscosity ranging from 1.7 to 27.7  $mPa \cdot s$  at 25 degree C, while that of ion-exchanged water is 0.86  $mPa \cdot s$ . It is obvious from Figure 5.17 that the mixing time increases with increased viscosity. The viscosity for a concentration of 70% of starch syrup is increased drastically to 83  $mPa \cdot s$ . The mixing time of the droplet with the viscosity of 83  $mPa \cdot s$  was about 60 s. Although two droplets of ion-changed water and water dyed by indigo carmine will finally mix by diffusion sooner or later, but without pseudo-rotational motion, the mixing time was considerably longer.

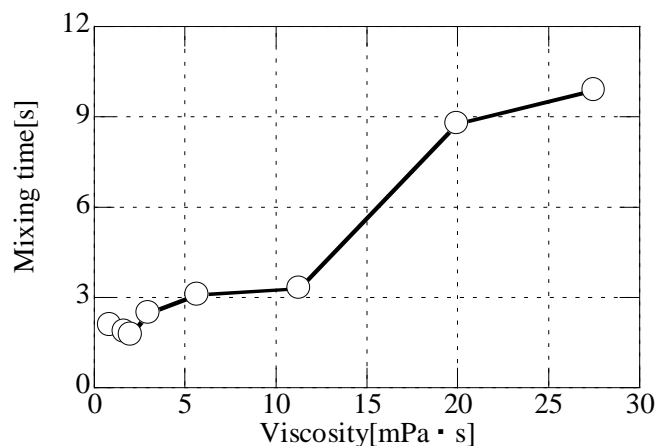


Figure 5.17 Mixing time of two water droplets containing starch syrup to vary the viscosity.

## 5.5 Conclusions

The effect of an electric field on oscillations of viscous droplets placed on hydrophobic surfaces has been studied here. The numerical approach is based on solving the classical Navier–Stokes equations for the fluid motion and the level set technique for the evolution of the fluid–fluid interface. The Maxwell stress tensor is employed to incorporate the interfacial stresses generated by the electric field into the momentum equations as volumetric source terms. The droplet seems to rotate with a rotational speed consistent with the frequency of applied AC voltage, but the fluid inside droplet is not rotating.

Two different coalescence regimes for two identical droplets placed on an insulating surface were found. Close to the resonant frequency, the droplet can be mixed by actually touching each other and far from this frequency the induced dipole attracts the droplets together.

It was also confirmed experimentally that the presented algorithm can reproduce droplet oscillations on a surface considering different contact angles. Our numerical results indicate that the resonant frequency of the water droplet depends on the surface property of the hydrophobic materials and the electrostatic force. It was also shown that the frequencies are well estimated by Noblin’s expression.

## References

- [1] M. G. Pollack, A. D. Shenderov, R. B. Fair, "Electrowetting-based actuation of droplets for integrated microfluidics", *Lab on a Chip*, vol. 2, no. 2, pp. 96-101, 2002.
- [2] D. Chatterjee, B. Hetayothin, A. R. Wheeler, D. J. King and R. L. Garrell, "Droplet-based microfluidics with nonaqueous solvents and solutions", *Lab on a Chip*, vol. 6, no. 2, pp. 199-206, 2006.
- [3] N. Kumari, V. Bahadur and S. V. Garimella, "Electrical actuation of electrically conducting and insulating droplets using AC and DC voltages", *J. Micromech. Microeng.*, vol. 18, pp. 105015 (10pp), 2008.
- [4] A. A. Darhuber and S. M. Troian, "Principles of microfluidic actuation by modulation of surface stresses", *Ann. Rev. Fluid Mech.*, vol. 37, pp. 425-455, 2005.
- [5] G. Lippmann, "Relations entre les phénomènes électriques et capillaires", *Ann. Chim. Phys.*, vol. 5, pp. 494-549, 1875.
- [6] F. Mugele and J. C. Bare, "Electrowetting: from basics to applications", *J. Phys.: Condens. Matter*, vol. 17, no. 28, pp. 705-774, 2005.
- [7] C. Quilliet, B. Berge, "Electrowetting: a recent outbreak", *Curr. Opin. Colloid Interface Sci.*, vol. 6, no. 1, pp. 34-39, 2001.
- [8] Y. Higashiyama, S. Yanase and T. Sugimoto, "Behavior of water droplet located on a hydrophobic insulating sheet under DC field", *Proc. of the IEEE IAS Annual Meeting, St. Louis, USA*, pp. 1808-1813, 1998.
- [9] T. Yamada, T. Sugimoto, Y. Higashiyama, M. Takeishi and T. Aoki, "Resonance phenomena of a single water droplet located on a hydrophobic sheet under AC electric field", *IEEE Trans. on Ind. Appl.*, vol. 39, no. 1, pp. 59-65, 2003.
- [10] Y. Higashiyama, T. Yamada and T. Sugimoto, "Vibration of water droplet located on a hydrophobic sheet under AC field", *Proc. IEEE, IAS Annual Meeting, Phoenix, Arizona*, vol. 3, pp. 1825-1830, 1999.
- [11] Y. Higashiyama, T. Takada and T. Sugimoto, "Resonant vibration and flashover phenomena of a water droplet located on a hydrophobic sheet under AC field", *J. of Electrostat.*, vol. 63, no. 6, pp. 883-889, 2005.

- [12] C. G. Cooney, C. Y. Chen, M. R. Emerling, A. Nadim and J. D. Sterling, "Electrowetting droplet microfluidics on a single planar surface", *Microfluid. Nanofluid.*, vol. 2, pp. 435-46, 2006.
- [13] T. B. Jones, "Liquid dielectrophoresis on the microscale", *J. Electrostat.*, vol. 51 pp. 290-299, 2001.
- [14] G. G. Karady, "Flashover mechanism of non-ceramic insulators", *IEEE Trans. Dielectr. Electr. Insul.*, vol. 6, no. 5, pp. 718-723, 1999.
- [15] G. G. Karady, M. Shah and R. L. Brown, "Flashover mechanism of silicone rubber insulators used for outdoor insulation-I", *IEEE Trans. Power Deliv.*, vol. 10, no. 4, pp. 1965-1971, 1995.
- [16] M. Shah, G. G. Karady and R. L. Brown, "Flashover mechanism of silicone rubber insulators used for outdoor insulation-II", *IEEE Trans. Power Deliv.*, vol. 10, no. 4, pp. 1972-1978, 1995.
- [17] A. Krivda and D. Birtwhistle, "Breakdown between water drops on wet polymer surfaces", *IEEE Conf. on Electr. Insul. and Dielectr. Phenomena*, pp. 572-280, 2001.
- [18] F. J. Hong, D. D. Jiang and P. Cheng, "Frequency-dependent resonance and asymmetric droplet oscillation under AC electrowetting on coplanar electrodes", *J. Micromech. Microeng.*, vol. 22, pp. 085024 (9pp), 2012.
- [19] S. Dash, N. Kumari and S. V. Garimella, "Frequency-dependent transient response of an oscillating electrically actuated droplet", *J. Micromech. Microeng.*, vol. 22, 075004 (11pp), 2012.
- [20] H. Lamb, "Hydrodynamics" 6th edn, (Cambridge: Cambridge University Press), 1932.
- [21] M. F. Lai, C. P. Lee, C. N. Liao and Z. H. Wei, "Oscillation spectrums and beat phenomenon of a water droplet driven by electrowetting", *Appl. Phys. Lett.*, vol. 94, 154102 (3pp), 2009.
- [22] J. Buehrle, S. Herminghaus and F. Mugele, "Interface profiles near three-phase contact lines in electric fields", *Phys. Rev. Lett.*, vol. 91, no. 8, pp. 86101-86105, 2003.
- [23] K. Adamiak, "Capillary and electrostatic limitations to the contact angle in electrowetting-on-dielectric", *Microfluid. Nanofluid.*, vol. 2, pp. 471-480, 2006.

- [24] G. Fuhr, R. Glaser and R. Hagedorn, "Rotation of dielectrics in a rotating electric high-frequency field", *Biophys J.*, vol. 49, no. 2, pp. 395-402, 1986.
- [25] H. Ziervogel, R. Glaser, D. Schadow and S. Heymann, "Electrorotation of lymphocytes-the influence of membrane events and nucleus", *Bioscience Rep.*, vol. 6, no. 11, pp. 973-982, 1986.
- [26] Yu. Dolinsky and T. Elperin, "Rotation of the leaky dielectric particle in a rotating electric field", *Phys. Rev. Lett. E*, vol. 75, no. 2, pp. 026611, 2007.
- [27] Yu. Dolinsky and T. Elperin, "Stability of particle rotation in a rotating electric field", *Phys. Rev. Lett. E*, vol. 79, pp. 026602 (8 pp), 2009.
- [28] H. Lee, S. Yun, S. H. Ko and K. H. Kang, "An electrohydrodynamic flow in AC electrowetting", *Biomicrofluid.*, vol. 3, pp. 044113-044125, 2009.
- [29] P. García-Sánchez, A. Ramos and F. Mugele, "Electrothermally driven flows in AC electrowetting", *Phys. Rev. Lett E*, vol. 81, pp. 015303 (4 pp), 2010.
- [30] F. Mugele, A. Staicu, R. Bakker and D. Van Den Ende, "Capillary Stokes drift: a new driving mechanism for mixing in AC electrowetting", *Lab on a Chip*, vol. 11, no.12, pp. 2011-2016, 2011.
- [31] P. Paik, V. K. Pamula and R. B. Fair, "Rapid droplet mixers for digital microfluidic systems", *Lab on a Chip*, vol. 3, no. 4, pp. 253-259, 2003.
- [32] R. Miraghaie, J. D. Sterling, A. Nadim, Shape oscillation and internal mixing in sessile liquid drops using electrowetting-on-dielectric (EWOD), *Technical Proc. of the NSTI Nanotechnology Conf. and Trade Show, Boston 2 (2006)* 610-613.
- [33] O. Ghazian, K. Adamiak, G. S. P. Castle, Electric-field-induced oscillations of water droplets deposited on insulating surfaces, *J. Electrostat.* 71 (2013) 489-495.
- [34] O. Ghazian, K. Adamiak, G. S. P. Castle, Numerical simulation of electrically deformed droplets less conductive than ambient fluid, *Colloids and Surfaces A: Physicochem. Eng. Aspects* 423 (2013) 27-34.
- [35] E. Olsson, G. Kreiss, A conservative level set method for two phase flow, *J. of Computational Physics* 210 (2005) 225-246.
- [36] Comsol Multiphysics User's Guide, (COMSOL 4.2).
- [37] J. S. Sharp, D. J. Farmer, J. Kelly, Contact angle dependence of the resonant frequency of sessile water droplets, *Langmuir* 27 (2011) 9367-9371.

- [38] J. S. Sharp, Resonant properties of sessile droplets; contact angle dependence of the resonant frequency and width in glycerol/water mixtures, *Soft Matter* 8 (2012) 399-407.
- [39] X. Noblin, A. Buguin, F. Brochard-Wyart, Vibrations of sessile drops, *Eur. Phys. J. Special Topics* 166 (2009) 7-10.
- [40] J. S. Eow, M. Ghadiri, Drop-drop coalescence in an electric field: the effects of applied electric field and electrode geometry, *Colloids and Surfaces A: Physicochem. Eng. Aspects* 219 (2003) 253-279.



## Chapter 6

### 6 « Spreading and retraction control of charged dielectric droplets »

#### 6.1 Introduction

The impacting and spreading of liquid drops on solid surfaces are important processes in many applications, such as spray coating, delivery of agricultural chemicals, ink jet printing and rapid spray cooling of heated targets [1-3]. The impact of liquid droplets on solid surfaces can be categorized into spreading, recoil, rebound and splashing. At some time after the impact, the drop spreading diameter reaches a maximum and then recedes depending on the wettability of the surface. Droplet retraction starts right after the spreading phase. A recent overview of droplet impact can be found in [4-6].

In most of the existing models, the impact is controlled by contact angle  $\theta$ , impact Reynolds number  $Re = \frac{\rho D_0 U_0}{\mu}$  and Weber number  $We = \frac{\rho D_0 U_0^2}{\sigma}$ , where  $D_0$  and  $U_0$  are the initial drop diameter and impact velocity, and  $\rho$ ,  $\mu$  and  $\sigma$  are the liquid density, viscosity and surface tension, respectively. One of the most important parameters relevant to the applications mentioned earlier is the maximum spreading diameter  $D_{max}$ , which is often normalized to the original diameter of the droplet prior to impact. The non-dimensional maximum spreading diameter can be defined as follows:

$$\beta_{max} = \frac{D_{max}}{D_0}$$

Numerical simulations of droplet impact onto dry surfaces have been conducted by many researchers [7-15]. The numerical methods used in previous work can be categorized into two groups. One is based on fixed grids such as a Cartesian grid. The other uses a Finite Element Method (FEM) with moving grid [11, 13]. The Volume of Fluid (VOF) method and the Level-Set method can easily handle large deformation including topology change in the liquid interface when a fixed grid is used. Most of the existing correlations for the maximum spreading diameter have been considered in the available range of the impact parameters ( $10 < Re < 40,000$  and  $2 < We < 8000$ ) [6]. It has been shown that if the

impact Reynolds and Weber numbers are high, the value of the maximum spreading diameter is only slightly dependent on the wettability of the substrate: the change in  $\beta_{max}$  is less than 5% [16].

Different correlations for the time evolution of the spread diameter ( $\beta = \frac{D}{D_0}$ ) have also been proposed in literature [17-20]. The most recent and probably the most refined model of such type predicts the dimensionless maximum spreading diameter  $D_{max}$  of a drop impacted onto a dry substrate as a root of the dimensionless cubic equation [21]

$$(We + 12)D_{max} = 8 + D_{max}^3[3(1 - \cos\theta) + 4WeRe^{-0.5}] \quad (6.1)$$

This model predicts very well the value of the maximum spreading diameter for a wide range of impact parameters. The models of Scheller and Bousfield [22]

$$\beta_{max} = 0.61(Re^2Oh)^{0.166} \quad (6.2)$$

where  $Oh = \frac{\mu}{\sqrt{\rho D_0 \sigma}}$  is the Ohnesorge number and Roisman [23]

$$\beta_{max} = 0.87Re^{1/5} - 0.4Re^{2/5}We^{-1/2} \quad (6.3)$$

showed good predictive capability for the Newtonian drops [24]. However, the effect of wettability, defined by the contact angle  $\theta$ , has been neglected in these models.

According to German and Bertola [5], maximum spreading diameter can also be found as the real root of the following cubic equation:

$$\left[ \frac{1}{4}(1 - \cos\theta) + \psi \frac{We^{0.83}}{Re\kappa} \right] (\beta_{max})^3 - \left( \frac{We}{12} + 1 \right) (\beta_{max}) + \frac{2}{3} = 0, \quad (6.4)$$

$$\psi = 0.07We^{0.2}, \kappa = 0.45Oh^{0.05}$$

These models [5, 21, 23] are all based on the energy balance approach: the initial droplet kinetic energy and surface energy prior to an impact is compared with the final surface energy (when the droplet reaches its maximum diameter and is stationary) plus the energy dissipated in overcoming liquid viscosity that resists spreading. The rate of energy loss from viscous dissipation is considered the most difficult quantity to estimate accurately because flow velocity profiles and the degree of flow recirculation can only be approximated [5]. In order to predict the maximum spreading of the drops, the correlation of German and Bertola [5] will be used in this paper (Section 6.2).

Several experimental and theoretical studies can be found in the literature on passive retraction control of aqueous droplets on hydrophobic surfaces [25-28]. In this work a new method is proposed and it relies on the application of electrostatic forces, which affect the fluid dynamics of impacting dielectric droplets especially for controlling the receding phase. Recently, perpendicular corona discharge was applied to a liquid–vapour interface to investigate a new type of interfacial electrohydrodynamic instability, which is the so-called rose-window instability [29, 30].

The effect of the electric charge on the spreading of conducting droplets impacting on dielectric substrates has been investigated by Ryu and Lee [31]. It was found that the diameter of the electrically charged droplet at the maximum spread turned out to be larger compared to that of neutral droplet and the difference becomes larger with increased electric charge.

The effect of corona discharge on the spreading and retraction control of dielectric drops has been also experimentally investigated by Mahmoudi et al. [32, 33]. It was shown that the interaction of the surface charge density and intense electric field generates an electrical pressure and leads to a uniform axisymmetric spreading of the droplet in the radial direction. A new active method based on the same concept was proposed in [33] to control the deposition of an impacted dielectric droplet. It was demonstrated that the electrical pressure effectively suppresses the droplet retraction at voltages above the corona discharge threshold.

## 6.2 Problem statement

To the best of the author's knowledge the use of a vertical electric field to control the spreading and recoiling phases of dielectric liquid droplet has not been numerically investigated. The present work focuses on the prediction of the maximum spreading diameter of a drop impacting normally on flat, dry solid surfaces with different wettability in the presence of the external electric field and/or surface charge. The results have been compared with the available experimental data.

In the first part of the paper the effect of the vertical electric field on the forced spreading dynamics of the millimetric sized charged drop placed gently on solid surfaces will be investigated.

Subsequently, the impact of the charged droplets on solid surfaces in a wide range of Reynolds and Weber numbers will be discussed.

The formulation of the problem and description of the initial conditions have already been described elsewhere [34, 35]. In order to investigate the dynamics of droplet deformation in an electric field it is necessary to solve the Navier-Stokes equations, governing the fluid motion, as well as track the interface between both fluids. The laminar two-phase flow studied here is coupled with the applied electric field and electric charges on the interface. Additional body forces are added to the Navier-Stokes equations for considering the surface tension ( $\mathbf{F}_{st}$ ) and electric stress ( $\mathbf{F}_{es}$ ).

$$\rho \frac{\partial \mathbf{u}}{\partial t} + \rho(\mathbf{u} \cdot \nabla)\mathbf{u} = \nabla \cdot [-p\mathbf{I} + \mu(\nabla\mathbf{u} + (\nabla\mathbf{u})^T)] + \rho\mathbf{g} + \mathbf{F}_{st} + \mathbf{F}_{es} \quad (6.5)$$

$$\nabla \cdot \mathbf{u} = 0$$

where  $\mathbf{u}$  denotes fluid velocity,  $\rho$  is the fluid density,  $\mathbf{g}$  is the gravitational acceleration,  $\mu$  is the dynamic viscosity,  $\mathbf{I}$  is the 3×3 identity matrix and  $p$  is the pressure. To represent the free boundaries of the droplet, the Level-Set method has been incorporated into the simulations. In this method, instead of zero thickness the interface is considered to have a finite thickness of the same order as the mesh size. The physical properties of both media

change smoothly from the value on one side of the interface to the value on the other side in the interfacial transitional zone.

The method describes the evolution of the interface between the two fluids tracing an isopotential curve of the level set function ( $\phi$ ). In general, inside the droplet  $\phi$  equals to one ( $\phi = 1$ ) and in ambient fluid  $\phi$  equals to zero ( $\phi = 0$ ). The interface is represented by the 0.5 contour of the level set function ( $\phi = 0.5$ ). The function  $\phi$  is governed by

$$\frac{\partial \phi}{\partial t} + \nabla \cdot (\phi \mathbf{u}) = \alpha \nabla \cdot \left( \epsilon_{ls} \nabla \phi - \phi(1 - \phi) \frac{\nabla \phi}{|\nabla \phi|} \right) \quad (6.6)$$

where  $\epsilon_{ls}$  is the parameter controlling the interface thickness and  $\alpha$  is the reinitialization parameter. The density and viscosity, which are different for the droplet and air, are automatically calculated from the level set variable  $\phi$ , as well as the surface tension force. The electric forces cause the droplet deformation; therefore, the distribution of the electric field, distorted by the presence of the droplet, should be calculated first. In the absence of any time-varying magnetic field, the curl of the electric field is zero ( $\nabla \times \mathbf{E} = 0$ ) and the electric field can be expressed in terms of the electric potential  $V$ .

$$\mathbf{E} = -\nabla V \quad (6.7)$$

In a two-fluid system, assuming that the electric relaxation time is longer than the time scale of the fluid motion, the governing equation for the potential can be expressed in each medium as follows:

$$\nabla \cdot \mathbf{D} = \rho_V \quad (6.8)$$

$$\mathbf{D} = \epsilon_0 \epsilon_r \mathbf{E} \quad (6.9)$$

where  $\mathbf{D}$  is the electric displacement,  $\epsilon_0$  is the permittivity of vacuum,  $\epsilon_r$  is the relative permittivity and  $\rho_V$  is the space charge density. It is assumed that there is no space charge in the fluids except the surface charge on the interface. Assuming that the fluids are incompressible, the electric stress can be calculated by taking the divergence of the

Maxwell stress tensor, which couples electrostatic and hydrodynamic phenomena. Neglecting the effect of magnetic field, the Maxwell stress tensor can be defined as:

$$\mathbf{T}_{Mij} = \varepsilon_r \varepsilon_0 E_i E_j - \frac{1}{2} (\varepsilon_r \varepsilon_0 E^2) \delta_{ij} \quad (6.10)$$

The momentum equation is modified by inserting the electric force,  $F_{es}$ , which can be determined by calculating the divergence of the Maxwell stress tensor ( $\mathbf{T}_M$ ):

$$\mathbf{F}_{es} = \nabla \cdot \mathbf{T}_M \quad (6.11)$$

Regardless of the contact angle value, there is no solution to the Navier–Stokes equations that would simultaneously satisfy all classical boundary conditions on the free surface and the solid boundary [36, 37]. The wetted wall boundary condition is suitable for solid walls in contact with a fluid–fluid interface. For the Level-Set method, this boundary condition enforces the slip condition  $\mathbf{u} \cdot \mathbf{n}_{wall} = 0$  and adds a frictional force of the form

$$\mathbf{F}_{fr} = -\frac{\mu}{\gamma} \mathbf{u} \quad (6.12)$$

where  $\gamma$  is the slip length. The computations are performed using COMSOL V4.3 [38], which is a commercial software implementing the finite element method.

The grid is fixed in space. In order to check the effect of grid size on the numerical results, three grid sizes of 20, 40, and 100 cells per initial droplet diameter were considered. It was revealed that the calculated spreading parameters did not vary significantly if the element size is smaller than  $D_0/40$ . Therefore, all further simulations were performed using such a mesh. The total mass of the droplet is

$$M = \int \rho_{drop} \phi \, d\Omega$$

where  $d\Omega$  is the element of the volume. Because there is no production or flow of mass through the boundaries, the mass of the droplet should not change with time. A conservative form of the level set equation Eq. (6.6) has been used in this study, which results in exact conservation of the mass.

## 6.3 Results

### 6.3.1 Spreading of charged dielectric droplet using vertical electric field

In this section the effect of electric field on the forced spreading of a charged droplet will be considered. A schematic illustration of the computational domain and boundary conditions are shown in Figure 6.1. The radius and height of the cylindrical computational domains are  $4D_0$  and  $3D_0$ , respectively. A small dielectric liquid droplet is deposited on a solid conducting surface, is surrounded by air and exposed to a vertical DC electric field. This field is generated by applying a high electric potential to the top electrode (H. V. electrode), while the bottom one is grounded. The zero charge boundary condition has been assumed for the electrical side boundary condition. The interface separating the two fluids is assumed to have a constant interfacial tension. At the initial stage, the shape of the droplet is assumed to be a spherical cap and both fluids are motionless. The gravity field is assumed to act in the vertical direction.

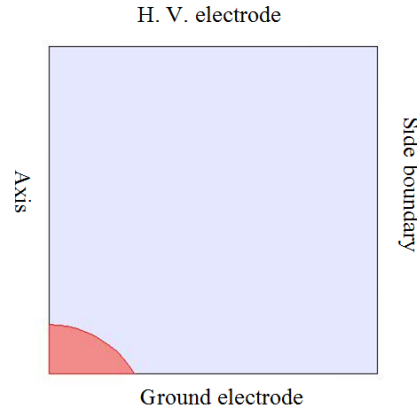


Figure 6.1 Initial configuration used in numerical computations

The volume charge was placed in the small finite interface surrounding the surface of the drop using the level-set variable distribution and is kept constant during the spreading and receding phases. The total charge ( $q$ ) can be calculated by integrating the electric charge over this interface.

The spreading of the droplet, which would not occur naturally, could be produced by applying the electric field. The maximum electric charge that a single isolated droplet can theoretically carry can be evaluated from the Rayleigh limit [39]:

$$q_{Ray} = 8\pi(\varepsilon_0\sigma r^3)^{1/2} \quad (6.13)$$

where  $\varepsilon_0$  is the vacuum permittivity, and  $\sigma$  and  $r$  are the surface tension and radius of the droplet, respectively. The simulations were performed for the following parameters:  $\rho_{drop} = 1000 \text{ kg/m}^3$ ,  $\rho_{air} = 1.2 \times 10^{-3} \text{ kg/m}^3$ ,  $\mu_{drop} = 0.05 \text{ Pa} \cdot \text{s}$ ,  $\mu_{air} = 2 \times 10^{-5} \text{ Pa} \cdot \text{s}$ ,  $\sigma = 0.022 \text{ N/m}$ ,  $D_0 = 2 \text{ mm}$  and  $E = 2.5 \times 10^6 \text{ V/m}$ . A single dielectric droplet with a volume of  $5 \text{ }\mu\text{l}$  and relative dielectric constant of 3 has been assumed in all cases. In order to keep the volume of the droplet constant, the radius of the droplet has to decrease with the increasing contact angle.

Successive snapshots of the drop shape for the spreading of droplets on a surface with the contact angle of  $\theta = 60^\circ$  are shown in Figure 6.2. Interaction of the strong electric field and the surface charges deposited on the surface of the droplet creates an electrical pressure which leads to spreading of the droplet [32].





















	$q/q_{Ray} = 0.15$	$q/q_{Ray} = 0.28$	$q/q_{Ray} = 0.55$
$t = 0$			
$t = 4$ ms			
$t = 8$ ms			
$t = 18$ ms			
$t = 28$ ms			
$t = 100$ ms			

Figure 6.2 Electrostatic spreading of a charged droplet placed on a surface ( $\theta=60^\circ$ ).

The above images show that the surface charge density is the crucial parameter affecting the maximum spreading diameter. The droplet starts to spread depending on the amount of the charge it carries. After some time, the droplets reach their maximum spreading diameter ( $t = 0.1$  s). This phenomenon has been observed experimentally and it has been found that the effect is suppressed for fluids with higher surface tension [32].

Figure 6.3 also shows the dynamic spread diameter as a function of time for different values of the surface charge density. The initial size of the deposited droplet,  $D_0$ , was evaluated by converting the droplet volume to its equivalent spherical size.

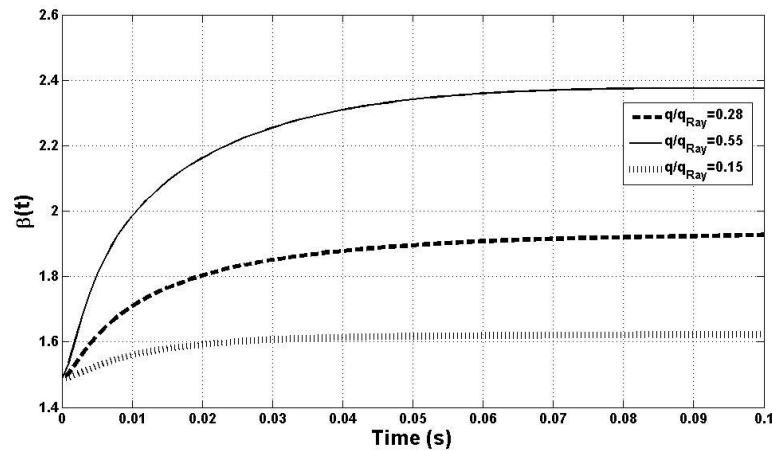


Figure 6.3 Dynamic spreading ratio of droplets with different surface charges in the presence of electric field  $E=25$  kV/cm for  $\theta=60^\circ$

### 6.3.1.1 Effect of viscosity

Changing the viscosity of the droplet does not have any major effect on the final spreading diameter but it affects the spreading rate during the initial stage. Droplets with low viscosities respond faster to the electric forces. Figure 6.4 presents the results for a droplet whose molecular viscosity is 5 times lower than the above ones, while both the electric field and charge are the same. For a less viscous droplet the viscous damping plays a smaller role and the inertial forces lead to a faster droplet spreading. This in turn produces a larger capillary force, which slightly retracts the droplets until a new balance

with electrical forces is reached. In the steady-state there is practically no effect of fluid viscosity.

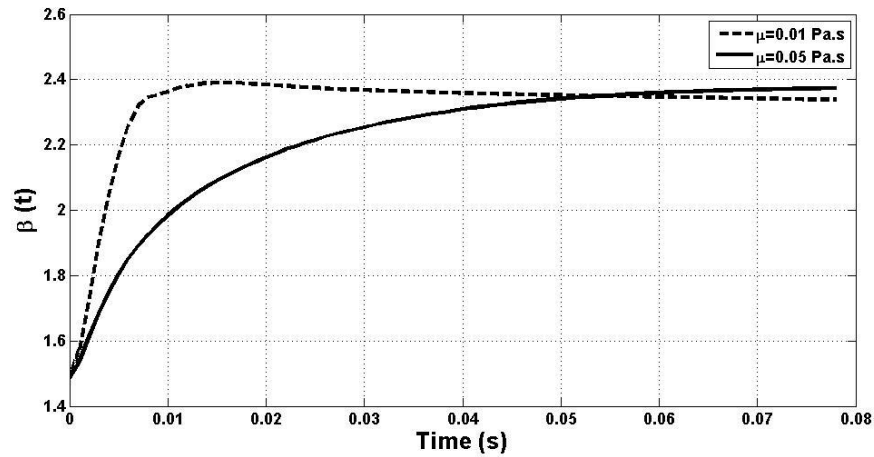


Figure 6.4 Effect of viscosity for  $q/q_{Ray}=0.55$  and  $E=25$  kV/cm

It can be concluded that both the surface charge and the electric field have effects on the maximum spreading diameter ( $\beta_{max}$ ), but the viscosity just affects the rate of spreading. The droplets with low viscosity reach to their final maximum spreading diameter faster because of the lower resistance on adjacent fluid layers due to the shear forces.

Using our numerical method, the maximum spreading diameter of the droplets with different surface charge densities can be obtained. It is suggested that this technique can be used in other fluid dynamics problems and in future research involving cooling effectiveness where the goal is to increase the area wetted by the liquid on the surfaces and the rate at which the droplets reach to the maximum wetting area.

### 6.3.2 Retraction control of the charged dielectric droplets using vertical electric field

In this model a liquid droplet having diameter  $D_0$  collides with the surface with an impact velocity  $U_0$  (Figure 6.5), which is directed normal to the wall. The simulations were performed for the following parameters:  $\rho_{drop} = 1000$  kg/m<sup>3</sup>,  $\rho_{air} = 1$  kg/m<sup>3</sup>,  $\mu_{drop} =$

$0.05 \text{ Pa} \cdot \text{s}$ ,  $\mu_{air} = 2 \times 10^{-5} \text{ Pa} \cdot \text{s}$ ,  $\sigma = 0.022 \text{ N/m}$ ,  $D_0 = 2 \text{ mm}$  and  $E = 25 \text{ kV/cm}$ . The droplet thermophysical properties have been chosen close to that of Silicone oil.

Droplet impact simulations were performed assuming surfaces with different contact angles from hydrophilic ( $\theta < 90^\circ$ ) to hydrophobic ones ( $\theta > 90^\circ$ ). In the simulations, the wetting boundary condition is applied to the bottom wall and a static contact angle model was used. For the verification of the numerical model, numerical simulations of droplet impact with the conditions identical to those in the experiments of Clanet et al. [17] were first performed.

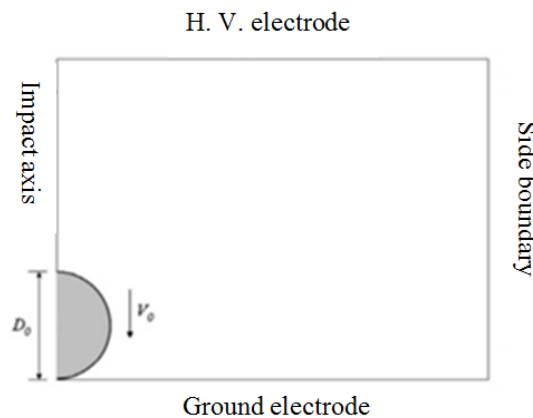


Figure 6.5 Computational domain for simulating a droplet impinging on horizontal surface

In the absence of the electric forces, the droplet hits the surface, spreads out and subsequently retracts. In Figure 6.6, the shape of the water droplet impacting on a superhydrophobic surface (the static contact angle equal to  $170^\circ$ ) is compared with the experimental study of Clanet et al. [17] for  $D_0 = 2.5 \text{ mm}$  and  $U_0 = 0.83 \text{ m/s}$ . Time interval between the pictures is  $2.7 \text{ ms}$  and  $t = 0$  shows the droplet just at impact.

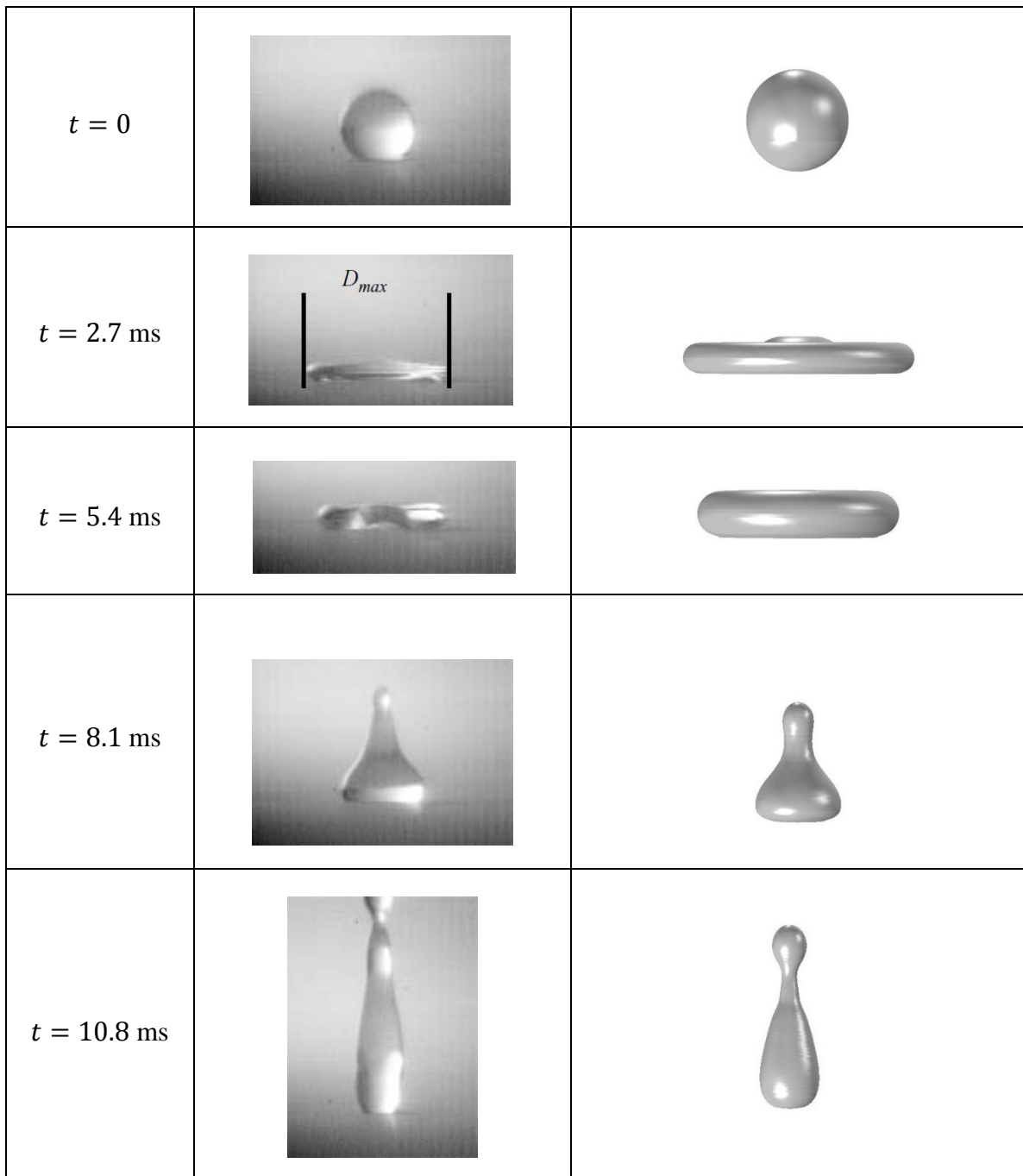


Figure 6.6 Experimental [17] (left) and simulated (right) shape of a water droplet impinging a super-hydrophobic surface

As shown in Figure 6.6, the numerically predicted droplet shape agrees very well with the results of the experiment over the considered time interval. The difference can likely be

attributed to the effect of the surface wettability and the assumption of the constant contact angle.

In Figure 6.7 the maximum diameter of the spreading droplet as a function of the Weber number is compared with the experimental study of Clanet et al [17].

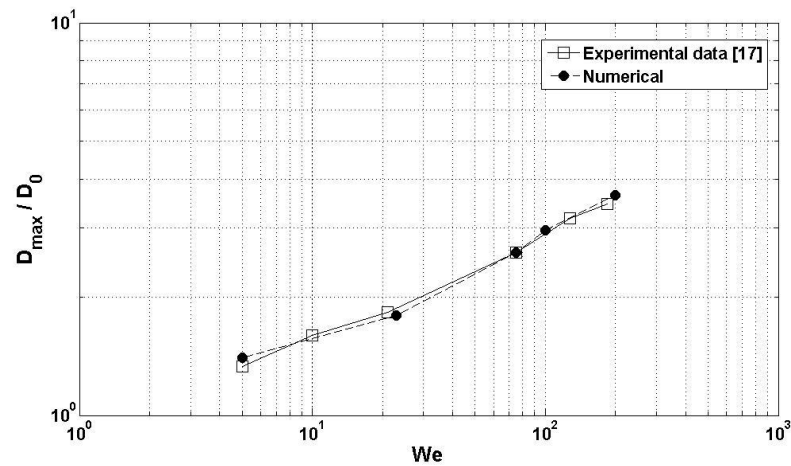


Figure 6.7 Comparison between the experimental [17] and numerical maximum spreading diameter

The numerical algorithm has been also validated by comparing with the semi-empirical model of German and Bertolla [5], in which a number of models to predict the maximum diameter were assessed and compared to experimental measurements; improved predictions were achieved by an empirical adjustment of one of the existing models [18]. Adjustments to the correlations presented by [5] were made through an iterative process of optimizing the empirically based powers of the Weber and Reynolds numbers and the empirical constant term by minimizing differences between predicted and experimental value of  $\beta_{max}$  for each Newtonian solution (prepared by dissolving glycerol in deionized water). As it can be seen from Figure 6.8, a reasonably good agreement has been achieved.

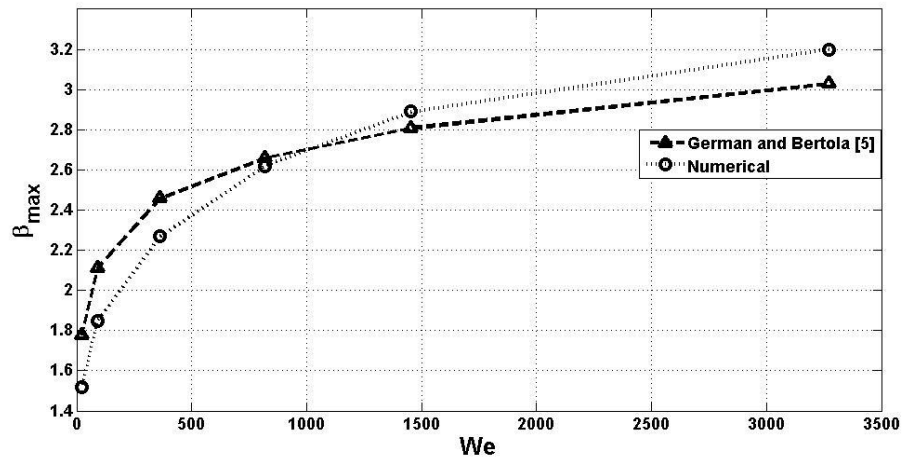


Figure 6.8 Comparison between the calculated spread diameter [5] and numerical results for the droplets impacting solid surface at different Weber numbers and the constant contact angle  $\theta = 100^\circ$

After increasing the impact velocity of the droplet, the effect of surface wettability and contact angle becomes negligible. Figure 6.9 illustrates the maximum spreading of a droplet for different contact angles and impact velocities. At lower impact velocities, the maximum spreading strongly depends on the contact angle. At higher Weber numbers, the effect of inertial force is dominant and the maximum spreading only slightly depends on the contact angle.

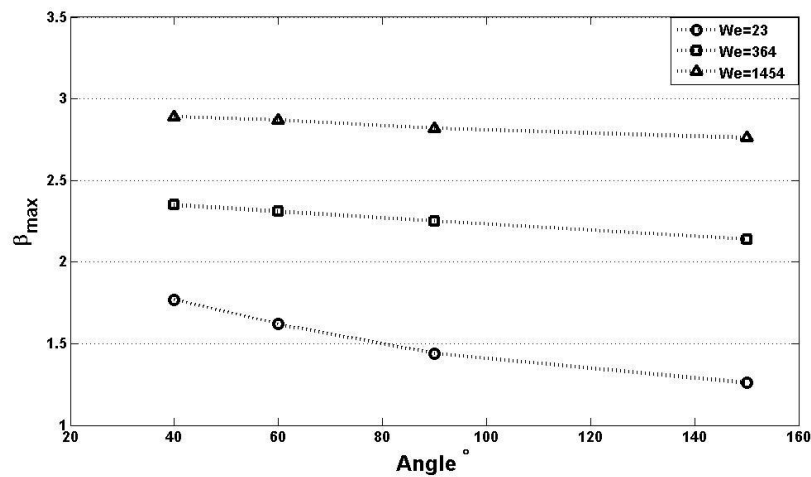


Figure 6.9 Effect of surface contact angle on the maximum droplet spreading

After a positive validation of the computational algorithm, it has been applied to simulate impacting charged droplets in the presence of an external electric field.

Figure 6.10 shows the distribution of the electric potential for a few instants of time. One can see that the electric potential lines have been dynamically distorted; as the droplet shape changes, the equipotential lines are adjusted clearly illustrating the two-way coupling in this multiphysics problem. The densely packed potential contours show the area of the high electric field.

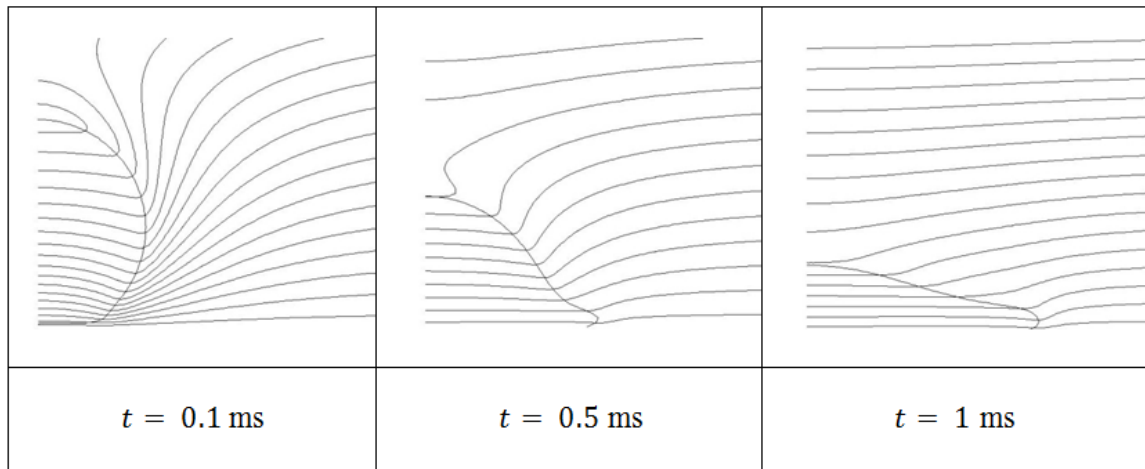




















Figure 6.10 Electric potential contour lines for different instants of time after the droplet impact

The first set of simulations was performed for the droplet with an initial diameter of 2 mm and contact angle of  $100^\circ$ ; the results are presented in Figure 6.11. The impact velocity was assumed to be  $U_0 = 2 \text{ m/s}$ , corresponding to  $We = 364$ , which was low enough so that droplets did not splash upon impact [40]. The droplet did not break up during impact since its kinetic energy was too low to overcome surface tension. In order to investigate the effect of charge density on the droplet spreading, the simulations have been performed for three different values of the total charge. The applied voltage difference was kept constant at the level of  $E=25 \text{ kV/cm}$ .



	$q/q_{Ray} = 0$	$q/q_{Ray} = 0.28$	$q/q_{Ray} = 0.80$
$t = 2 \text{ ms}$			
$t = 4 \text{ ms}$			
$t = 6 \text{ ms}$			
$t = 8 \text{ ms}$			
$t = 12 \text{ ms}$			
$t = 18 \text{ ms}$			

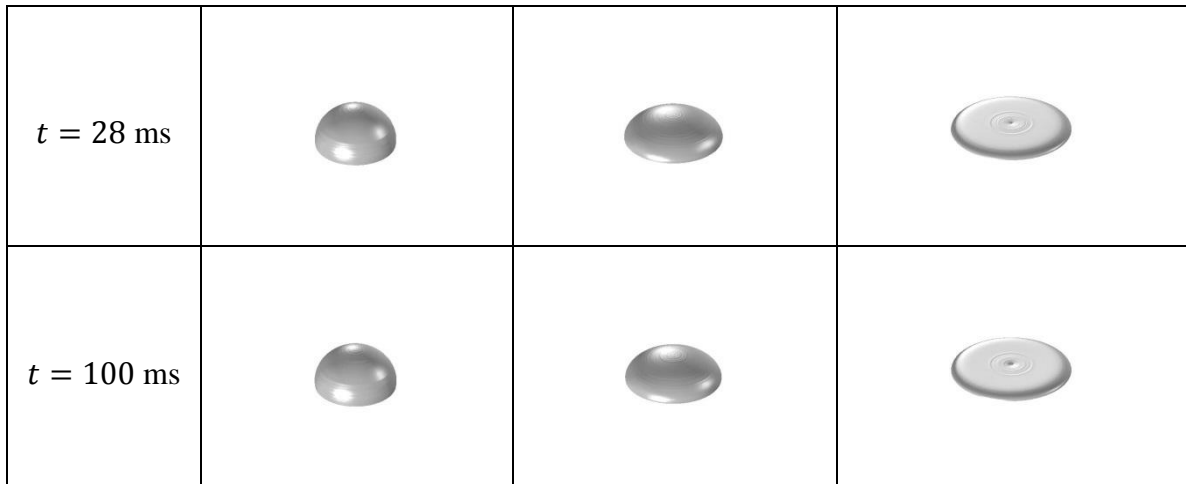


Figure 6.11 Impact of the electrically charged droplet on a surface with the contact angle of  $\theta=100^\circ$  and exposed to an external electric field  $E=25 \text{ kV/cm}$

In all cases the droplets spread to their maximum diameter and were then pulled back by surface tension. In the absence of the charge ( $q/q_{Ray} = 0$ ), the spreading stage takes place during 3 ms after the impact and is followed by retraction of the droplet, which occurs in a few tens of milliseconds after the impact. However, it can be clearly observed that the increasing surface charge acts to maintain the maximum spreading diameter. Charged droplets retracted less after the maximum spreading than those uncharged.

In the case of a high charge ( $q/q_{Ray} = 0.80$ ), the retraction can be completely eliminated after reaching the maximum diameter due to the combined effect of the surface charge and electric field. From the practical point of view, this level of charge is impossible, as any instability of the droplet surface could immediately cause droplet fission [41, 42]. However, this case has been investigated as a theoretical exercise.

For the lower value of charge ( $q/q_{Ray} = 0.28$ ) the electric force is not strong enough to maintain the maximum spreading after the impact.

Figure 6.12 illustrates dynamics of the spread diameter,  $\beta$ , as function of the time for the same charges as presented in Figure 6.11. The results show that the final wetting diameter increases as surface charge increases. Obviously, this is due to the electric forces applied on the surface of the charged droplets, which are exposed to an external electric field. It

can also be observed that the spreading phase is almost identical for three cases and the maximum spreading diameter is achieved at  $t = 0.003$  s. During the expansion stage, the inertial force is dominant, whereas for the retraction stage the inertial force is less important and the process mostly depends on capillary forces. The inertial force is larger than the electric force during the expansion stage and the inertia is the dominant force even assuming the maximum charge over the droplet interface. During the retraction stage, the primary force, which is the capillary force, is comparable with the electric force; therefore, the retraction is expected to be suppressed.

An order of magnitude analysis based on relevant dimensionless numbers [43] can be helpful to understand the results. For the expansion stage, the electro-inertial number  $N_E = \frac{\epsilon_{ex} E^2}{\rho_{drop} U_0^2} \approx 0.01$  and it can be concluded that the inertia effect in the spreading stage dominates over the electric force. During the retraction stage, the electric capillary number based on droplet maximum diameter  $Ca_E = \frac{D_{max} \epsilon_{ex} E^2}{\sigma} \approx 5$  suggesting that the retraction can be controlled using electric forces.

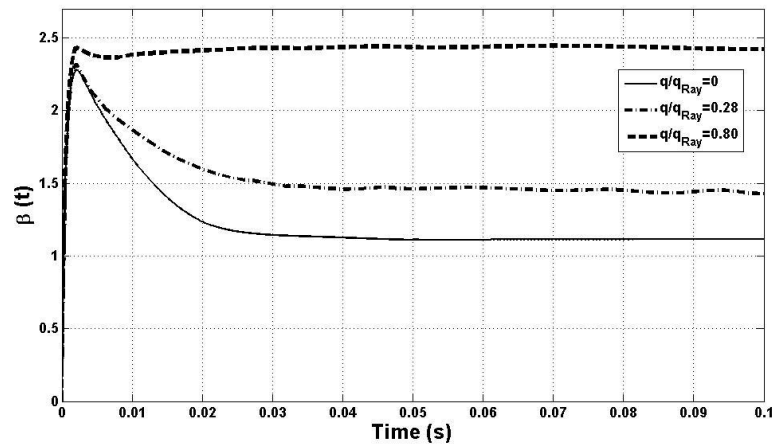


Figure 6.12 Dynamic spreading diameter droplets charged to different values in the presence of electric field  $E=25$  kV/cm for  $\theta=100^\circ$ ,  $We=364$  and  $Re=80$

Two regimes can be clearly identified in this process. For moderate charges ( $\frac{q}{q_{Ray}} < 0.8$ ) the droplet reaches the maximum spreading, but later retracts. However, by increasing the charge, the final spreading diameter gets closer to the maximum spreading. If the charge

density is high enough, ( $q/q_{Ray} \geq 0.8$ ), the droplet remains at the maximum spreading or continues to spread even more.

In order to further examine the problem, the effect of the impact velocity is considered in Figure 6.13. Comparison of the time evolution characteristics confirms that after reaching the maximum spreading diameter, there is a bit of retraction for the Weber number of 364, but in the case of  $We = 91$ , the maximum spreading diameter has been conserved.

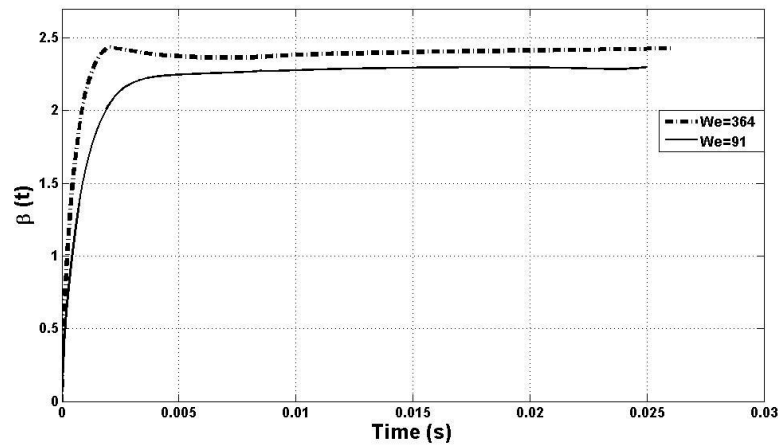



















Figure 6.13 Effect of impact velocity on the droplet spreading for  $\theta=100^\circ$  and  $q/q_{Ray}=0.8$

Although the maximum droplet spreading is slightly different, it can be conserved at its final value, if the droplet is charged to a proper level.

### 6.3.2.1 Contact angle dependence

To study the influences of the contact angle, the calculated shapes of the droplet with the same diameter and impact velocity as those in Figure 6.11, but on a surface with a smaller contact angle ( $\theta = 60^\circ$ ), at different time instants are shown in Figure 6.14. The numerical results show that the maximum spreading has been increased comparing to the case of  $\theta = 100^\circ$ .

	$q/q_{Ray} = 0$	$q/q_{Ray} = 0.28$	$q/q_{Ray} = 0.55$
$t = 2 \text{ ms}$			
$t = 4 \text{ ms}$			
$t = 6 \text{ ms}$			
$t = 8 \text{ ms}$			
$t = 12 \text{ ms}$			
$t = 18 \text{ ms}$			

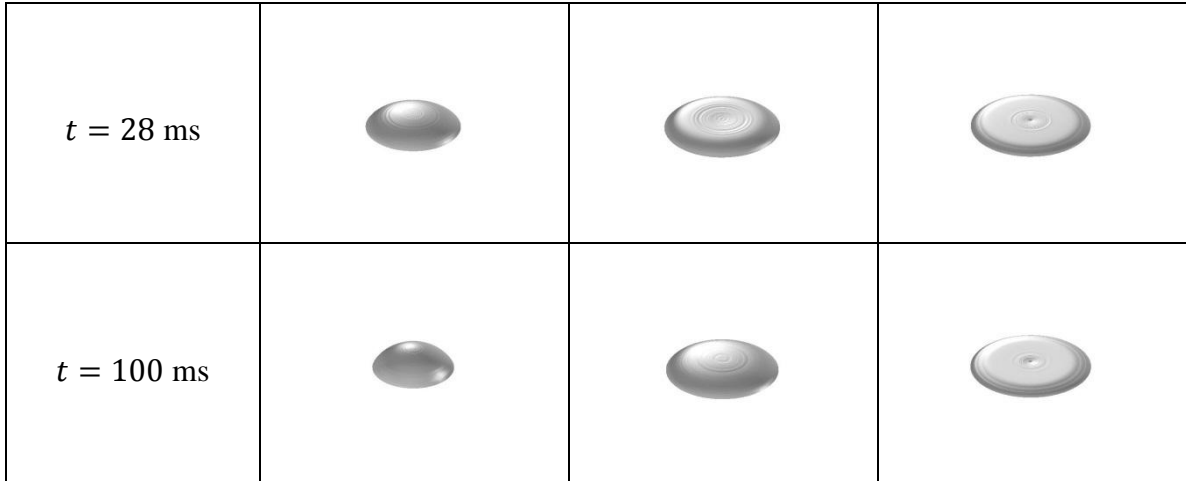


Figure 6.14 Impact of the charged droplet on a surface with the contact angle of  $\theta=60^\circ$  and  $E=25 \text{ kV/cm}$

By decreasing the wettability of the surface, the resistive force acting against the electric force during the receding phase decreases and a lower value of charge is sufficient to keep the maximum spreading diameter. The dynamic spreading diameter for  $\theta = 60^\circ$  and  $D_0 = 2 \text{ mm}$  for the impact velocity of  $U_0 = 2 \text{ m/s}$  is shown in Figure 6.15.

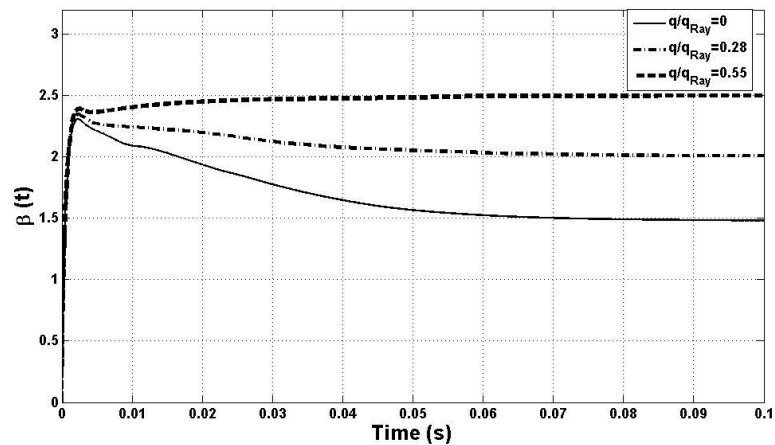


Figure 6.15 Dynamic spreading ratio of droplets with different surface charges in the presence of electric field  $E=25 \text{ kV/cm}$  for  $\theta=60^\circ$  and  $We=364$

By comparing the results for  $\theta = 100^\circ$  (Figure 6.12) and  $\theta = 60^\circ$  (Figure 6.15), one can notice that for the same droplet total charge ( $q/q_{Ray} = 0.28$ ) the final spreading

diameter increases with decreasing the contact angle, assuming the same droplet volume. In other words, in order to keep the maximum diameter after the impact, less charge is needed for the surfaces with a lower contact angle. The results of computations of the spreading diameter for different contact angles are shown in Figure 6.16.

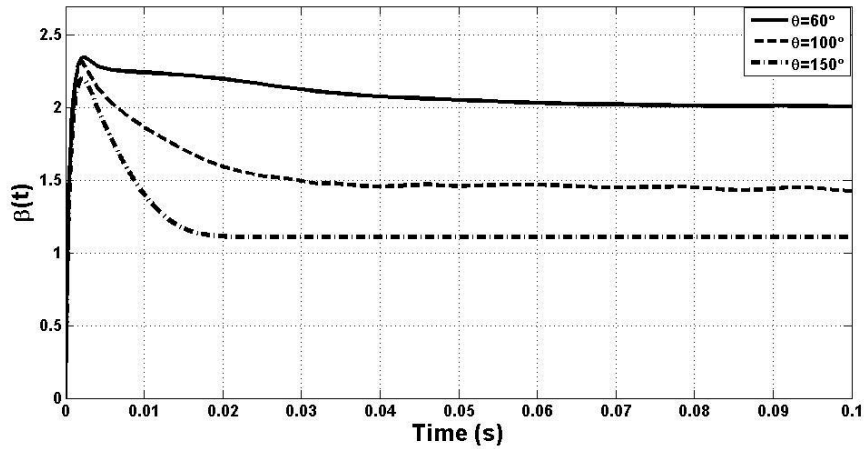














Figure 6.16 Effect of contact angle on spreading diameter for  $q/q_{Ray}=0.28$ ,  $We=364$  and  $E=25$  kV/cm

These results show that higher values of charge are required to overcome the capillary forces on the surface with larger contact angles.

Also of interest is investigating the effect of electric field intensity on droplet spreading. In Figure 6.17, the effect of electric field intensity is shown for  $\theta = 60^\circ$  and  $E = 8.3$  kV/cm. It is obvious that by decreasing the magnitude of the electric field, the electric force suppressing the retraction decreases. This can be explained considering that the electrostatic force depends on both the magnitude of the surface charge and the electric field. In order to keep the maximum diameter, one should increase the charge in lower external electric field intensities.

	$q/q_{Ray} = 0.28$	$q/q_{Ray} = 0.80$
$t = 2 \text{ ms}$		
$t = 4 \text{ ms}$		
$t = 6 \text{ ms}$		
$t = 8 \text{ ms}$		
$t = 12 \text{ ms}$		
$t = 18 \text{ ms}$		



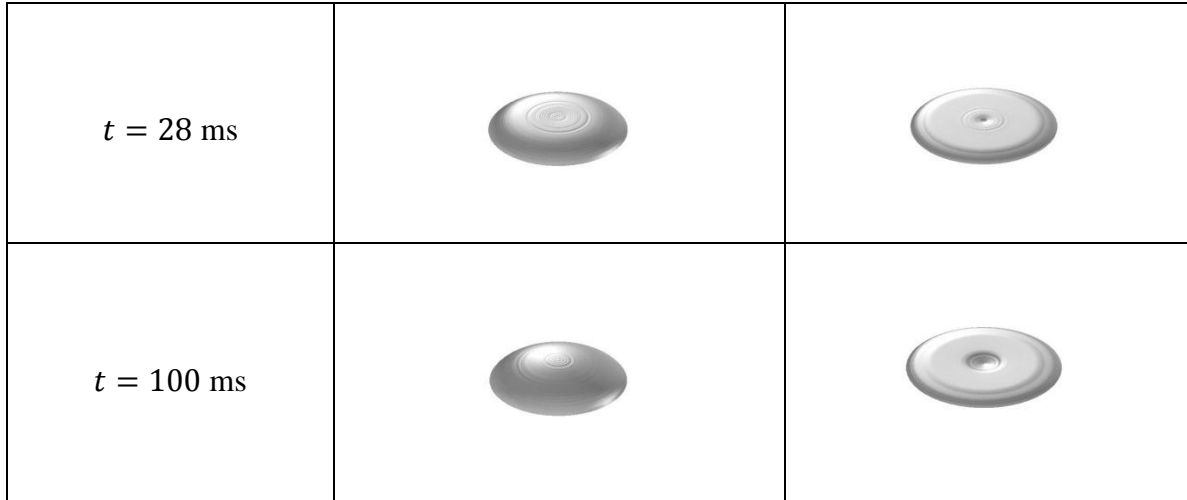


Figure 6.17 Spreading of a droplet impacting on a surface  $\theta=60^\circ$  and subjected to an electric field  $E=8.3 \text{ kV/cm}$  and  $We=364$

Comparing Figure 6.15 and Figure 6.18 it can be observed that the maximum spreading diameter has decreased with decreasing the magnitude of the applied external electric field, confirming the fact that the electrostatic force depends on both the magnitude of the surface charge and the electric field.

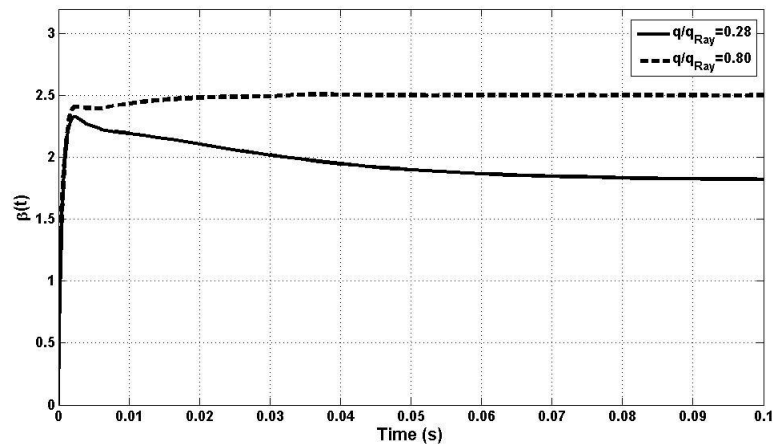


Figure 6.18 Dynamic spreading ratio of droplets with different surface charges in the presence of electric field  $E=8.3 \text{ kV/cm}$  for  $\theta=60^\circ$  and  $We=364$

For the large values of the surface tension, putting the charge even higher than the Rayleigh limit is not enough to keep the droplets from retracting. For instance, if the surface tension is strong enough (close to the surface tension of water), no inhibition is

observed but only the spreading of a droplet accompanied by the receding phase. Therefore, it can be concluded that retraction inhibition increases with increasing of the droplet charge or external electric field. Moreover, the maximum spreading diameter can be conserved using smaller value of charge on surfaces with smaller contact angles.

## 6.4 Conclusions

Spreading and retraction control of millimeter sized dielectric droplets impacting on dry surfaces have been investigated to examine the effect of the surface charge density and electric field intensity. The maximum diameter to which droplets spread can be controlled using the electric forces. To validate the numerical algorithm, the numerical results have been compared with the available theoretical and experimental studies of droplet impact. It was found that the correlation by German and Bertola [5] is the one that best predicts droplet maximum spreading diameter for the considered range of Reynolds and Weber numbers. The obtained numerical predictions for the shape of the droplet have been compared with experimental data published in the literature [17].

The effect of the surface charge on the spreading of droplets placed gently on surfaces was investigated in the first part. It was found that the maximum spreading diameter increases with an increasing charge. It was also found that lowering the viscosity will accelerate the spreading.

In the second part, the impact of a droplet on a ground electrode was considered. It was found that by increasing the charge density, it may be possible to increase the spreading without any retraction after the droplet reaches its maximum diameter. It was also found that in order to keep the maximum diameter after the impact, less charge is needed for surfaces with lower contact angle.

## References

- [1] A. Frohn and R. Roth, “Dynamics of Droplets Springer”, Berlin, 2000.
- [2] J. D. Bernardin, C. J. Stebbins and I. Mudawar, “Mapping of impact and heat transfer regimes of water drops impinging on a polished surface”, *Int. J. Heat Mass Transfer*, vol. 40, no. 2, pp. 247-267, 1997.
- [3] G. Xie, L. Luo, S. Liu, D. Guo, C. Zhang and L. Si, “Electrospreading of dielectric liquid menisci on the small scale”, *Soft Matt.*, vol. 7, no. 13, pp. 60-76, 2011.
- [4] A. L. Yarin, “Drop impact dynamics: splashing, spreading, receding, bouncing”, *Ann. Rev. Fluid Mech.*, vol. 38, pp. 159-192, 2006.
- [5] G. German and V. Bertola, “Review of drop impact models and validation with high viscosity Newtonian fluids”, *Atm. Sprays*, vol. 19, no. 8, pp. 787-807, 2009.
- [6] M. Marengo, C. Antonini, I.V. Roisman and C. Tropea, “Drop collisions with simple and complex surfaces”, *Curr. Opin. Colloid Interface Sci.*, vol. 16, no. 4, pp. 292-302, 2011.
- [7] F. H. Harlow and J. P. Shannon, “The splash of a liquid drop”, *J. Appl. Phys.*, vol. 38, pp. 3855-3866, 1967.
- [8] K. Tsurutani, M. Yao, J. Senda and H. Fujimoto, “Numerical analysis of the deformation process of a droplet impinging upon a wall”, *JSME Int. J., Ser. II*, vol. 33, pp. 555-562, 1990.
- [9] G. Trapaga and J. Szekely, “Mathematical modeling of the isothermal impingement of liquid droplets in spraying processes”, *Metall. Trans. B*, vol. 22, no. 6, pp. 901-914, 1991.
- [10] Y. D. Shikhmurzaev, “The moving contact line on a smooth solid surface”, *Int. J. Multiphase Flow*, vol. 19, no. 4, pp. 589-610, 1993.
- [11] J. Fukai, Z. Zhao, D. Poulikakos, C. M. Megaridis and O. Miyatake, “Modeling of the deformation of a liquid droplet impinging upon a flat surface”, *Phys. Fluids A*, vol. 5, no. 11, pp. 2588-2599, 1993.
- [12] A. Karl, K. Anders, M. Rieber and A. Frohn, “Deformation of liquid droplets during collisions with hot walls: Experiment and numerical results”, *Part. Part. Syst. Charact.*, vol. 13, no. 3, pp. 186-191, 1996.

- [13] M. Bertagnolli, M. Marchese, G. Jacucci, I. St. Doltsinis and S. Noelting, “Thermomechanical simulation of the splashing of ceramic droplets on a rigid substrate”, *J. Comput. Phys.*, vol. 133, no. 2, pp. 205-221, 1997.
- [14] M. Bussmann, S. Chandra and J. Mostaghimi, “Modeling the splash of a droplet impacting a solid surface”, *Phys. Fluids*, vol. 12, no. 12, pp. 3121-3132, 2000.
- [15] M. Renardy, Y. Renardy and J. Li, “Numerical simulation of moving contact line problems using a volume-of-fluid method”, *J. Comput. Phys.*, vol. 171, no. 1, pp. 243-263, 2001.
- [16] R. Rioboo, M. Marengo and C. Tropea, “Time evolution of liquid drop impact onto solid, dry surfaces”, *Exp. Fluids*, vol. 33, no. 1, pp. 112-124, 2002.
- [17] C. Clanet, C. Beguin, D. Richard and D. Quere, “Maximal deformation of an impacting drop”, *J. Fluid Mech.*, vol. 517, pp. 199-208, 2004.
- [18] T. Mao, D. Kuhn and H. Tran, “Spread and rebound of liquid droplets upon impact on flat surfaces”, *AIChE J.*, vol. 43, no. 9, pp. 2169-2179, 1997.
- [19] M. Pasandideh-Fard, Y. Qiao, S. Chandra and J. Mostaghimi, “Capillary effects during droplet impact on a solid surface”, *Phys. Fluids*, vol. 8, no. 3, pp. 650-659, 1996.
- [20] P. Attane, F. Girard and V. Morin, “An energy balance approach of the dynamics of drop impact on a solid surface”, *Phys. Fluids*, vol. 19, 012101-17, 2007.
- [21] C. Ukiwe and D. Y. Kwok, “On the maximum spreading diameter of impacting droplets on well-prepared solid surfaces”, *Langmuir*, vol. 21, no. 2, pp. 666-673, 2005.
- [22] B.L. Scheller and D.W. Bousfield, “Newtonian drop impact with a solid surface”, *AIChE J.*, vol. 41, no. 6, pp. 1357-1367, 1995.
- [23] I.V. Roisman, “Inertia dominated drop collisions. II. An analytical solution of the Navier–Stokes equations for a spreading viscous film”, *Phys. Fluids*, vol. 21, pp. 052104-11, 2009.
- [24] S. M. An and S. Y. Lee, “Maximum spreading of a shear-thinning liquid drop impacting on dry solid surfaces”, *Exp. Ther. Flui. Sci.*, vol. 38, pp. 140-148, 2012.
- [25] A. Carre, J. Gastel and M. Shanahan, “Viscoelastic effects in the spreading of liquids”, *Nature*, vol. 379, pp. 432-434, 1996.
- [26] V. Bergeron, D. Bonn, J. Yves Martin and L. Vovelle, “Controlling droplet deposition with polymer additives”, *Nature*, vol. 405, pp. 772-775, 2000.

- [27] D. Bartolo, A. Boudaoud, G. Narcy and D. Bonn, “Dynamics of non-Newtonian droplets”, *Phys. Rev. Lett.*, vol. 99, pp. 174502, 2007.
- [28] M. I. Smith and V. Bertola, “Effect of polymer additives on the wetting of impacting droplets”, *Phys. Rev. Lett.*, vol. 104, pp. 154502, 2010.
- [29] F. Vega and F. García, “Pattern imaging of primary and secondary electrohydrodynamic instabilities”, *J. Fluid Mech.*, vol. 549, pp. 61-69, 2006.
- [30] F. Vega and A. T. Pérez, “Corona-induced electrohydrodynamic instabilities in low conducting liquids”, *Exp. Fluids*, vol. 34, no. 6, pp. 726-735, 2003.
- [31] S. U. Ryu and S. Y. Lee , “Maximum spreading of electrically charged droplets impacting on dielectric substrates”, *Int. J. of Multiphase Flow*, vol. 35, no. 1, pp. 1-7, 2009.
- [32] S. R. Mahmoudi, K. Adamiak and G. S. P. Castle, “Spreading of a dielectric droplet through an interfacial electric pressure”, *Proc. R. Soc.*, vol. 467, 3257, pp. 1-15, 2011.
- [33] S. R. Mahmoudi, G. S. P. Castle and K. Adamiak, “Retraction control of an impacted dielectric droplet through electrical pressure”, *Soft Matter*, vol. 8, no. 3, pp. 808-813, 2012.
- [34] O. Ghazian, K. Adamiak and G. S. P. Castle, “Electric-field-induced oscillations of water droplets deposited on insulating surfaces”, *J. Electrostat.*, vol. 71, no. 3, pp. 489-495, 2013.
- [35] O. Ghazian, K. Adamiak and G. S. P. Castle, “Numerical simulation of electrically deformed droplets less conductive than ambient fluid”, *Colloids and Surfaces A: Physicochem. Eng. Aspects*, vol. 423, no. 20, pp. 27-34, 2013.
- [36] Y. D. Shikhmurzaev, “Capillary flows with forming interfaces”, Chapman & Hall/CRC: Boca Raton, FL, 2007.
- [37] Y.D. Shikhmurzaev, “Singularities at the moving contact line, Mathematical, physical and computational aspects”, *Physica D: Nonlinear Phenomena*, vol. 217, no. 2, pp. 121-133, 2006.
- [38] Comsol Multiphysics User’s Guide, (COMSOL 4.3).
- [39] L. Rayleigh, “On the equilibrium of liquid conducting masses charged with electricity”, *Phil. Mag.*, vol. 5, no. 87, pp. 184-186, 1882.

- [40] C. Mundo, M. Sommerfeld and C. Tropea, "Droplet-wall collisions: experimental studies of the deformation and breakup process", *Int. J. Multiph. Flow*, vol. 21, no. 2, pp. 151-173, 1995.
- [41] A. Gomez and K. Tang, "Charge and Fission of Droplets in Electrostatic Sprays", *Phys. Fluids*, vol. 6, no.1, pp. 404-414, 1994.
- [42] A. Grigorev and S. O. Shiryayeva, "Mechanism of electrostatic polydispersion of liquid", *J. Phys. D: Appl. Phys.*, vol. 23, no.11, pp.1361-1370, 1990.
- [43] IEEE-DEIS-EHD Technical Committee, "Recommended international standard for dimensionless parameters used in electrohydrodynamics", *IEEE Tran. on Dielectr. and Electr. Insul.*, vol. 10, no.1, pp. 3-6, 2003.

## Chapter 7

### 7 « Head-on collision of electrically charged droplets »

#### 7.1 Introduction

Charged droplets play a significant role in a wide range of applications, such as electro spray atomization [1-4], fuel injection and formation of clouds [5-6].

The electric force can also be used to enhance the separation and coalescence of small droplets. The interaction between electric field and single charged droplets has already been extensively studied [7-10], but droplet collision is still not well understood. Park [11] produced collisions between streams of water droplets traveling in still air and showed pictorially that near head-on collision between pairs of equally sized droplets resulted in stable coalescence. Ashgriz and Poo [12] developed models for predicting the boundary between the coalescence and separation regimes. In general, the outcome of the drop collision can be categorized into four different types: bouncing, coalescence, separation, and shattering collisions. At higher Weber number for head-on or near head-on cases, reflexive separation may happen resulting in formation of satellites. “Shattering” occurs at extremely high Weber numbers, which is beyond the scope of the conventional application.

As reported by Qian and Law [13], for head-on collisions of water droplets at atmospheric pressure bouncing is not observed; for the same conditions however, the collision between hydrocarbon droplets may result in bouncing. The collision behavior of fuel droplets were found to vary significantly from those of water droplets. The most noticeable difference is the bouncing phenomena. Estrade et al. [14] published information about the number of satellite droplets, their sizes and velocities produced by bouncing collisions. Brenn et al. [15] produced a nomogram for the various collision regimes and for the number of satellite droplets formed during droplet collision depending on the Weber number and impact parameter, which agreed quite well with the experimental results of Ashgriz and Poo [12].

There are a few studies on the numerical simulation of the droplet collision. Nobari et al. [16] used the front tracking method in axi-symmetric formulation for the central collision; the method was able to capture the features of bouncing, coalescence and reflexive separation with up to one satellite droplet formed. Mashayek et al. [17] studied the coalescence collision of two droplets in axi-symmetric geometry, using a Galerkin Finite Element Method. Recently, Pan and Suga [18] using the implicit continuous-fluid Eulerian method coupled with the Level-Set methodology for a single phase in a fixed uniform mesh system, simulated the three major regimes of binary collision (bouncing, coalescence and separation), both for water and hydrocarbon droplets. Their numerical results suggest that the mechanism of bouncing collision is governed by the macroscopic dynamics, while the mechanism of coalescence is related to the microscopic dynamics. Tanguy and Berlemont [19] performed simulation using a Level-Set method. Results of coalescence, reflexive separation and stretching separation were found in good agreement with experiments. Nikolopoulos et al. [20, 21] conducted numerical investigation of both head-on and off-centre droplet collision based on the volume of fluid (VOF) method. Their results provided a detailed picture of the collision process, the ligament formation and dimensions, the pinch-off mechanism, as well as the creation of the satellite droplet. They further investigated the effect of gas, liquid properties and droplet size ratio on the central collision between two unequal-size droplets in the reflexive regime [22], results of which show that the droplet size ratio, rather than the Reynolds number based on the gas properties, is an important parameter affecting the collision outcome. Chen et al. [23] analyzed energy and mass transfer during binary droplet collision based on the VOF simulation. The mass transfer process was studied in detail, whereas the energy transfer process was only investigated with the overall energy balance. Estrade et al. [24] for the first time included information about the number of the satellite droplets in separation collisions.

Literature on the investigation of interactions between two charged droplets is extremely scarce [25]. The feasibility of coalescence of two perfectly conducting, electrically charged droplets was studied from a thermodynamic point of view by Gallily et al. [26]. A suitable expression was developed for the electrical energy of the two droplets which make the initial contact. It was proven by Lekner [27] that two charged conducting



spheres will almost always attract each other at a close distance. Surprisingly, this is true even when they have like charges. The one exception is when the two spheres have a charge ratio which would result from droplets making mechanical contact. Phase Doppler anemometry measurements and flow visualizations were used to measure the structures of electrostatically atomized hydrocarbon fuel sprays by Shrimpton and Yule [28].

The purpose of the present study is to investigate the electrostatic interaction of charged droplets considering different physical parameters and impact velocities with the aim of providing broader and more in depth insight into the collision of charged droplets and different outcome regimes. The Navier–Stokes equations with the volumetric forces due to surface tension and electric charges are solved numerically by the finite element methodology.

There are three aspects of the present investigation. First, in order to validate the model the numerical results are compared in detail with the images of the simulated liquid droplet collision obtained by Pan and Suga [18]. Secondly, the mechanism of Coulomb attraction between two like charged conducting droplets is investigated. The third aspect of the study concerns the collision dynamics of two charged droplets and satellite droplet formation.

## 7.2 The mathematical model

The flow is considered as axi-symmetric, incompressible and laminar. The main parameters affecting the process are grouped in two dimensionless numbers: Reynolds  $Re = \frac{\rho_{drop} D_0 (2U_0)}{\mu_{drop}}$  and Weber  $We = \frac{\rho_{drop} D_0 (2U_0)^2}{\sigma}$ , where  $D_0$  is the initial drop diameter,  $U_0$  is the impact velocity, and  $\rho_{drop}$ ,  $\mu_{drop}$  and  $\sigma$  are the liquid density, viscosity and surface tension, respectively.

In order to investigate the dynamics of droplet deformation in an electric field it is necessary to solve the Navier-Stokes equations governing the fluid motion, as well as track the interface between both fluids. The laminar two-phase flow studied here is coupled with the applied electric field and electric charges on the interface. Additional body forces are added to the Navier-Stokes equations for considering the surface tension ( $\mathbf{F}_{st}$ ) and electric stress ( $\mathbf{F}_{es}$ ).

The computational domain is shown in Figure 7.1. In most of previous numerical and experimental studies, the droplets were assumed to have equal, but opposite velocities before collision. At the beginning of the simulation,  $t = 0$ , the centers of the droplets are  $2D_0$  apart approaching each other with a relative velocity  $2U_0$ , whilst the surrounding gas has zero velocity. Due to the symmetry only one droplet, shown in the figures, needs to be considered, because the other droplet is identical and the top edge of the domain is the symmetry line.

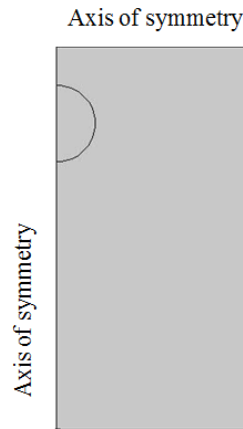


Figure 7.1 Initial configuration used in numerical simulation of droplet impact

In order to investigate the grid dependency of the results, three grids with 20, 40, and 100 cells per initial droplet diameter were considered. It was found that the calculated parameters of droplet shapes did not vary significantly, if the element size is smaller than  $D_0/40$ . Therefore, all further simulations were performed using such a mesh.

The radius and height of the cylindrical computational domains are  $3D_0$  and  $5D_0$ , respectively. The increase in size of the chosen domain has been found to have a negligibly small effect on the solution. The computational domain is therefore large enough to neglect the effects of the domain truncation.

The behavior of the binary fluid system is governed by the level set equation. In the present study, the discretization and calculation procedure follow that described by Ghazian et al. [29-31]. The level set function moves with the fluid at velocity  $u$  as a passive scalar variable. The density and the viscosity are calculated throughout the

computational domain depending on the value of  $\phi$ . The fluid properties continuously change across the interfacial region. Note that in the experiments, the droplet diameters were in the range of 100-500  $\mu\text{m}$ . In such cases, the gravity effects are negligible since the Bond number is always small.

### 7.3 Verification of the numerical method

Figure 7.2 shows a sequence of results from the present simulation for two uncharged colliding droplets compared with the simulations of Pan and Suga [18].

As the droplets approach each other, high pressure is built up in the gap; the droplets are flattened, conversion of the droplet kinetic energy into surface tension energy takes place and gas is squeezed out in a form of a jet sheet.

The merged mass continues to deform into a donut shape. After coalescence, it is retracted into a cylindrical rod, which later stretches longer and thinner, until it eventually breaks into two primary droplets with one secondary drop. During most of the collision process, consisting of the stretching filament, its disintegration between bulbous ends, and the further breakup, the comparison shows very reasonable agreement.

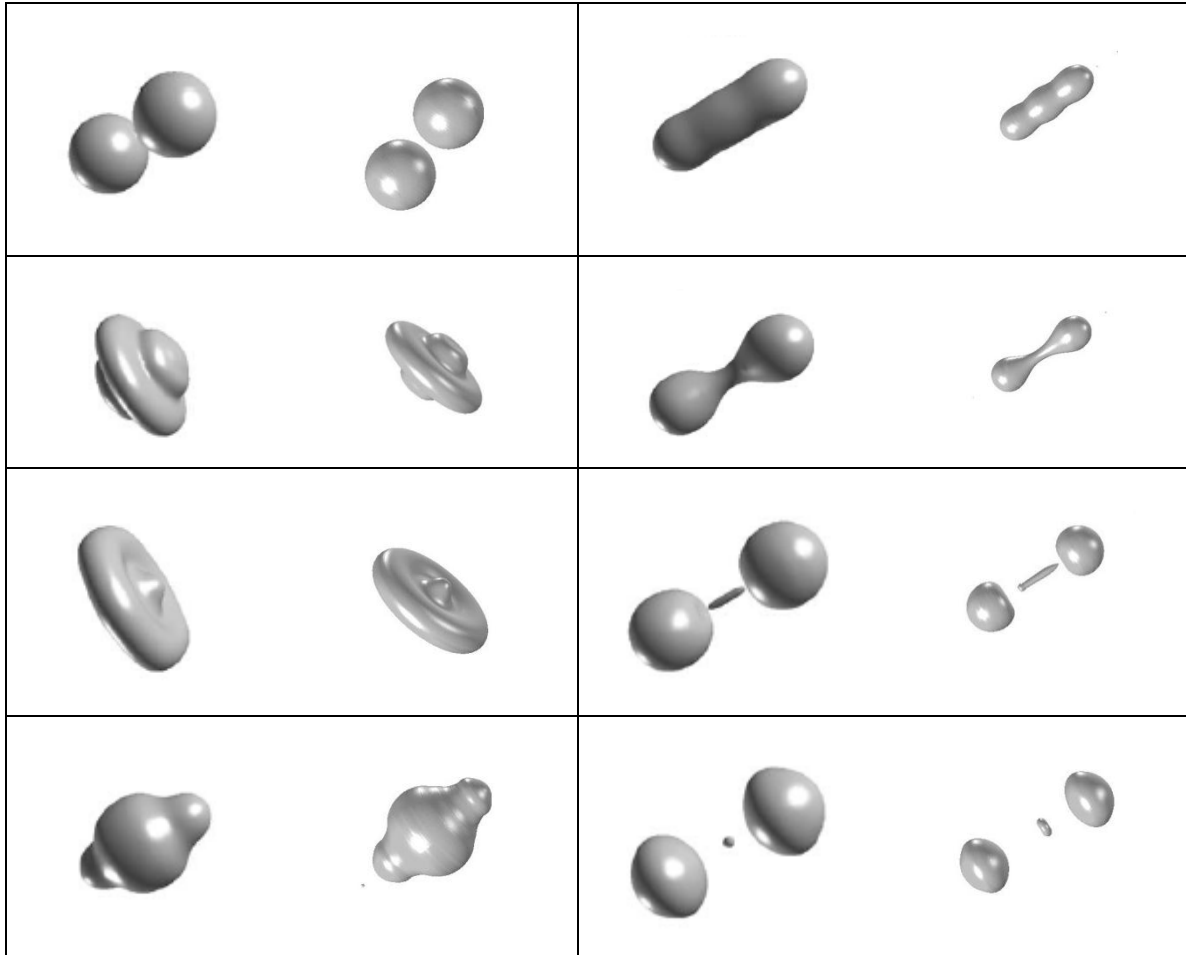


Figure 7.2 Pan and Suga simulation [18] (left) and our simulated (right) snapshots of head-on collision of two uncharged water droplets in air. The initial droplet diameter is  $300\ \mu\text{m}$  and the relative velocity of collision is  $0.28\ \text{m/s}$

## 7.4 Results and discussion

In this section the model is extended to study the Coulomb attraction between two stationary conducting droplets. In the second part, the collision dynamics of two identical charged droplets is reported. Some interesting features of the charged droplet disintegration and satellite droplet formation are illustrated via various examples.

### 7.4.1 Two stationary conducting droplets

The presented results of simulation illustrate how the surfaces of the two droplets are deformed due to the electrostatic interactions between them. In particular, modification of the electrostatic interactions caused by the droplet deformations will be investigated. This aspect has not been discussed elsewhere.

As shown below, surprisingly Coulomb attraction may exist between two conducting droplets carrying the same sign charges.

In the first example, we consider the case of two identical spherical droplets separated from each other by an initial distance of 2.5 radii between their centers. The maximum electric charge that a single isolated droplet can theoretically carry can be evaluated from the Rayleigh limit:

$$q_{Ray} = 8\pi(\varepsilon_0\sigma r^3)^{1/2}$$

where  $\varepsilon_0$  is the vacuum permittivity and  $r$  is the radius of the droplet. The simulations were performed for the following parameters:  $\rho_{drop} = 1000 \text{ kg/m}^3$ ,  $\rho_{air} = 1 \times 10^{-3} \text{ kg/m}^3$ ,  $\mu_{drop} = 0.001 \text{ Pa} \cdot \text{s}$ ,  $\mu_{air} = 2 \times 10^{-5} \text{ Pa} \cdot \text{s}$ ,  $\sigma = 0.073 \text{ N/m}$ ,  $r = 100 \text{ } \mu\text{m}$ . The maximum Rayleigh charge is calculated to be  $q_{Ray} = 20 \text{ pC}$ .

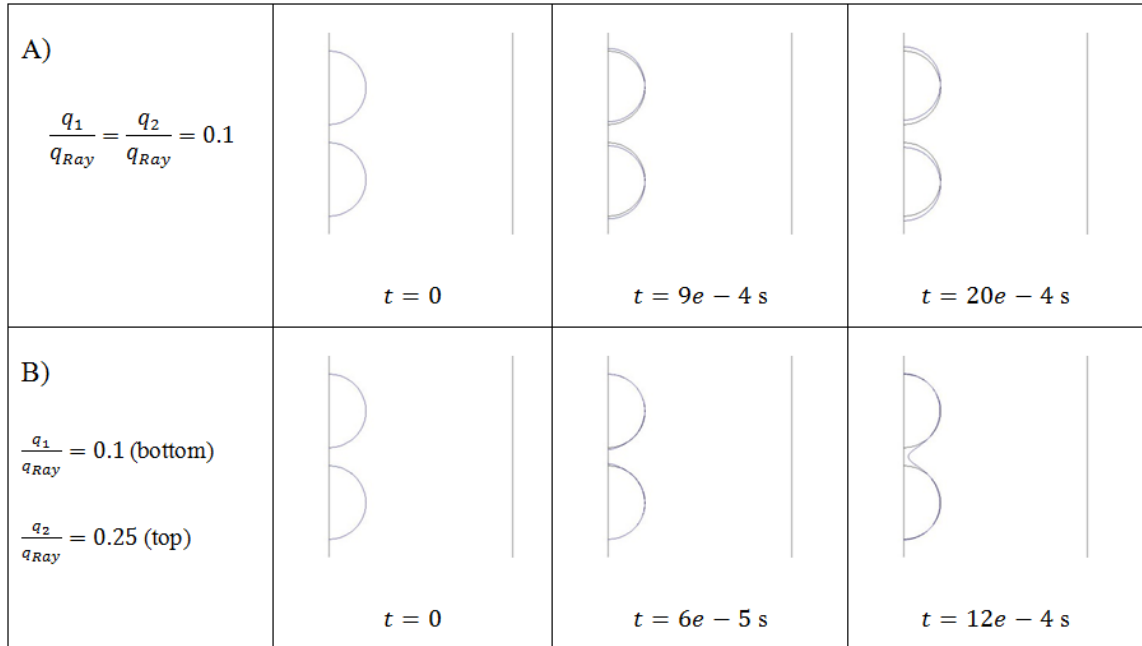


Figure 7.3 Interaction between two identical spherical droplets with the same (A) and different charges (B) at an initial distance of 2.5 radii between centers

As it can be expected, droplets with the same magnitude and sign of charge (Figure 7.3A) repel each other. However, in the case where the droplets have different charge magnitudes (Figure 7.3B), the droplets attract each other, even though they carry charge of the same polarity. The two droplets will eventually move towards and collide with each other after forming conical protrusions at the contact point. It can be deduced that the lower part of the upper droplet carries negative charge, while the upper part of it carries the opposite charge.

By keeping the same value for charge (Figure 7.3B) and increasing the distance between the droplets, the droplets will repel each other (Figure 7.4). This example indicates that the distance plays an important role in Coulomb attraction for the droplets charged with the same polarity. It also proves that conducting droplets will almost always attract each other at close proximity, even when they have like charges.

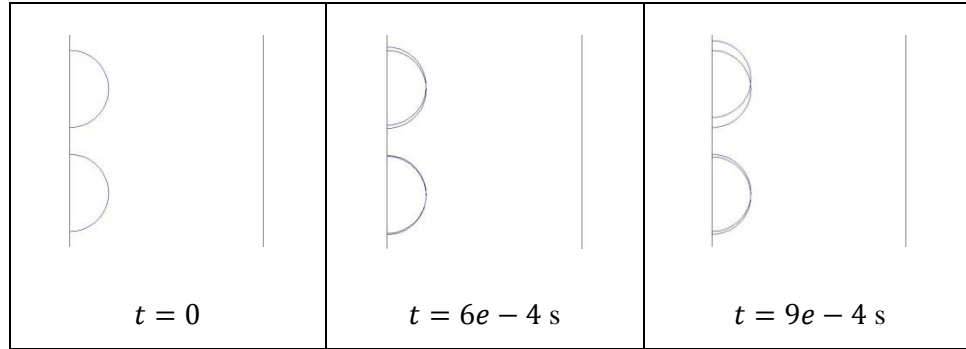


Figure 7.4 Two identical spherical droplets with different charges at a larger distance of 2.7 radii between the two centers,  $q_1/q_{Ray}=0.1$  (bottom),  $q_2/q_{Ray}=0.25$  (top)

Contrary to common sense, it seems that two conducting droplets carrying charges of the same polarity can attract each other in some situations. This apparent paradox can be easily understood by noting that the charge on a conductor is not fixed but free to move on the surface of the droplets under the action of an electric field. When the two conducting droplets move towards each other, the surface charges will redistribute and a net attraction force will be created between them due to the unsymmetrical charge distribution. In addition, the electric force will also result in deformation of the two droplets close to the facing sides, which in turn will enhance the charge redistribution since charges will move to locations of high surface curvature. Obviously, this destabilizing mechanism will not happen in the case of rigid spheres.

Figure 7.5 illustrates the limit between the attraction and repulsion regimes for two identical droplets, where  $d_0$  is the initial distance between the droplet centers. It is clear that in order to get the attraction regime, the charge ratio should increase when the distance between the droplets increases. There is a maximum distance ( $d_0 = 2.8 r$ ), beyond which the repulsion is always dominant. It can be concluded that the attraction occurs at a shorter distance when droplets have closer charges.

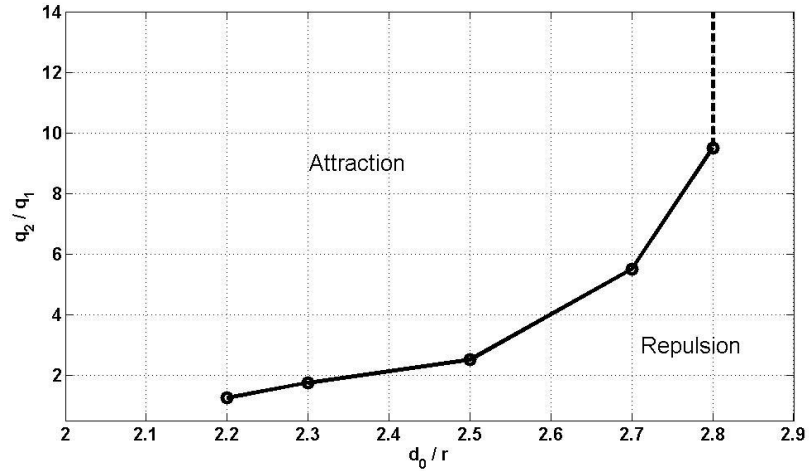


Figure 7.5 The limit between attraction and repulsion regimes for two identical droplets

## 7.4.2 Impacting dielectric droplets

In this section the collision of two charged dielectric droplets is considered. The simulations were performed for the following parameters:  $\rho_{drop} = 1000 \text{ kg/m}^3$ ,  $\rho_{air} = 1 \times 10^{-3} \text{ kg/m}^3$ ,  $\mu_{drop} = 0.003 \text{ Pa} \cdot \text{s}$ ,  $\mu_{air} = 2 \times 10^{-5} \text{ Pa} \cdot \text{s}$ ,  $\sigma = 0.03 \text{ N/m}$ ,  $D_0 = 200 \text{ } \mu\text{m}$ .

Initial distance between both droplets is equal to two droplet diameters. At the beginning of the simulation,  $t=0$ , a uniform velocity  $U_0$  is imposed on each of the two liquid droplets in opposite but approaching directions, while the surrounding gas is stationary.

Grid dependence tests have been already performed using different discretization densities and it has been confirmed that the presented results are reasonably grid independent.

### 7.4.2.1 Effect of Weber number

Two regimes can be clearly identified at low Weber numbers in this process. In the first one, the droplets initially start to move towards each other, but the kinetic energy is not sufficiently high to overcome the electrostatic repulsion. Since the droplet velocity is too small, the droplets repel each other due to the electrostatic force and do not even touch (Figure 7.6). To nondimensionalize time we have the choice to use the advection time



( $t_0 = D_0/U_0$ ) of the droplets before impact. Our results are presented using the advective time scale.

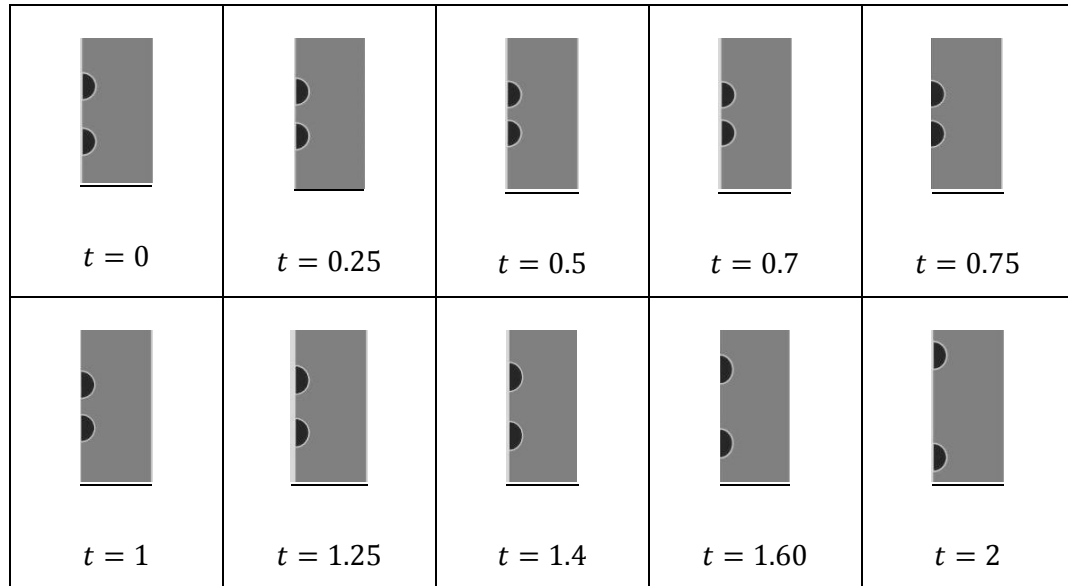


Figure 7.6 Shape evolution of the head-on collision of two equal-size droplets for  $We=6.7$ ,  $Re=66.7$  and  $q/q_{Ray}=0.5$

Figure 7.7 illustrates the case of the droplets with the same value of the charge, but for higher Weber number. It is clear that the droplets collide and form a larger one, which oscillates until it reaches steady-state. Simulations are continued until oscillations of the combined droplet completely decay.

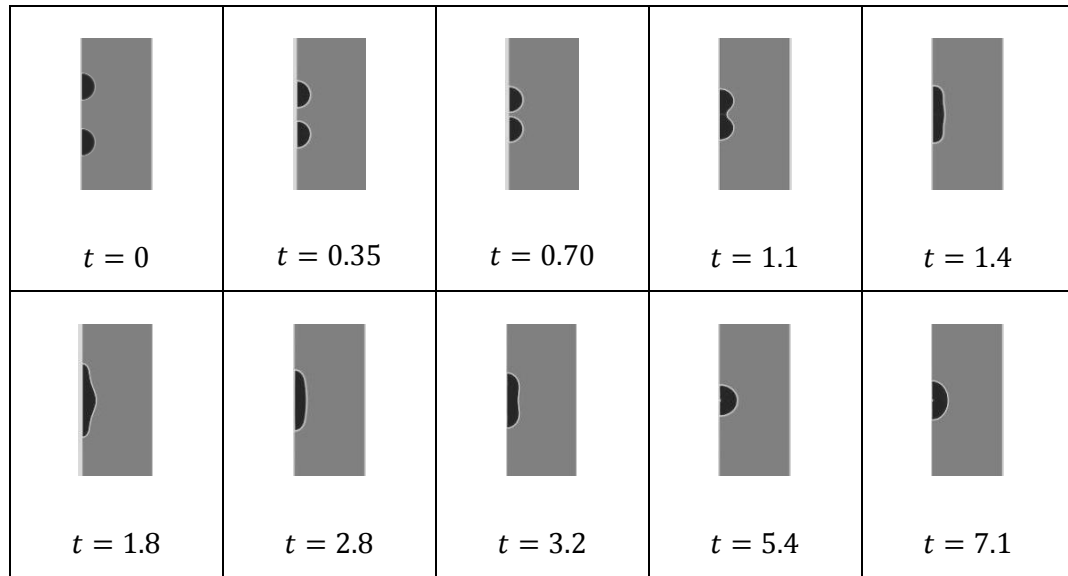


Figure 7.7 Shape evolution of the head-on collision of two equal-size droplets for  $We=13$ ,  $Re=94.3$  and  $q/q_{Ray}=0.5$

The simulation was also carried out for increased droplet charge and keeping the velocity constant (Figure 7.8); it is clear that here the droplets are repelling each other even though the magnitude of the Weber number is the same as in Figure 7.7.

This behavior can be explained by considering the fact that since the Weber number and the initial impact velocity are kept constant, the electrostatic force becomes dominant and prevents droplets from colliding.

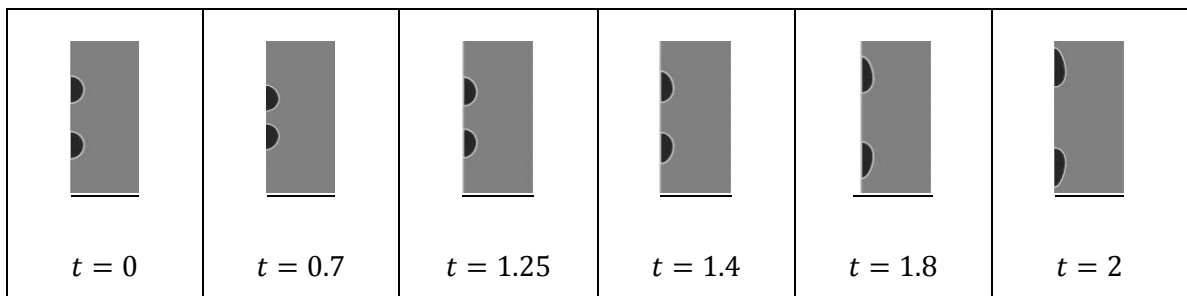


Figure 7.8 Shape evolution of the head-on collision of two equal-size droplets for  $We=13$ ,  $Re=94.3$  and  $q/q_{Ray}=0.7$

A map can be drawn to show the limit between the repulsion and coalescence regimes. The graph in Figure 7.9 shows the boundary between the repulsion and coalescence for the fixed initial distance of  $d_0 = 4r$ . At higher droplet charge the coalescence occurs, but

higher Weber number is necessary. Theoretically, the droplet charge can be increased up to the Rayleigh limit, before the droplet becomes unstable. In the investigated models the droplet charge was increased up to 80 percent of the Rayleigh limit without observing any instability.

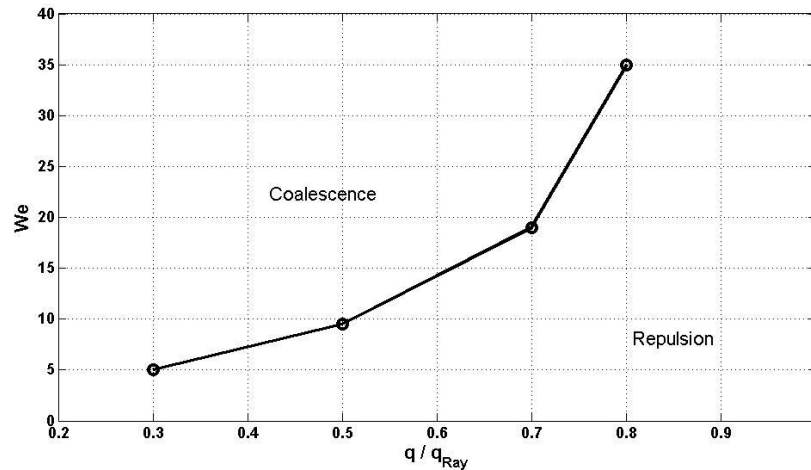


Figure 7.9 The limit between coalescence and repulsion regimes for two identical impacting droplets with the initial distance of  $d_0=4r$

#### 7.4.2.2 Effect of the droplet charge in the break-up regime

The effect of the droplet charge on the collision between two identical dielectric droplets has also been considered. The droplets have been impacted at much higher velocities and both droplets have been charged up to 50% of the Rayleigh limit, which is  $q_{Ray} = 13$  pC for the 100 micron size droplets considered in this section.

The charge was placed in the small finite interface surrounding the surface of the drop using the level set variable distribution. The total charge was kept constant and calculated by integration over the surface of the droplet. The total surface area has been calculated and a uniform charge distribution was considered on the droplets in a way that the total charge is still kept constant. Figure 7.10 shows the head-on collision of two identical neutral droplets.

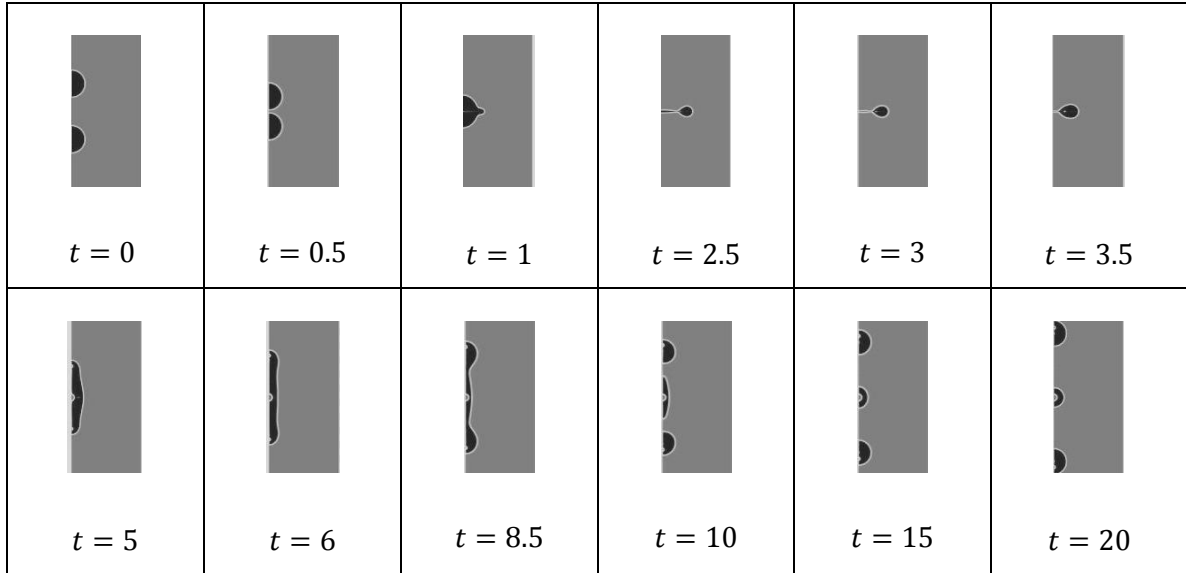


Figure 7.10 Shape evolution of the head-on collision of two neutral equal-size droplets for  $We=106.7$ ,  $Re=266.67$  and  $q/q_{Ray}=0$

The droplets first coalesce and then reach the maximum deformation in the radial direction forming a thin disc with a toroidal rim. This shape then contracts under the effects of surface tension attempting to recover the spherical shape. However, due to inertia a liquid cylinder is formed and it continuously stretches until it eventually breaks, if it has sufficient energy. It can be seen that the ligament stretches leaving a daughter droplet between the bulbous ends.

A relatively small amount of gas is trapped in the coalesced mass of droplets. Such micro-bubble entrapment, due to the formation of curved interfaces on the approaching sides of the droplets, has been observed experimentally by Ashgriz and Poo [12].

In addition, a recent high-resolution computation of two approaching drops using the VOF method also showed that a small portion of ambient fluid gets trapped during coalescence [32]. The formation of a micro-bubble at low  $We$  reported in our paper is thus apparently a physical macroscopic effect and not a numerical artifact.

If the droplets are charged up to 30% of the Rayleigh limit (Figure 7.11), there is no obvious change in the collision pattern, if the Weber number is kept at the same level. By further increasing the initial droplet charge up to 50 % (Figure 7.12), the daughter

droplets break into smaller ones and this continues until the radius of the droplet gets close to the mesh size.

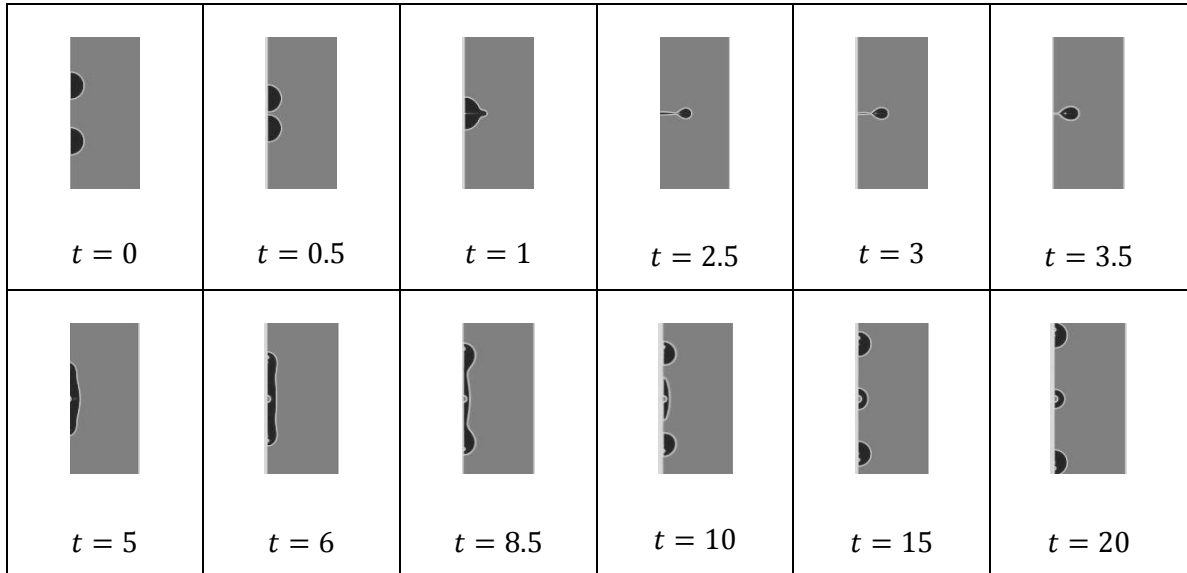


Figure 7.11 Shape evolution of the head-on collision of two equal-size droplets for  $We=106.7$ ,  $Re=266.67$  and  $q/q_{Ray}=0.3$

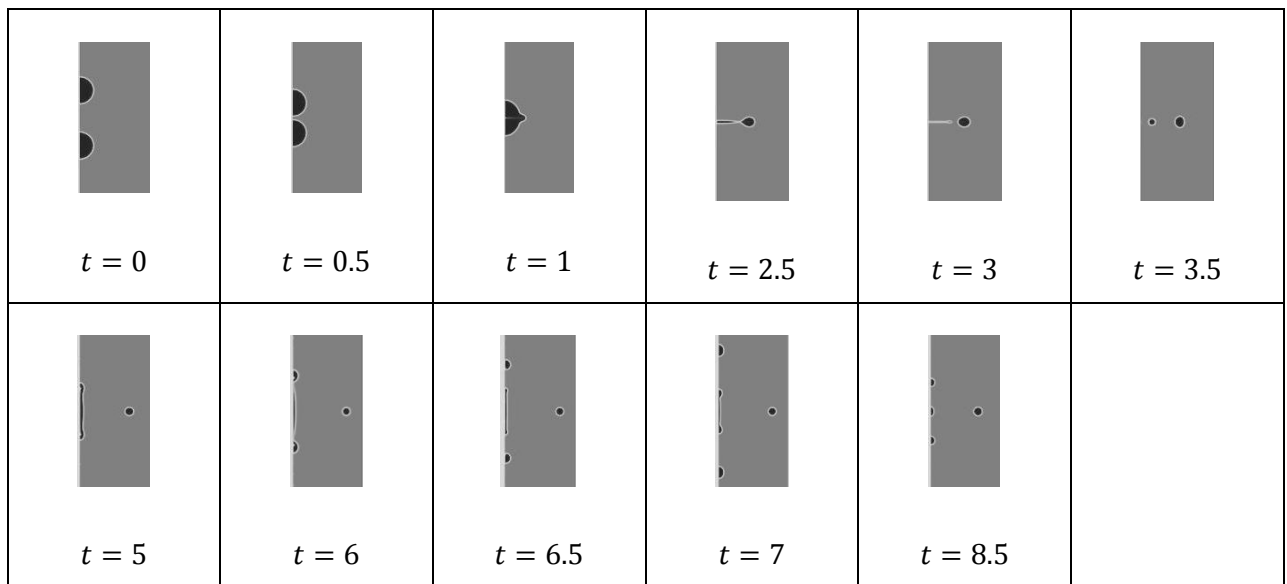


Figure 7.12 Shape evolution of the head-on collision of two equal-size droplets for  $We=106.7$ ,  $Re=266.67$  and  $q/q_{Ray}=0.5$

Since the surface tension of the stretched droplet cannot hold the large amount of kinetic energy, even with the stabilization effect of viscous dissipation, the merged droplet eventually separates and a smaller, satellite droplets are continuously formed. It was found that by increasing the charge, the droplets will disintegrate into a larger number of daughter droplets after collisions.

### 7.4.3 Unequal-size droplets:

In practical atomization processes, unequal-size droplet collisions are more frequent than equal-size cases; however, they have been less examined both experimentally and numerically. Equal-size droplet collisions have minimal mixing after droplet coalescence due to the symmetry with respect to the collision plane. Thus, breaking the symmetry through the unequal droplet sizes may result in improved mixing upon coalescence. In the present study, simulations were carried out to investigate the dynamics of unequal-size droplets collision. Before the droplets collide, there is a squeezed gas between the droplet interfaces which produces some localized excess energy and needs to be ejected. A smaller repulsive force from the compressed gas flow between the droplets can be assumed for the smaller droplet due to the smaller frontal area which promotes coalescence. For the larger droplet, more energy can be dissipated by internal motion and the coalesced droplet can be stabilized.

The charge ratio on droplets is equal to the surface ratio of the droplets, which assumes identical surface charge density. The symmetry boundary condition cannot be used in this part due to difference in size of the droplets. The schematic of the problem is shown in Figure 7.13.

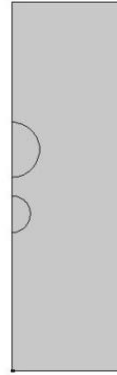


Figure 7.13 Computational domain for simulating collision of droplets with different size

The impact of droplets with radii of  $100\ \mu\text{m}$  and  $150\ \mu\text{m}$  is shown in Figure 7.14. The initial velocity of  $U_0 = 2\ \text{m/s}$  is assumed for both droplets. The Weber number and nondimensional time are calculated based on the diameter of the larger droplet.

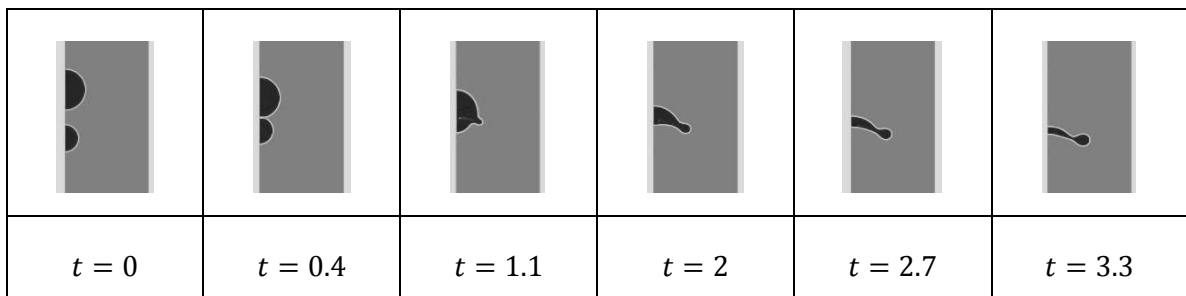


Figure 7.14 Snapshots of droplet motion of larger (upper) and smaller (lower) neutral spherical droplets with  $R_2/R_1=1.5$  at  $We=160$  and  $Re=400$

For unequal-size droplet collision, the droplet deformation is more complex because of the loss of the symmetric shape. Two droplets impinge head-on and spread outwardly in the radial direction to form a flying-saucer-like shape upon merging. By increasing the Weber number (Figure 7.15), the saucer-like shape becomes more stretched in the radial direction and a ring at the edge of the combined droplet becomes smaller in size leading to ejection of a small droplet.

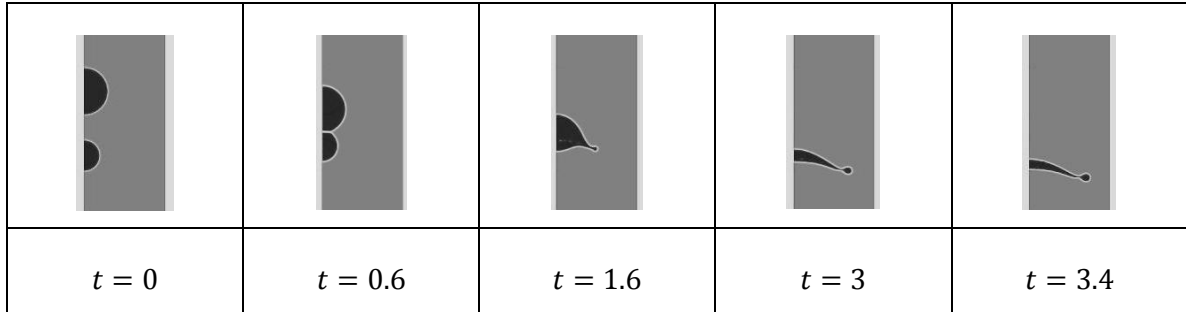


Figure 7.15 Snapshots of droplet motions between a larger (upper) and a smaller (lower) neutral spherical droplets with  $R_2/R_1=1.5$  at  $We=360$  and  $Re=600$

## 7.5 Conclusions

The head-on collision of two liquid drops is studied using the FEM. The effects of the impact velocity, drop size ratio and electric charge on the behavior of the combined droplet are investigated. The present study proves the feasibility of applying the Level-Set method as a numerical technique to investigate the collision dynamics of electrically charged droplets.

It is demonstrated that the presented numerical method is able to capture the droplet collision in the presence of the electric charges on the surface of the droplets. It was also shown that two conducting droplets carrying charges of the same polarity under some conditions may be electrically attracted.

The formation of charged daughter droplets has been investigated and it was found that the number of the satellite droplets after collision appears to increase with an increase in the droplet charge.



## Nomenclature

$d_0$	Initial distance of droplets	$t_0$	Time scale
$D_0$	Initial droplet diameter	$u$	Velocity
$E$	Electric field	$U_0$	Impact velocity
$F_{es}$	Electric force	$We$	Weber number
$F_{st}$	Surface tension force	Greek symbols	
$I$	Identity matrix	$\alpha$	Reinitialization parameter
$n$	Interface normal	$\epsilon_r$	Relative permittivity
$P$	Pressure	$\epsilon_{ls}$	Parameter controlling the interface thickness
$q$	Droplet charge	$\epsilon_0$	Permittivity of vacuum
$q_{Ray}$	Rayleigh limit	$\phi$	Level-set function
$r$	Droplet radius	$\rho_{air}$	Air density
$Re$	Reynolds number	$\rho_{drop}$	Droplet density
$T$	Capillary pressure tensor	$\mu_{air}$	Air dynamic viscosity
$T_M$	Maxwell stress tensor	$\mu_{drop}$	Droplet viscosity
$t$	Nondimensional time	$\sigma$	Surface tension

## References

- [1] L. D. Juan and J. Fernandez De La Mora, "Charge and size distributions of electrospray drops", *J. Colloid Interface Sci.*, vol. 186, no. 2, pp. 280-293, 1997.
- [2] N. V. Krasnov and S. I. Shevchenko, "Comprehensive studies of electrohydrodynamic spraying of liquids", *Rev. Sci. Instrum.*, vol. 66, no. 6, pp. 3623-3626, 1995.
- [3] H. Okuda and A. J. Kelly, "Electrostatic atomization: Experiment, theory and industrial applications", *Phys. Plasmas*, vol. 3, no. 5, pp. 2191-2196, 1996.
- [4] J. S. Eow, M. Ghadiri and A. Sharif, "Experimental studies of deformation and break-up of aqueous drops in high electric fields", *Colloids Surf., A*, vol. 225, no. 1-3, pp. 193-210, 2003.
- [5] B. A. Tinsley, R. P. Rourbaugh, M. Hei and K. V. Beard, "Effects of image charges on the scavenging of aerosol particles by cloud droplets and on droplet charging and possible ice nucleation processes", *J. Atmos. Sci.*, vol. 57, no. 13, pp. 2118-2134, 2000.
- [6] K. V. Beard, R. I. Durkee and H. T. Ochs, "Coalescence efficiency measurements for minimally charged cloud drops", *J. Atmos. Sci.*, vol. 59, no. 2, pp. 233-243, 2002.
- [7] J. Q. Feng and K. V. Beard, "Small-amplitude oscillations of electrostatically levitated drops", *Proc. R. Soc. London, Ser. A*, vol. 430, no. 1878, pp. 133-150, 1990.
- [8] K. C. Sang and E. H. Trinh, "Internal flow of an electrostatically levitated droplet undergoing resonant shape oscillation", *Phys. Fluid.*, vol. 12, no. 2, pp. 249-251, 2000.
- [9] D. Duft, T. Achtzehn, R. Muller, B. A. Huber and T. Leisner, "Coulomb fission: Rayleigh jets from levitated microdroplets", *Nature*, London, vol. 421, no. 1, pp. 128-128, 2003.
- [10] Lord Rayleigh, "On the equilibrium of liquid conducting masses charged with electricity", *Philos. Mag.*, vol. 14, no. 87, pp. 184-186, 1882.
- [11] R.W. Park, "Behavior of Water Drops Colliding in Humid Nitrogen", PhD Thesis, Department of Chemical Engineering, The University of Wisconsin, 1970.
- [12] N. Ashgriz and J.Y. Poo, "Coalescence and separation in binary collision of liquid drops", *J. Fluid. Mech.*, vol. 221, pp. 183-204, 1990.
- [13] J. Qian and C.K. Law, "Regimes of coalescence and separation in droplet collision", *J. Fluid Mech.*, vol. 331, pp. 59-81, 1997.

- [14] J. P. Estrade, H. Carentz, G. Lavergne and Y. Biscos, "Experimental investigation of dynamic binary collision of ethanol droplets-A model for droplet coalescence and bouncing", *Int. J. Heat Fluid Flow*, vol. 20, no. 5, pp. 486-491, 1999.
- [15] G. Brenn, D. Valkovska and K. D. Danov, "The formation of satellite droplets by unstable binary drop collision", *Phys Fluids*, vol. 13, pp. 2463-2477, 2001.
- [16] M. R. Nobari, Y. J. Jan and G. Tryggvason, "Head-on collision of drops-A numerical investigation", *Phys. Fluids*, vol. 8, no. 1, pp. 29-42, 1996.
- [17] F. Mashayek, A. Ashgriz, W. J. Minkowycz and B. Shotornan, "Coalescence collision of liquid drops", *Int. J. Heat Mass Transfer*, vol. 46, no. 1, pp. 77-89, 2003.
- [18] Y. Pan and K. Suga, "Numerical simulation of binary liquid droplet collision", *Phys. Fluids*, vol. 17, pp. 082105-14, 2005.
- [19] S. Tanguy and A. Berlemont, "Application of a level set method for simulation of droplet collisions", *Int. J. Multiphase Flow*, vol. 31, no. 9, pp. 1015-1035, 2005.
- [20] N. Nikolopoulos, K. S. Nikas and G. Bergeles, "A numerical investigation of central binary collision of droplets", *Comput. Fluids*, vol. 38, no. 6, pp. 1191-1202, 2009.
- [21] N. Nikolopoulos, A. Theodorakakos and G. Bergeles, "Off-centre binary collision of droplets: a numerical investigation", *Int. J. Heat Mass Transfer*, vol. 52, no. 19-20, pp. 4160-4174, 2009.
- [22] N. Nikolopoulos and G. Bergeles, "The effect of gas and liquid properties and droplet size ratio on the central collision between two unequal-size droplets in the reflexive regime", *Int. J. Heat Mass Transfer*, vol. 54, no. 1-3, pp. 678-691, 2011.
- [23] X. D. Chen, D. J. Ma, P. Khare and V. Yang, "Energy and mass transfer during binary droplet collision", 49th AIAA Aerospace Sciences Meeting including the New Horizons Forum and Aerospace Exposition, Orlando, United States, AIAA 771, pp.1-17, 2011.
- [24] J. P. Estrade, H. Carentz, G. Lavergne and Y. Biscos, "Experimental investigation of dynamic binary collision of ethanol droplets-A model for droplet coalescence and bouncing", *Int. J. Heat Fluid Flow*, vol. 20, no. 5, pp. 486-491, 1999.
- [25] Y. H. Su, "A numerical study of electrostatic interactions between two charged conducting droplets", *Phys. of Fluids*, vol. 18, pp. 042108-10, 2006.

- [26] I. Gallil and G. Ailam (Volinez), "On the coalescence of electrically charged droplets", *J. of Colloid and Interface Sci.*, vol. 30, no. 4, pp. 537-545, 1969.
- [27] J. Lekner, "Electrostatics of two charged conducting spheres", *Proc. R. Soc. A.*, pp. 1-20, 2012.
- [28] J. S. Shrimpton and A. J. Yule, "Characterisation of charged hydrocarbon sprays for application in combustion systems", *Experiments in Fluids*, vol. 26, no. 5, pp. 460-469, 1999.
- [29] O. Ghazian, K. Adamiak and G. S. P. Castle, "Electric-field-induced oscillations of water droplets deposited on insulating surfaces", *J. Electrostat.*, vol. 71, no. 3, pp. 489-495, 2013.
- [30] O. Ghazian, K. Adamiak and G. S. P. Castle, "Numerical simulation of electrically deformed droplets less conductive than ambient fluid", *Colloid. Surf. A: Physicochem. Eng. Aspects*, vol. 423, pp. 27-34, 2013.
- [31] O. Ghazian, K. Adamiak and G. S. P. Castle, "Oscillation, pseudo-rotation and coalescence of sessile droplets in a rotating electric field", *Colloid. Surf. A: Physicochem. Eng. Aspects*, vol. 441, pp. 346-353, 2014.
- [32] S. Hardt, "An extended volume-of-fluid method for micro flows with short-range interaction between fluid interfaces", *Phys. Fluids*, vol. 17, pp. 100601(1-9), 2005.

## Chapter 8

### 8 « Summary and recommendations for future study »

#### 8.1 Summary

In this thesis, a numerical technique was proposed for simulating the behavior of droplets, neutral or charged, exposed to an external electric field. The electrical phenomena were responsible for generating the flow body force; a commercial Finite Element software package, COMSOL, was used in simulations, as it easily links electrostatic and hydrodynamic phenomena. To represent the distortion of free boundaries of the droplet, the Level-Set method has been incorporated into the simulations. The charge was placed on the surface of the drop using the level set variable distribution. The effects of electrostatic forces on a number of problem configurations were investigated. In many cases, the simulation results were compared with the existing experimental data to verify the reliability of the numerical model. The new contributions conducted in this study were presented in five chapters.

In Chapter 2, the implementation of the numerical technique, which covers both the fluid model and its coupling with the electrostatic forces, was described. The original thesis contribution starts with simulating a droplet suspended in another immiscible fluid under DC uniform electric field (Chapter 3). Here, a new break up pattern for droplets less conductive than ambient fluid was demonstrated. In Chapters 4 and 5, the role of solid surfaces has been considered by putting droplets on solid surfaces having different properties. The effect of the surface contact angle on droplet oscillations was demonstrated. It was shown that the contact angle affects the resonance phenomena of the oscillating droplets and the resonance frequency of the water droplet deposited on a hydrophobic surface increases with a decreasing contact angle. Chapter 6 is devoted to the electrostatic manipulation of the droplets impacting onto a solid surface. The effect of the electrostatic forces on maximum spreading diameter, an important parameter relevant to many applications, was investigated. It was found that by increasing the droplet charge, it may be possible to increase the spreading without any retraction after the droplet reaches its maximum diameter. The numerical technique was also applied to

investigate the collision of electrically charged droplets in Chapter 7. It was demonstrated that two conducting droplets carrying charges of the same polarity under some conditions may be electrically attracted. A map was drawn to show the limit between the repulsion and coalescence regimes. This Chapter also addressed the collision dynamics of two charged droplets and satellite droplet formation. It was found that the number of the satellite droplets after collision appears to increase with an increase in the droplet charge.

## 8.2 Recommendations for future studies

The research presented in this work aimed to apply the developed numerical technique to various phenomena. The other direction for future work involves extending the current modeling capabilities by taking into account additional physical effects such as charge convection and parameters and applying them to different applications. There are a number of such which deserve further investigations. Some are described below.

### 8.2.1 Frost removal using electric field

In recent years, the electrohydrodynamic (EHD) technique has received some attention as a possible effective defrosting method [1-4]. It was found that frost formation changes considerably under the action of an electric field: the frost morphology is affected and crystals solidify in different forms. Depending on electric field intensity, the electric field can either reduce or increase the frost mass accumulated on the cold surface. It is believed that using EHD methods can help removal of ice crystals because of the attracting force towards the electrodes. The observed crystals are thinner and more fragile as compared to those grown without an electric field. In addition, because the frost structure is relatively irregular and rather thin, it may not sustain itself from gravity force as it grows further. It is also expected that when the frequency of the applied force matches with the natural frequencies of vibrations of the ice crystals, more frost can be removed due to the resonance phenomenon. It seems that using a sweeping frequency which covers a range of frequencies could be more effective due to covering the natural frequencies of different ice crystals and increasing the chance of resonance.

### 8.2.2 Separation of bio-particles in microfluidic chips

In recent years, separation of micro particles, such as biological cells and viruses, has become a crucial technology in the clinical laboratories. Existing technologies can be categorized into biological markers or “label-free” techniques, such as differential biomechanical and electromechanical.

The microfluidic technology has attracted considerable attention and broadened its applications in biology, chemistry, medicine and engineering. Manipulation of biological particles (DNAs, viruses, bacteria, cells, multi cellular organisms, etc.) is highly important in various biomedical and biotechnological applications.

An applied electric field introduces electrophoretic and dielectrophoretic forces (DEP) on the particles. DEP can potentially be used to capture cancer cells that are less likely to be isolated by traditional methods [5-7]. Simulating the electric force in such microfluidic devices plays an important role in properly designing and locating the electrodes needed for the isolating process. Estimation of the DEP forces acting on biological cells is much more challenging. Because of their complex and heterogeneous structure, they cannot be considered as a simple sphere, for example, human red blood cells are essentially oblate spheroids with indented sides, while viruses and bacteria often have elongated cigar shapes. The droplet-based characteristic of this device makes it convenient to use smaller sample portions of patients' blood.

### 8.2.3 Coating

The developed model is capable of capturing the fluid motion inside the droplets. Substrate coating has been proposed as one of the potential applications of the digital microfluidic systems, and the quality of the coating operation depends on the internal fluid flow [8]. The developed model can be used to optimize such coating processes. This task can be performed by controlling the micro-droplet speed and the resulting internal flow.

### 8.2.4 Hot-spot cooling

Thermal management of microprocessors has become an increasing challenge in recent years. A cooling method on a “digital micro-fluidics” platform can be proposed whereby

discrete droplets are manipulated and moved using electric forces to certain spots to cool hotspots. Electrowetting was demonstrated by as a viable technique to manipulate droplets. This may find several applications in which temperature of the solid surface is of the great concern and could involve extending the modeling techniques to include thermal forces as an added parameter.



## References

- [1] C. M. Joppolo, L. Molinaroli, S. D. Antonellis and U. Merlo, “Experimental analysis of frost formation with the presence of an electric field on fin and tube evaporator”, *Int. J. of Refrigeration*, vol. 35, no. 2, pp. 468-474, 2012.
- [2] C. C. Wang, R. T. Huang, W. J. Sheu and Y. J. Chang, “Some observations of the frost formation in free convection: with and without the presence of electric field”, *Int. J. of Heat and Mass Transfer*, vol. 47, no. 14-16, pp. 3491-3505, 2004.
- [3] V. Tudor and M. M. Ohadi, “The effect of stationary and sweeping frequency AC electric fields on frost crystal removal on a cold plate”, *Int. J. of Refrigeration*, vol. 29, no. 4, pp. 669-677, 2006.
- [4] V. Tudor, M. M. Ohadi and F. H. R. Franca, “An experimental investigation on frost control using DC and AC electric fields on a horizontal downward-facing plate”, *HVAC&R Research*, vol. 9, no. 2, pp. 2013-213, 2003.
- [5] Y. Sheng, Z. Jun, L. Ming, A. Gursel, D. Haiping, S. Ronald and L. Weihua, “On chip high-throughput manipulation of particles in a dielectrophoresis-active hydrophoretic focuser”, *Scientific Reports*, vol. 4, no. 5060, pp. 1-8, 2014.
- [6] A. Sonnenberg, J. Y. Marciniak, E. A. Skowronski, S. Manouchehri, L. Rassenti, E. M. Ghia, G. F. Widhopf, T. J. Kipps and M. J. Heller, “Dielectrophoretic isolation and detection of cancer-related circulating cell-free DNA biomarkers from blood and plasma”, *Electrophoresis*, vol. 35, no.12, pp. 1828-1836, 2014.
- [7] F. Fabbri, S. Carloni, W. Zoli, P. Ulivi, G. Gallerani, P. Fici, E. Chiadini, A. Passardi, G. L. Frassinetti, A. Ragazzini and D. Amadori, “Detection and recovery of circulating colon cancer cells using a dielectrophoresis-based device: KRAS mutation status in pure CTCs”, *Cancer Letters*, vol. 335, no. 1, pp. 225-231, 2013.
- [8] D. Witters, S. Vermeir, R. Puers, B. F. Sels, D. E. De Vos, J. Lammertyn and R. Ameloot, “Miniaturized layer-by-layer deposition of metal-organic framework coatings through digital microfluidics”, *Chem. Mater.*, vol. 25, no. 7, pp. 1021-1023, 2013.

## Curriculum Vitae

<b>Name:</b>	Osameh Ghazian
<b>Post-secondary Education and Degrees:</b>	<p>University of Tehran Tehran, Tehran, Iran 2004-2008 B.Sc.</p> <p>University of Tehran Tehran, Tehran, Iran 2008-2010 M.Sc.</p> <p>The University of Western Ontario London, Ontario, Canada 2011-2014 Ph.D.</p>
<b>Honours and Awards:</b>	<p>MITACS Accelerate Fellowship, April – November 2014</p> <p>Western Engineering Graduate Entrance Scholarship (WEGES).</p> <p>Ranked 2<sup>nd</sup> Electrostatics Society of America, June 2014, University of Notre Dame, USA.</p> <p>IEEE Award Winner, Outstanding Presentation in Graduate Symposium 2013.</p> <p>Ranked 1<sup>st</sup> in Electrostatics Joint Conference, June 2012 Cambridge, ON, Canada.</p> <p>Ranked 2<sup>nd</sup> in Electrostatics Society of America Conference, June 2013 Cocoa beach, FL, USA.</p> <p>Ranked 3<sup>rd</sup> Cage Club Conference On High Voltage Engineering and Applied Electrostatics, August 2013, University of Waterloo, Waterloo, ON, Canada.</p>
<b>Related Work Experience</b>	<p>Teaching Assistant The University of Western Ontario 2011-2014</p> <p>MITACS Research Intern Cayuga Displays Inc. April – December 2014</p>

**Publications:**

O. Ghazian, K. Adamiak and G.S.P Castle, Head-on collision of electrically charged droplets, *Journal of Electrostatics*, Volume 73, February 2015, Pages 89–96.

O. Ghazian, K. Adamiak and G.S.P Castle, “Electric-field-induced oscillations of water droplets deposited on insulating surfaces”, *Journal of Electrostatics*, Volume 71, Issue 3, June 2013, Pages 489–495.

O. Ghazian, K. Adamiak and G.S.P Castle, “Numerical simulation of electrically deformed droplets less conductive than ambient fluid”, *Colloids and Surfaces A: Physicochemical and Engineering Aspects*, Volume 423, 20 April 2013, Pages 27–34.

O. Ghazian, K. Adamiak and G.S.P Castle, “Oscillation, pseudo-rotation and coalescence of sessile droplets in a rotating electric field”, *Colloids and Surfaces A: Physicochemical and Engineering Aspects*, Volume 441, 20 January 2014, Pages 346–353.

O. Ghazian, K. Adamiak and G.S.P Castle, “Spreading and retraction control of charged dielectric droplets”, *Colloids and Surfaces A: Physicochemical and Engineering Aspects*, Volume 448, 20 April 2014, Pages 23–33.

O. Ghazian and J. Sabarinathan, “Variable-focus liquid lens simulation”, *International Journal of Engineering Systems Modelling and Simulation*, 2013, In Press.

O. Ghazian, K. Adamiak and G.S.P Castle, “On the effect of electrostatic forces on impacting dielectric droplets” *International Symposium on Electrohydrodynamics 2014*, Japan.

O. Ghazian, K. Adamiak and G.S.P Castle, “Interaction between two, stationary or impacting, electrically charged droplets” *Electrostatics Society of America*, June 2014, University of Notre Dame, USA.

O. Ghazian, K. Adamiak and G.S.P Castle, “Electrohydrodynamic deformation and breakup of an uncharged droplet suspended in an ambient fluid of higher conductivity”, *Proceedings of the 2012 Electrostatics Joint Conference*, Electrostatics Society of America, June 2012 Cambridge, ON, Canada.

O. Ghazian, K. Adamiak and G.S.P Castle, “Numerical simulation of the deformation dynamics of an uncharged droplet suspended in another liquid under uniform electric field”, *Cage Club Conference On High Voltage Engineering and Applied Electrostatics*, August 2011, University of Waterloo, Waterloo, ON, Canada.

O. Ghazian, K. Adamiak and G.S.P Castle, “Oscillation, pseudo-rotation and coalescence of sessile droplets in a rotating electric field”, *Electrostatics Society of America*, June 2013 Cocoa beach, FL, USA.